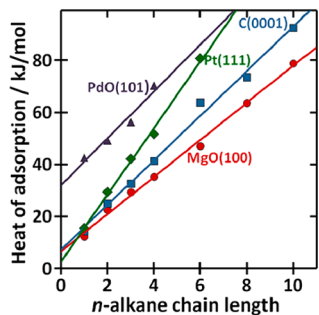


Enthalpies and Entropies of Adsorption on Well-Defined Oxide Surfaces: Experimental Measurements

Charles T. Campbell* and Jason R. V. Sellers

Department of Chemistry, University of Washington, Seattle, Washington 98195-1700, United States



CONTENTS

| | | | |
|--|------|--|------|
| 1. Introduction | 4106 | 6.3. Relating Metal Atom Adsorption Energies with Metal/Oxide Adhesion Energies and Sublimation Energies of the Bulk Metal | 4122 |
| 2. Experimental Methods for Measuring Adsorption Energies and Entropies on Single Crystals | 4107 | 6.4. SCAC Studies of Metal Adsorption Enthalpies on Single-Crystal Oxide Surfaces | 4122 |
| 2.1. Single-Crystal Adsorption Calorimetry (SCAC) | 4107 | 6.4.1. Adsorption Enthalpies of Different Metal Atoms on Defective MgO(100) | 4122 |
| 2.2. Equilibrium Adsorption Isotherms (EAI): Enthalpies and Entropies of Adsorption | 4108 | 6.4.2. Silver Atom Adsorption Enthalpies on Different Oxide Surfaces | 4125 |
| 2.3. Temperature Programmed Desorption (TPD): Activation Energies and Prefactors for Desorption | 4109 | 6.5. TPD Studies of Metal Atom Adsorption Enthalpies on Oxides | 4128 |
| 3. Intact Molecular Adsorption and Noble Gas Adsorption on MgO(100) | 4111 | 6.5.1. TPD Studies of the Adsorption of Late Transition Metals and Noble Metals | 4128 |
| 3.1. Entropies of Adsorption on MgO(100) and Other Surfaces: Correlation with Gas-Phase Entropies | 4111 | 6.5.2. TPD Studies of the Adsorption of Alkali Metals | 4130 |
| 3.2. Predicting Desorption Prefactors Using this Adsorption Entropy Correlation | 4115 | 7. Concluding Remarks | 4130 |
| 3.3. Trends in Adsorption Enthalpies on MgO(100) | 4116 | Author Information | 4131 |
| 4. Intact Molecular Adsorption on Oxide Single-Crystal Surfaces: Adsorption Enthalpies from TPD Studies of Desorption Energies | 4117 | Corresponding Author | 4131 |
| 4.1. CO | 4117 | Notes | 4131 |
| 4.2. Alkanes | 4117 | Biographies | 4131 |
| 4.3. Water | 4118 | Acknowledgments | 4131 |
| 4.4. Alcohols | 4118 | References | 4131 |
| 4.5. Comparison to Adsorption Calorimetry on Powdered Oxides | 4119 | | |
| 5. Reversible Dissociative Adsorption on Oxides: Adsorption Enthalpies by TPD | 4120 | 1. INTRODUCTION | |
| 6. Metal Atom Adsorption on Oxide Surfaces and Metal/Oxide Interfacial Adhesion | 4120 | The chemistry of oxide surfaces plays a central role in many current technologies, and promises to play an ever-increasing role in future technologies. In addition to their importance in catalytic and electrocatalytic materials, oxides are central ingredients in photocatalysts, photoelectrocatalysts, transparent electrodes for photovoltaics, solid electrolytes, superconductors, microelectronics, computer chips, protective coatings, windows, optics, batteries, piezoelectrics, pyroelectrics, and ceramics, just to name a few. When compared to metal surfaces, however, much less is understood about the chemistry of oxide surfaces. This is mainly related to the greater difficulty of preparing well-ordered single-crystalline surfaces of oxides, and the fact that even once prepared they are often not electrically conductive enough to be amenable to many of the techniques for surface characterization. However, the past decade has seen the development of many new sample preparation techniques for oxide surfaces that overcame these problems, and consequently an explosion of experimental results characterizing adsorption and surface reactions on well-defined oxide surfaces, where the nature of the surface sites involved is well-known. | |
| 6.1. Predicting When the Adsorbing Metal Will Reduce the Underlying Oxide | 4120 | | |
| 6.2. Metal/Oxide Adhesion Energies and Wetting of Oxide Surfaces by Metal Films | 4121 | Special Issue: 2013 Surface Chemistry of Oxides | |

Received: August 11, 2012
Published: February 26, 2013

Here, we review what has been learned about the enthalpies and entropies of adsorption reactions on well-defined oxide surfaces from experimental measurements. In discussing well-defined oxide surfaces here, we refer to studies on ordered surfaces of bulk single-crystal oxides and single-facet nanomaterials, and of ordered thin films of oxides that have been grown epitaxially on the surfaces of bulk single crystals of metals. We will refer to these collectively as “single-crystalline oxide surfaces” below. Because adsorption energies on thin-film oxides have been shown to be strengthened by interactions with the underlying metal when the oxide film is 1 nm thick or thinner, we limit this Review to include only those cases where the oxide films are thicker than 1 nm. Trends in experimental adsorption energies and entropies are revealed and discussed. These energies and entropies will serve as important experimental benchmarks to guide the currently intense worldwide efforts to improve theoretical methods, like density functional theory (DFT) with periodic boundary conditions, with respect to their accuracy at predicting the relative energies of adsorbates on oxide surfaces.

Accompanying the rapid developments in the experimental study of adsorption on oxide surfaces mentioned above, there also has been a dramatic increase in efforts to understand the surface reactivity of oxides and trends in their surface reactivity at the electronic-structure level, through computational quantum mechanical approaches. Approaches using density functional theory, with the generalized gradient approximation (GGA-DFT) and periodic boundary conditions, which have proven so effective in explaining and even predicting the reactivity of metal surfaces,^{1–7} have been shown to have greater limitations when applied to oxide surfaces.^{8–10} An improved version, “DFT+U”, cures some of the problems by introducing the *U* parameter in the Hamiltonian to localize the d- or f-electrons. This *U* can be chosen to give a better fit than GGA-DFT to some reaction energies.¹⁰ GGA+U is now the most widely used methodology, but it still has limitations in energy accuracy. Because of the greater challenges presented by oxide surfaces, there are currently many efforts worldwide to improve such computational methodology for applications in oxide surface chemistry, for example, through use of hybrid functionals, which is a much more computationally intensive alternative.

Currently, the main experimental benchmarks that are used for validating these new theoretical approaches are bulk properties like the heats of oxide formation, band gaps, lattice parameters, phonon spectra, etc. Experience with metal surfaces has proven that, to achieve the most effective theoretical codes, they must also be validated against experimental measurements of surface properties, adsorption energies, surface reaction energies, and adsorbate geometries for well-defined adsorbates at well-defined surface sites. Such measurements are only possible using single-crystalline surfaces. Currently, there is no easily accessible source for adsorption energies of well-defined adsorbates at well-defined sites on single-crystalline oxide surfaces. This Review presents by far the most extensive compilation of such energies yet available. In many cases, these energies have been extracted directly from the source literature, but in some cases the data in the source literature were treated here with kinetic and thermodynamic models to provide reliable estimates of the adsorption energies and metal/oxide adhesion for vapor-deposited metal films.

Adsorption energies on single-crystalline oxide surfaces have been measured by single-crystal adsorption calorimetry

(SCAC), equilibrium adsorption isotherms (EAI), and temperature programmed desorption (TPD), also referred to as thermal desorption spectroscopy (TDS). The SCAC measurements provide these energies very directly, so they are unambiguous. Equilibrium adsorption isotherms are also relatively straightforward, but do require that the adsorption \rightleftharpoons desorption process is reversible.

On the other hand, TPD is much less direct and requires some explanation and, for many of the cases here, our own interpretation of the measured TPD spectra to extract adsorption energies. In the best case, TPD only provides an accurate activation energy for desorption, *E_d*. This can only be equated with the adsorption energy when both the adsorption \rightleftharpoons desorption process is reversible and the activation energy for adsorption is negligible. We will limit ourselves to such cases here. Also, many of the papers used here for extracting adsorption energies in such cases have already reported such estimates of adsorption energies, but only by assuming a pre-exponential factor for desorption, *v*. In these cases, and when the adsorbate is molecularly adsorbed, we will reevaluate the adsorption energies using instead values for *v* estimated from a recently discovered correlation between the pre-exponential factor for desorption and the entropy of the gas-phase product,¹¹ which applies only to reversible molecular adsorption \rightleftharpoons desorption where the activation energy for adsorption is negligible. This new approach provides more reliable estimates for adsorption energies of molecularly adsorbed species.

In some cases of dissociative adsorption and associative recombination in desorption, the criteria also hold that adsorption \rightleftharpoons desorption is reversible and the activation energy for adsorption is negligible. We will also estimate adsorption energies from TPD data for these cases, using instead estimates for the pre-exponential factor determined in similar cases from detailed kinetic analyses of the TPD peak lineshapes versus coverage. Unfortunately, there are few cases of this type. There are no other cases where we know the adsorption energy associated with molecular fragments on single-crystal oxide surfaces by either EAI or direct calorimetric measurements. These must await SCAC measurements, which we have recently initiated for studying dissociative adsorption on single-crystal oxide surfaces.

2. EXPERIMENTAL METHODS FOR MEASURING ADSORPTION ENERGIES AND ENTROPIES ON SINGLE CRYSTALS

2.1. Single-Crystal Adsorption Calorimetry (SCAC)

Calorimetric measurements of heats of adsorption of gases on high surface area metal films were being performed already in the 1950s (refs 12–14 and refs therein). However, on such complex surfaces, it is generally not clear what are the structures or even the chemical formulas of the adsorbates being formed upon gas adsorption. Single crystals provide much simpler surfaces, which offer tremendous advantages for determining the chemical formulas and geometric structures of the adsorbates formed upon gas adsorption. Adsorption microcalorimetry thus became much more powerful when methods were developed that allowed it to be done on such single-crystal surfaces by measuring the tiny temperature increase associated with exothermic gas adsorption.

Masel's group published a description of the first apparatus that could measure heats of adsorption on single-crystal

surfaces.¹⁵ The precision of that method for heat detection, based on a thermistor, was problematic and not further applied. The real breakthrough came with an apparatus developed by David King's group, who named the measurement of heats of adsorption on single-crystal surfaces "single-crystal adsorption calorimetry", or SCAC for short. Their apparatus, shown schematically in Figure 1, detects the transient temperature rise

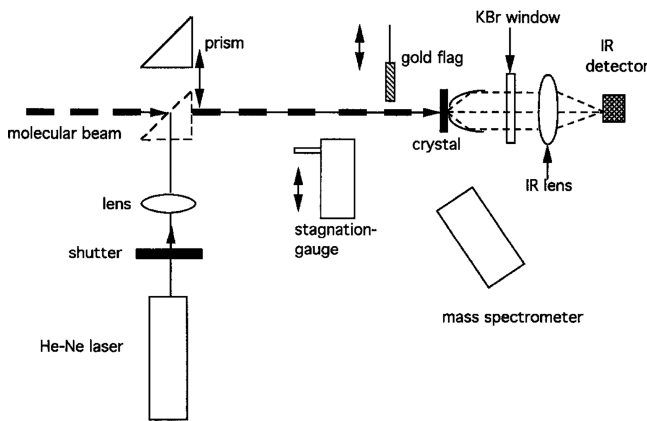


Figure 1. Schematic of the single-crystal adsorption calorimeter developed by the group of Sir David King. Pulses of a molecular beam impinge on the clean surface of a very thin single crystal, held in ultrahigh vacuum. The transient temperature rise is measured by infrared optical pyrometry of the back of the crystal. The heat signal associated with this temperature rise was calibrated using pulses of light of known power from a He-Ne laser, which are directed down the molecular beam path. Reprinted with permission from ref 23. Copyright 1996 Elsevier.

of a single crystal (proportional to the heat of reaction) upon adsorption of gas pulses from a molecular beam onto a surface using infrared optical pyrometry.^{16–23} This method is sensitive enough to detect the heat of adsorption of gas pulses containing only ~5% of a monolayer of adsorbate, thus allowing measurements of the heat of adsorption versus coverage. However, because the heat signal in that method varies as T^3 , where T is the sample temperature, it is not sensitive enough for measurements on samples well below room temperature. King's group subsequently developed a method that works at very low temperatures wherein the single crystal is fused to a pyroelectric crystal (lithium tantalate),²⁴ but this has not been further applied because it does not allow most samples to be annealed to high enough temperature to obtain a well-ordered surface.

Most recently, our group has developed^{25–28} and further perfected^{29–32} a heat detection method for SCAC based on gently touching a soft pyroelectric polymer ribbon against the back surface of the single-crystal sample during calorimetry measurements, and removing it during sample cleaning and annealing. This heat detection method has proven to have much higher sensitivity. It is now routinely applicable at cryogenic conditions.^{31,33–35} Precision is high, with a pulse-to-pulse standard deviation as good as 1.3 kJ/mol from 100 to 300 K when using gas pulses that contain only 1.5×10^{13} molecules per cm^2 (1% of a monolayer).³¹ The pulse-to-pulse standard deviation mentioned above sets the detection limit at ~5 kJ/mol. This heat detection method has the added advantage that it can use much thicker single crystals,³⁰ which are easier to obtain, clean, and maintain. The absolute accuracy of this type of calorimeter depends on the accuracy of its calibration, but

also the accuracy of measuring the absolute beam flux and area, and the sticking probability. When applying it to measure the energy of metal vapor adsorption, where the high-coverage limit should equal the literature value for the bulk heat of sublimation, we generally found the agreement to be within 3% (based on the average of several runs). Most of those measurements will be reviewed below. Our more recent low-temperature measurements with molecules that form multilayers, whose heat can also be compared to the bulk sublimation energy, also gave absolute accuracies better than 3%.³⁵ The readsorption of gases in the molecular beam that do not stick upon first hitting the sample makes a negligible contribution to the heat for all of the systems we have studied, which will generally be the case when the sticking probability is higher than 0.3 and the gases are well pumped. Also, we have never noticed any contamination on the front face of the sample from the ribbon touching the back of the sample.

In SCAC, one derives the differential heat of adsorption (q_{ad}) from the measured heat (q_{cal}) using:^{26,29}

$$\begin{aligned} q_{\text{ad}} &= -\Delta H_{\text{ad}}^0 \\ &= -\Delta U_{\text{ad}}^0 + RT_{\text{sample}} \\ &= q_{\text{cal}} - 4/2RT_{\text{source}} + 5/2RT_{\text{sample}} \end{aligned} \quad (1)$$

where ΔH_{ad}^0 is the standard enthalpy change for the adsorption reaction (gas \rightarrow adsorbed, with gas and solid both at the temperature of the single crystal, T_{sample}), R is the universal gas constant, and T_{source} is the temperature of the effusive molecular beam source. The heat of adsorption as defined here is identical to the isosteric heat of adsorption. The superscripts 0 here on ΔH_{ad}^0 and ΔU_{ad}^0 refer to their values at the standard pressure of 1 bar. Both ΔU_{ad}^0 and ΔH_{ad}^0 are always negative numbers, so ΔU_{ad}^0 is always smaller in absolute value than ΔH_{ad}^0 .

Methods for and results from SCAC have been reviewed several times previously.^{36–40}

2.2. Equilibrium Adsorption Isotherms (EAI): Enthalpies and Entropies of Adsorption

The use of equilibrium adsorption isotherms to determine the enthalpy change upon adsorption of a gas (ΔH_{ad}) is analogous to making a Clausius–Clapeyron plot to determine the enthalpy of vaporization (ΔH_{vap}). In the latter, the equilibrium vapor pressure above a liquid ($P_{\text{vap,eq}}$) is measured versus temperature (T). The plot of $\ln(P_{\text{vap,eq}}/P^0)$ versus $1/T$ over a reasonably narrow range of T gives a straight line with slope equal to $-\Delta H_{\text{vap}}^0/R$ (where P^0 is the standard pressure of 1 bar and R is the gas constant) and a y -intercept equal to $\Delta S_{\text{vap}}^0/R$, where ΔS_{vap} is the entropy of vaporization. The superscripts 0 here on ΔH_{vap}^0 and ΔS_{vap}^0 refer to their values at the standard pressure of 1 bar. Their values correspond to the average temperature in the range over which this straight line is fitted to the data. Similarly, to determine an adsorption enthalpy, the equilibrium vapor pressure ($P_{\theta,\text{eq}}$) above an adlayer at fixed coverage (θ) is measured versus temperature (T). The plot of $\ln(P_{\theta,\text{eq}}/P^0)$ versus $1/T$ over a reasonably narrow range of T gives a slope equal to $\Delta H_{\text{ad}}^0/R$ and a y -intercept equal to $-\Delta S_{\text{ad}}^0/R$, where both values correspond to that specific coverage and 1 bar pressure. The change of signs here is due to reversing the reaction direction from vaporization to condensation. The coverage dependence can be determined by repeating the measurements and data analysis at a different coverage. Coverage can be measured by any of a variety of

probes. We will cite here examples where it was measured on flat single crystals by LEED and helium atom scattering for the purposes of EAI measurements.

The simplest way to generate the needed data ($P_{\theta,\text{eq}}$ versus T at several fixed coverages) is to perform an isotherm, starting with a clean surface in a fixed volume, and then introducing more gas in fixed increments, allowing the system to come to equilibrium at the same constant temperature after each incremental dose. The pressure ($P_{\theta,\text{eq}}$) and coverage (θ) are measured at each increment and plotted as θ versus $P_{\theta,\text{eq}}$. After a series of these isotherms are plotted, a horizontal cut at any constant θ gives the needed $P_{\theta,\text{eq}}$ versus T data points.^{41,42}

Starting already before 1978, a group at the University of Washington made the first quantitative measurements of adsorption enthalpies on any oxide single-crystal surface using EAI measurements on “MgO(100) smoke” (Figure 2).^{41,42}

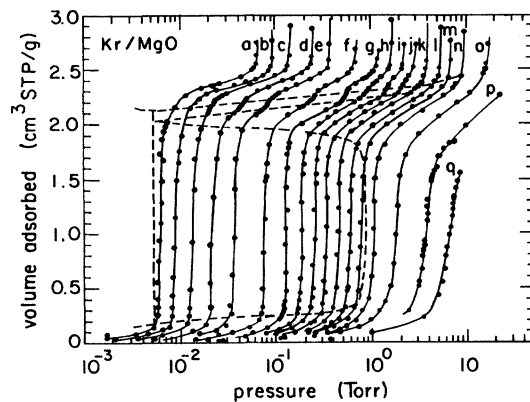


Figure 2. Typical equilibrium adsorption isotherm (EAI) data, in this case volumetric measurements of Kr adsorption on MgO(100) smoke. Isotherm temperatures (in K): (a) 66.76, (b) 67.82, (c) 69.10, (d) 70.97, (e) 72.56, (f) 75.21, (g) 77.47, (h) 78.97, (i) 80.28, (j) 81.59, (k) 83.16, (l) 84.52, (m) 85.87, (n) 87.56, (o) 90.88, (p) 95.21, and (q) 98.66 K. The Kr pressure ($P_{\theta,\text{eq}}$) at the adsorbed volume in the middle of the first large vertical riser (i.e., at $\theta_{\text{eq}} = 1/2 \text{ ML}$ coverage) was used to determine the enthalpy and entropy of the first monolayer from a plot of $\ln(P_{\theta,\text{eq}}/P^0)$ versus $1/T$, as described in the text. Dashed lines indicate estimated phase boundaries. Reprinted with permission from ref 42. Copyright 1984 American Physical Society.

This special MgO powder was produced by burning Mg filaments as done in early camera flash bulbs. This results in a powder with relatively large specific area which, upon examination by electron microscopy, proved to consist primarily of single-crystal nanocubes of MgO (with sizes from 20 to 200 nm) with only the (100) surface exposed except at the edges.⁴² The advantage of such a single-facet powder (which we will refer to here as “MgO(100) smoke”) as compared to a flat crystal is that the surface coverage can be measured with much simpler equipment. Thus, the equilibrium coverage was measured by simple volumetric measurements of the amount of gas consumed by adsorption (i.e., by monitoring the decrease in pressure as compared to that for the same number of moles of gas introduced into the same volume in the absence of any adsorbent).

An advantage of EAI measurements is that they also provide the entropy of adsorption. To our knowledge, the only cases where this entropy has actually been determined in this way for any single-crystal oxide surface are about a dozen examples using MgO(100) smoke, which we will discuss in detail. The entropy of adsorption is important because it can be combined

with the enthalpy to provide the equilibrium constant for adsorption, K_{eq} , and its temperature dependence:

$$\ln K_{\text{eq}} = \Delta S_{\text{ad}}^0 / R - \Delta H_{\text{ad}}^0 / (RT) \quad (2)$$

As we discuss below, the entropy of adsorption is also needed to calculate the rate constant for reactions of the adsorbate using transition state theory. We apply it below to do just that, specifically in predicting pre-exponential factors for desorption from entropy trends.

This MgO(100) smoke was also used by that same group for calorimetric measurements of the heat capacity of He adlayers on MgO(100) back in 1985,⁴³ which to our knowledge was the only calorimetric measurement ever reported for the heat capacity of any adlayer on any single-crystal surface, until our recent report for adsorbed water on Pt(111).³⁵ Interestingly, while that same calorimeter could have been used to determine adsorption energies on MgO(100) smoke, it was not applied for that purpose.

2.3. Temperature Programmed Desorption (TPD): Activation Energies and Prefactors for Desorption

In TPD, a sample with preadsorbed species is heated in ultrahigh vacuum, typically at a constant heating rate between 0.1 and 100 K/s, while monitoring the rate of appearance of gases emitted by the surface.⁴⁴ The rate of appearance of gases is typically monitored using a mass spectrometer. A typical example of TPD, measuring the rate of butane desorption from MgO(100) after different initial doses,⁴⁵ is shown in Figure 3.

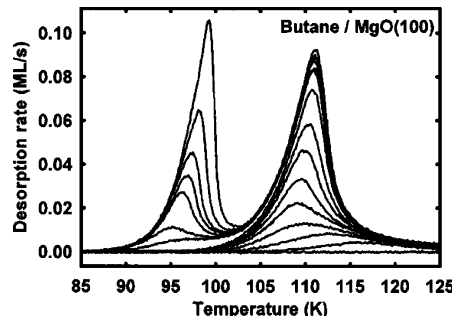


Figure 3. Typical TPD data for butane on MgO(100) at a heating rate of 0.6 K/s for 16 initial coverages in the range of 0–1.76 ML: 0.00, 0.10, 0.19, 0.28, 0.42, 0.51, 0.66, 0.76, 0.88, 1.05, 1.13, 1.21, 1.31, 1.38, 1.52, and 1.76 ML. Two desorption peaks are resolved, multilayer (99 K) and first-layer (110 K) desorption, as well as a high-temperature tail on the first-layer peak due to desorption from defect sites on the surface (mainly step edges). Reprinted with permission from ref 45. Copyright 2005 American Institute of Physics.

Methods for improving mass spectrometric measurements of desorption rates for TPD have been discussed.⁴⁶ Frequently, the ionization source of the mass spectrometer or its entrance aperture is located in line-of-sight, near and normal to the surface to enhance the signal of the desorbing species being monitored. In well-pumped systems, this has the advantages that (1) the signal from the front surface of the sample is greatly enhanced as compared to its back and edges, and (2) the signal for a given species is directly proportional to the flux of desorbing molecules (provided the common assumptions hold that all of the molecules desorb with the same velocity distribution and that their internal energy distribution does not change, or at least that the changes in this distribution do not affect the ionization probability). It is necessary for kinetic

Table 1. Enthalpies and Entropies of Molecular Adsorption on MgO(100) Determined by Equilibrium Adsorption Isotherms in a Temperature Range with the Specified Average Temperature^a

| adsorbate | $-\Delta H_{ad}^0$ /(kJ/mol) | $-\Delta S_{ad}^0(T)$ /(J/mol/K) | $S_{ad}^0(T)$ /(J/mol/K) | $S_{gas}^0(T)$ /(J/mol/K) | temp/K | citation |
|--|------------------------------|----------------------------------|--------------------------|---------------------------|--------|----------|
| Part A: MgO(100) Smoke | | | | | | |
| Ar | 8.4 | | | | 60 | 42 |
| Kr | 11.7 | | | | 85 | 42 |
| Xe | 15.5 | | | | 115 | 42 |
| N ₂ | 14.7 | | | | | 52 |
| NH ₃ | 71 → 25 | 36 → 161 | 126 → 1 | 162 | 170 | 53 |
| methane | 12 | 91 | 49.5 | 141 | 77 | 54 |
| ethane | 18 | 100 | 93.9 | 193 | 120 | 54 |
| propane | 23 | 96 | 138 | 234 | 140 | 54 |
| butane | 27 | 100 | 169 | 269 | 163 | 54 |
| pentane | 31 | 140 | 161 | 301 | 185 | 54 |
| neopentane | 30.4 | 146 | 112 | 258 | 200 | 55 |
| hexane | 34 | 142 | 198 | 340 | 207 | 54 |
| CH ₃ OH | 72 | 124 | 112 | 235 | 264 | 56 |
| CH ₃ Cl | 25 ± 4 | | | | 168 | 57 |
| Part B: Flat MgO(100) Crystals | | | | | | |
| H ₂ O ^b | 50 → 85 ± 2 | | | | 203 | 58 |
| C ₂ H ₂ (2 × 2) ^c | 29 ± 2 | | | | 91 | 59 |

^aWhen a range of enthalpy or entropy values are given, the arrow indicates that this is the direction of increasing coverage. ^bCoverage determined using He atom scattering (HAS). ^cCoverage determined using low energy electron diffraction (LEED).

analyses to be able to relate the measured signal (flux) at any time, t , to the total instantaneous desorption rate, $r(t)$.

Commonly, it is assumed that this total desorption rate is directly proportional to the instantaneous mass spectrometer signal for a given species, but this is not true for such line-of-sight measurements if the angular distribution of desorbing molecules changes. To minimize the error when the desorption angular distribution changes, the mass spectrometer can be placed so that the measured flux is at the so-called magic angle ($\sim 38^\circ$ from the surface normal).⁴⁷ If the signal is sufficient, it is better to instead monitor the non-line-of-site increase in the background pressure of the desorbing gas, which is proportional to the total desorption rate for well-pumped systems even when the velocity and angular distributions of the desorbing gas change with temperature.

Once desorption rate data versus temperature and coverage of the type shown in Figure 3 are obtained, one analyzes it to determine the activation energy for desorption, E_d . There are many methods that have been used to do this. A useful comparison on these methods and their accuracy in extracting E_d and other kinetic parameters has been published.⁴⁸ That report shows that some methods are much more accurate than others. When the adsorption ⇌ desorption process is reversible and the activation energy for adsorption is negligible, E_d can be related to enthalpy of adsorption, ΔH_{ad}^0 , by adding 1/2RT:

$$q_{ad} = -\Delta H_{ad}^0 = E_d + 1/2 RT \quad (3)$$

where R is the gas constant and T is the average sample temperature where the desorption rates were measured.³⁶ When the sticking probability for adsorption is near unity, as is usually the case for simple molecular adsorption, it is safe to assume that the activation energy for adsorption is negligible.

To extract E_d , the surface species are always assumed to be in equilibrium, in which case the desorption rate is a single-valued function of coverage and temperature: $r(\theta, T)$. We next describe our recommended method for extracting E_d for the case of most importance here: reversible molecular adsorption/desorption, where it is reasonable to assume that desorption

is a first-order process, in which case the Polanyi–Wigner equation gives:

$$r(\theta, T) = -d\theta/dt = \nu \exp(-E_d(\theta)/RT)\theta \quad (4)$$

where ν is the pre-exponential factor, which we typically assume does not vary with coverage or temperature, and $E_d(\theta)$ is the coverage-dependent desorption activation energy. This adsorption energy changes with coverage because various adsorption sites (e.g., defects, terrace sites, etc.) have different strengths of interaction, and interactions between the adsorbates change with the average adsorbate–adsorbate distance, so E_d is certainly expected to vary with coverage. By mathematical inversion of the rate data, the value of $E_d(\theta)$ can be obtained from the Polanyi–Wigner equation if ν is known:⁴⁹

$$E_d(\theta) = -RT \ln[(-d\theta/dt)/(\nu\theta)] \quad (5)$$

Typically, one treats ν as a variational parameter to optimize the fit between experimental and simulated TPDs, thus finding the prefactor that best matches the kinetics of the desorption process. This was the method used for alkanes on MgO(100).^{45,50} As to be discussed below, the value of the prefactor can be used to estimate the adsorption entropy, because the transition state for desorption is very similar to the gas.

One can also extract E_d using the first-order Redhead equation, which relates the temperature at which the desorption rate maximizes (T_p) to E_d , the heating rate (β), and ν :⁴⁴

$$E_d/(RT_p^2) = (\nu/\beta) \exp[-E_d/(RT_p)] \quad (6)$$

The most common practice is to simply use eq 6 and an assumed value for ν , which gives reasonable accuracy if the value of ν is approximately correct. A factor of 10 error in ν corresponds to an error of only $\sim 2.3RT_p$ in E_d , which is only 6 kJ/mol, or $\sim 7\%$, for $T_p = 300$ K and $\nu = 10^{15}$ s⁻¹. We review below our recent discovery of a new method for estimating this prefactor,¹¹ which gives values with a standard deviation in $\log(\nu/s^{-1})$ of only 0.86 from a tabulation of 24 measured

prefactors. We apply this below in eq 6 to estimate E_d for many systems.

Whenever molecular adsorption/desorption is not completely reversible such that partial dissociation competes with desorption, it leads to complexity that invalidates the above analyses. A creative way to circumvent that problem whenever that dissociation involves C–H, O–H, or N–H dissociation is to use the deuterated isotope, because this often greatly suppresses the dissociation probability during TPD (via the primary kinetic isotope effect), so that molecular desorption can now dominate.⁵¹

If adsorption is dissociative but the two adsorbed products are attracted to each other and prefer to populate neighboring sites, their associative desorption kinetics can be treated as a pseudo-first-order process using the same first-order analyses as described above to get E_d . This still requires that the adsorption ⇌ desorption process be reversible and the activation energy for adsorption be negligible (i.e., sticking probability near unity). We will analyze some cases like this below.

3. INTACT MOLECULAR ADSORPTION AND NOBLE GAS ADSORPTION ON MgO(100)

Table 1 summarizes reported measurements of the adsorption enthalpies and entropies determined on MgO(100) by EAI for several noble gases and molecules which remain intact upon adsorption. The standard entropies of the gas-phase species at the average temperature of the measurement, S_{gas}^0 , are included for comparison. Part A shows results for MgO(100) smoke where the surface coverage was measured by volumetric techniques, and Part B is for planar MgO(100) single crystals where the surface coverage was measured using ultrahigh vacuum (UHV) techniques. Note that for several of these studies, the structure of the adlayer as determined by neutron diffraction or other diffraction-based techniques was also reported.

3.1. Entropies of Adsorption on MgO(100) and Other Surfaces: Correlation with Gas-Phase Entropies

Figure 4 shows the standard entropies of these adsorbates ($S_{\text{ad}}^0 = S_{\text{gas}}^0 + \Delta S_{\text{ad}}^0$) on MgO(100) smoke, determined by EAI from Table 1, plotted versus the standard entropy of the gas-phase species at the temperature of the measurement. We add to this plot the standard entropies of these same and other adsorbates determined from desorption prefactors measured in TPD (at different temperatures), using transition state theory as described next. The values of these prefactors, desorption temperatures, heats of adsorption, and corresponding adsorbate entropies based on TPD data are listed in Table 2, to be described in more detail below.

When the adsorption ⇌ desorption process is reversible and the activation energy for adsorption is negligible, as it is for the cases in Table 2, the transition state for desorption is the molecule with its center of mass constricted to lie on a plane parallel to the surface at some distance far enough away from the surface that its interaction with the surface is negligible for any angle of rotation. In this case, the transition state is very well-defined. Its entropy ($S_{\text{TS,des}}^0$) is identical to that for the gas (S_{gas}^0) at the same temperature, except that it is missing one translational degree of freedom (the one perpendicular to the surface):

$$S_{\text{TS,des}}^0 = S_{\text{gas}}^0 - S_{\text{gas,1D-trans}}^0 \quad (7)$$

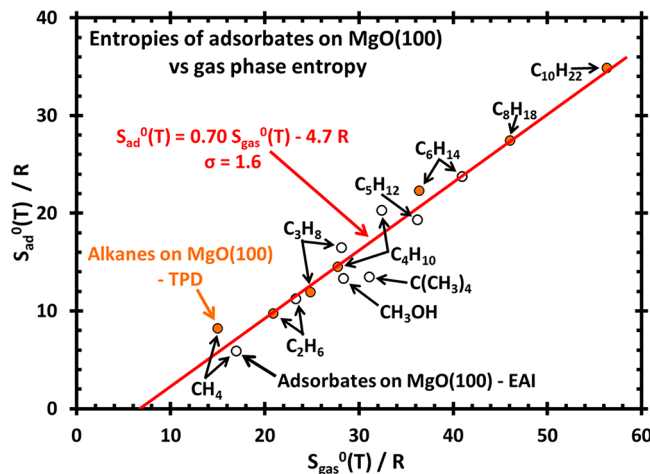


Figure 4. Plot of the standard entropies of adsorbates ($S_{\text{ad}}^0 = S_{\text{gas}}^0 + \Delta S_{\text{ad}}^0$) on MgO(100) smoke determined by equilibrium adsorption isotherms (EAI) plotted versus the standard entropy of the gas-phase species at the same temperature from Table 1. The standard entropies of these same and other adsorbates determined using desorption prefactors and peak temperatures from TPD data together with eq 11 are also included from Table 2. The agreement with EAI results proves the accuracy of this method. The best linear fit to these data is also shown, along with the standard deviation (σ) of the adsorbate entropies from this line. Reprinted with permission from ref 11. Copyright 2012 American Chemical Society.

The value of $S_{\text{gas,1D-trans}}^0$ for any gas can easily be calculated using statistical mechanics (the Sackur–Tetrode equation),⁶⁵ assuming that each translational degree of freedom contributes 1/3 of the total 3D translational entropy. This gives that:

$$S_{\text{gas,1D-trans}}^0 = (1/3)\{S_{\text{Ar,298K}}^0 + R \ln[(m/m_{\text{Ar}})^{3/2}(T/298 \text{ K})^{5/2}]\} \quad (8)$$

where m is the molar mass of the gas, m_{Ar} is that for argon, and $S_{\text{Ar,298K}}^0$ is the entropy of Ar gas at 1 bar and 298 K (=18.6 R).

Within the transition state theory,⁶⁶ the desorption prefactor is given by:

$$\nu = k_B T / h \exp(\Delta S_{\text{TS,des}}^0 / R) \\ = k_B T / h \exp[(S_{\text{TS,des}}^0 - S_{\text{ad}}^0) / R] \quad (9)$$

where k_B is Boltzmann's constant and h is Planck's constant. Substitution using eq 7 gives:

$$\nu = k_B T / h \exp[(S_{\text{gas}}^0 - S_{\text{gas,1D-trans}}^0 - S_{\text{ad}}^0) / R] \quad (10)$$

This can be rearranged to give an expression for calculating S_{ad}^0 from an experimentally determined value of ν :

$$S_{\text{ad}}^0 = (S_{\text{gas}}^0 - S_{\text{gas,1D-trans}}^0) - R \ln[\nu h / (k_B T)] \quad (11)$$

where all entropies are for the same temperature T as the measurement of ν . This expression was used to calculate the adsorbate entropies listed in Table 2 and Table 3 and plotted in Figure 4 for the points from TPD. The values of S_{gas}^0 for these molecules are found in standard thermodynamic tables and, when necessary, extrapolated to different temperatures using tabulated heat capacities. The validity of eq 11 is verified by the excellent agreement seen in Figure 4 between the adsorbate entropies on MgO(100) obtained using eq 11 and those directly measured by EAI. Below we summarize its applications

Table 2. Adsorption Enthalpies and Entropies for Molecularly Adsorbed Species on MgO(100) Determined by TPD, Showing Also the Peak Temperature and Heating Rate^a

| adsorbate | adsorption site | T _p /K | β/(K/s) | log(ν/s ⁻¹) | -ΔH _{ad} ⁰ /(kJ/mol) | S _{ad} ⁰ (T _p)/R | S _{gas} ⁰ (T _p)/R | citation |
|------------------|---------------------|-------------------|---------|-------------------------|--|--|---|----------|
| H ₂ O | Mg | 235 | 3 | 14.5 | 67.9 | 11.9 | 21.7 | 60 |
| CO | | 59 → 57 | 0.2 | 13.8 | 16.9 → 16.3 | 9.38 → 9.30 | 18.1 → 18.0 | 61 |
| | | 63 → 59 | 0.6 | 13.9 → 13.8 | 17.6 → 16.5 | 9.53 → 9.40 | 18.3 → 18.1 | 49 |
| | c(4 × 2) phase | 45 | 0.6 | 13.7 | 12.3 | 8.72 | 17.2 | 49 |
| NO | | 84 → 75 | 0.5 | 14.0 | 24.1 → 21.3 | 10.4 → 10.1 | 19.6 → 19.2 | 62 |
| methane | | 47 | 0.6 | 13.1 | 12.3 | 8.20 | 15.0 | 50 |
| ethane | | 75 | 0.6 | 14.9 | 22.5 | 9.76 | 20.9 | 50 |
| propane | | 93 | 0.6 | 15.6 | 29.4 | 11.9 | 24.9 | 50 |
| butane | | 111 | 0.6 | 15.7 ± 1.6 | 35.4 ± 3.9 | 15.8 | 27.8 | 45 |
| hexane | | 144 | 0.6 | 16.0 | 47.0 | 22.3 | 36.4 | 50 |
| octane | | 175 | 0.6 | 17.9 | 63.6 | 27.4 | 46.1 | 50 |
| decane | | 204 | 0.6 | 19.1 | 77.9 | 34.9 | 56.3 | 50 |
| benzene | parallel to surface | 175 | 5 | 15.0 | 51.1 | 16.5 | 28.3 | 63 |
| | tilted | 148 | 5 | 14.9 | 42.6 | 15.9 | 27.3 | 63 |
| methanol | Mg | 296 → 275 | 3 | 15.3 | 90.5 → 83.7 | 16.9 → 16.6 | 28.8 → 28.4 | 64 |
| | oxygen | 240 | 3 | 15.2 | 72.3 | 16.2 | 27.8 | 64 |

^aPrefactor and enthalpy values in bold were determined in the original paper by careful analysis of the TPD data, so the resulting adsorbate's entropy at T_p determined from this prefactor using eq 11 is also in bold. The remaining prefactor, enthalpy, and entropy values not in bold were estimated using eqs 16, 6, and 11, respectively. The entries in bold under "adsorption site" are as reported in the original paper. Those not in bold are based on our tentative assignments as justified in section 4. When a range of T_p and enthalpy values are given, the arrow indicates that this is the direction of increasing coverage.

to understanding the thermodynamics of adsorption, some of which have already been described,¹¹ and which prove quite powerful.

By combining the adsorbate entropies on MgO(100) measured by both EAI and TPD in Figure 4, one can see that there is a nearly perfect linear correlation between S_{ad}⁰ and S_{gas}⁰, with a slope of 0.70, a y-intercept of -4.7R, and a correlation coefficient (R²) of 0.96 (standard deviation = 1.6R). Note that this is for temperatures where desorption is fast enough to perform these EAI and TPD measurements ($\sim 10^{-3}$ to 100 ML/s), which are the most relevant temperatures for many types of experiments. We showed that this correlation becomes a direct proportionality if we first subtract from S_{gas}⁰ the entropy associated with one degree of translational freedom, S_{gas,1D-trans}⁰, to correct for the fact that an adsorbate has very restricted motion (i.e., sits in a very steep potential well) in the direction perpendicular to the surface, z.¹¹ The proportionality:

$$S_{ad}^0 = 0.68(S_{gas}^0 - S_{gas,1D-trans}^0) \quad (12)$$

was found to fit the data very well, with R² = 0.96 and a standard deviation of 1.7R. This proves that the adsorbate maintains $\sim 2/3$ of the entropy of the gas-phase species (after subtracting the entropy of its z translation motion).

As shown in Figure 5, the linear relationship between S_{ad}⁰ and S_{gas}⁰ for MgO(100) in Figure 4 was found to hold with the same slope and almost as high R² (0.94) when we include entropies for all of the other molecules whose prefactors for desorption had been determined experimentally from fitting TPD data in a reliable way on any other oxide single-crystal surface (as listed in Table 3, to be discussed below) and our own experimental determinations of prefactors for linear alkanes on graphite(0001) and Pt(111) from TPD data.⁶⁷ Again, eq 11 was used to convert measured prefactors into adsorbate entropies. The equation for this line in Figure 5:

$$S_{ad}^0(T) = 0.70S_{gas}^0(T) - 3.3R \quad (13)$$

agrees very well with the measured entropies, with a standard deviation of only 2.2R. Including this much larger data set shifted the y-intercept only very slightly (up by 1.4R) from the line for MgO(100), and the slope stayed the same. This indicates that this linear relationship is independent of both the surface material and the adsorbed molecule. As we show below, eq 13 provides a very useful and simple method for estimating adsorption entropies for molecularly adsorbed gases on oxide surfaces. We also show below that this can be applied to estimate pre-exponential factors in rate constants for reactions involving adsorbates, like desorption.

The explanation we offered for the slope of $\sim 2/3$ in Figures 4 and 5 and eqs 12 and 13 is that there is a very weak corrugation of the molecule–surface interaction potential for translational and rotational motions parallel to the surface, with saddle points that are lower than RT at temperatures where desorption is fast enough for EAI and TPD, but a steep energy well for motion perpendicular to the surface. Thus, all x and y components of translational and rotational motion of the gas molecule are maintained upon adsorption, but any z components are lost. If the entropies of these motions are equally distributed between x, y, and z directions in the gas, then 2/3 of the entropy will be maintained after adsorption (when vibrational entropy is negligible).¹¹

We found that the behavior is somewhat different for molecules with gas entropies above $\sim 60R$, where the slope increased to almost unity up to 100R (i.e., for n-alkanes with >10 atoms).¹¹ The reason for this change is the slower increase of the rotational entropy in the gas-phase molecules due to the bends in these longer-chain alkanes and the increased importance of vibrational entropy in these larger molecules (which desorb at higher temperatures).¹¹ This is the same reason that the prefactors for n-alkane desorption stop increasing with chain length above 10 carbons,^{68,69} as explained on the basis of molecular dynamics simulations.^{70–72}

The only case where ΔS_{ad}⁰ was measured versus coverage by EAI is for NH₃ on MgO(100) smoke, which shows a large

Table 3. Adsorption Enthalpies and Entropies for Molecularly Adsorbed Species on Oxide Surfaces Determined by TPD, Showing Also the Peak Temperature and Heating Rate^a

| adsorbate | oxide surface | adsorption site | T _p /K | β/(K/s) | log(ν/s ⁻¹) | -ΔH _{ad} ⁰ /(kJ/mol) | S _{ad} ⁰ (T _p)/R | S _{gas} ⁰ (T _p)/R | citation |
|------------------|--|-----------------------------|-------------------|---------|-------------------------|--|--|---|----------|
| N ₂ | TiO ₂ (110) | metal | 105 → 90 | 1 | 14.1 → 14.0 | 29.7 → 25.3 | 10.3 → 9.91 | 19.4 → 18.8 | 84 |
| | | oxygen | 70 → 45 | 1 | 13.8 → 13.6 | 19.3 → 12.0 | 9.29 → 8.21 | 18.0 → 16.4 | 84 |
| O ₂ | TiO ₂ (110) | metal | 71 → 60 | 1 | 13.9 → 13.8 | 19.6 → 16.4 | 9.69 → 9.27 | 18.5 → 17.9 | 84 |
| | | oxygen | 44 → 41 | 1 | 13.6 | 11.8 → 10.9 | 8.53 → 8.37 | 16.9 → 16.7 | 84 |
| | TiO ₂ (110) 8% reduced | oxygen vacancies | 410 | 2 | 19.8 ^b | 162 | 14.0 | 24.7 | 85 |
| | Cr ₂ O ₃ (0001) | | 320 → 300 | 4 | 14.7 → 14.6 | 93.5 → 87.3 | 13.4 → 13.2 | 23.8 → 23.6 | 86 |
| CO | PdO(101) | metal | 250 → 233 | 1 | 14.5 | 74.7 → 69.2 | 12.8 → 12.6 | 23.0 → 22.7 | 87 |
| | | oxygen | 117 | 1 | 14.1 | 33.4 | 10.9 | 20.3 | 87 |
| | MgO(100) | | 59 → 57 | 0.2 | 13.8 | 16.9 → 16.3 | 9.38 → 9.30 | 18.1 → 18.0 | 61 |
| | | | 63 → 59 | 0.6 | 13.9 → 13.8 | 17.6 → 16.5 | 9.53 → 9.40 | 18.3 → 18.1 | 49 |
| CO | TiO ₂ (110) | c(4 × 2) phase | 45 | 0.6 | 13.7 | 12.3 | 8.72 | 17.2 | 49 |
| | | | 153 → 137 | 1 | 14.3 | 44.5 → 39.6 | 11.7 → 11.4 | 21.4 → 21.0 | 84 |
| | | | 170 → 135 | 0.5 | 14 | 49.5 → 39.1 | 13.1 → 11.9 | 21.8 → 21.0 | 88 |
| | | metal | 180 → 175 | 1 | 14.4 | 52.9 → 51.4 | 12.1 → 12.0 | 22.0 → 21.9 | 89 |
| | Cr ₂ O ₃ (0001) | | 105 | 1 | 14.1 | 29.9 | 10.8 | 20.1 | 89 |
| | Fe ₃ O ₄ (111) | Fe ³⁺ step edges | 230 | 3 | 19.6 ^b | 88.1 | 12.7 | 22.9 | 90 |
| | | Fe ²⁺ terraces | 200 → 180 | 3 | 14.5 → 14.4 | 57.4 → 51.3 | 12.4 → 12.1 | 22.4 → 22.0 | 90 |
| | | | 110 | 3 | 14.2 | 30.4 | 10.9 | 20.3 | 90 |
| NO | NiO(100) | | 137 → 115 | 3 | 14.3 → 14.2 | 38.4 → 31.9 | 11.4 → 11.0 | 21.1 → 20.4 | 61,62 |
| | ZnO(10̄10) | | 360 | 2.5 | 14.8 | 108 | 13.8 | 24.4 | 91 |
| | MgO(100) | | 84 → 75 | 0.5 | 14.0 | 24.1 → 21.3 | 10.4 → 10.1 | 19.6 → 19.2 | 61 |
| | TiO ₂ (110) | | 129 → 126 | 0.5 | 13.5 | 36.0 → 35.2 | 13.3 → 13.2 | 21.1 → 21.0 | 92 |
| H ₂ O | RuO ₂ (110) | | 495 → 430 | 3 | 15.0 → 14.9 | 150 → 129 | 14.8 → 14.4 | 25.8 → 25.3 | 93 |
| | | | 250 | 3 | 14.6 | 72.8 | 13.1 | 23.4 | 93 |
| | NiO(100) | | 220 → 216 | 3 | 14.6 → 14.5 | 63.6 → 62.4 | 12.8 → 12.7 | 22.9 | 61,62 |
| | MgO(100) | metal | 235 | 3 | 14.5 | 67.9 | 11.9 | 21.7 | 60 |
| | CeO ₂ (111) | metal | 271 | 2 | 14.6 | 79.9 | 12.3 | 22.3 | 94 |
| | | | 320 → 265 | 1 | 14.7 → 14.6 | 97.1 → 79.5 | 12.8 → 12.3 | 23.0 → 22.2 | 95 |
| | | oxygen | 185 → 170 | 2 | 14.4 → 14.3 | 53.2 → 48.6 | 11.3 → 11.0 | 20.8 → 20.4 | 94 |
| | | | 207 → 195 | 1 | 14.4 | 61.1 → 57.3 | 11.6 → 11.4 | 21.2 → 21.0 | 95 |
| H ₂ O | CeO _{1.93} (111) | metal | 265 → 240 | 1 | 14.6 → 14.5 | 79.5 → 71.5 | 12.3 → 12.0 | 22.2 → 21.8 | 95 |
| | | oxygen | 190 | 1 | 14.4 | 55.8 | 11.4 | 20.9 | 95 |
| | CeO ₂ (001) | oxygen | 200 | 2 | 14.4 | 57.8 | 11.5 | 21.1 | 96 |
| | TiO ₂ (110) | metal | 306 → 278 | 1 | 14.7 → 14.6 | 92.6 → 83.7 | 12.7 → 12.4 | 22.5 | 84 |
| | | | 300 → 272 | 5 | 14.7 → 14.6 | 86.8 → 78.2 | 12.6 → 12.4 | 22.7 → 22.3 | 97 |
| | | oxygen | 189 → 183 | 1 | 14.4 | 55.5 → 53.6 | 11.3 → 11.2 | 20.9 → 20.7 | 84 |
| | | | 170 | 7.5 | 14.3 | 46.8 | 11.0 | 20.4 | 97 |
| | TiO ₂ (101) | metal | 257 → 246 | 1 | 14.6 → 14.5 | 76.9 → 73.4 | 12.2 → 12.1 | 22.1 → 21.9 | 98 |
| TiO ₂ | | oxygen | 190 | 1 | 14.4 | 55.8 | 11.3 | 20.9 | 98 |
| | TiO ₂ (100) | metal | 280 → 250 | 1.8 | 14.6 → 14.5 | 83.0 → 73.5 | 12.4 → 12.1 | 22.4 → 22.0 | 99 |
| | | oxygen | 171 | 1.8 | 14.3 | 49.0 | 11.1 | 20.5 | 99 |
| | α-Cr ₂ O ₃ (001) | metal | 310 | 2 | 14.7 | 92.2 | 12.7 | 22.6 | 100 |
| | | oxygen | 210 | 2 | 14.4 | 60.9 | 11.6 | 21.3 | 100 |
| H ₂ O | α-Cr ₂ O ₃ (001) 2% strained | oxygen | 185 | 2 | 14.4 | 53.2 | 11.3 | 20.8 | 100 |
| | | metal | 295 | 2 | 14.6 | 87.4 | 12.6 | 22.8 | 100 |
| | | oxygen | 210 | 2 | 14.4 | 60.9 | 11.6 | 21.3 | 100 |
| | | | 185 | 2 | 14.4 | 53.2 | 11.3 | 20.8 | 100 |
| | Fe ₃ O ₄ (111) | oxygen | 210 → 190 | 5 | 14.5 → 14.4 | 59.3 → 53.3 | 11.6 → 11.3 | 21.3 → 20.9 | 101 |
| | Fe ₃ O ₄ (001) | oxygen ¹⁰¹ | 225 | 2 | 14.5 | 65.5 | 11.8 | 21.6 | 102 |
| | RuO ₂ (110) | metal | 400 | 4 | 14.8 | 119 | 13.4 | 23.9 | 103 |
| | PdO(101) | oxygen | 197 | 1 | 14.4 | 58.0 | 11.4 | 21.0 | 104 |
| H ₂ O | Cu ₂ O(100) | oxygen | 210 → 183 | 2 | 14.4 | 60.9 → 52.6 | 11.6 → 11.2 | 21.3 → 20.7 | 105 |
| | ZnO(0001) | metal | 320 | 7.5 | 14.7 | 91.9 | 12.8 | 23.0 | 106 |
| | ZnO(000̄1) | oxygen | 207 | 5 | 14.4 | 58.4 | 11.6 | 21.2 | 107 |
| | | | 190 | 7.5 | 14.4 | 52.7 | 11.3 | 20.9 | 106 |
| | ZnO(10̄10) | metal | 370 | 1 | 14.8 | 113 | 13.2 | 23.6 | 108 |
| | | | 340 | 7.5 | 14.7 | 98.1 | 13.0 | 23.2 | 106 |
| | | oxygen | 190 | 7.5 | 14.4 | 52.7 | 11.3 | 20.9 | 106 |
| CO ₂ | TiO ₂ (110) | oxygen vacancies | 206 → 200 | 2 | 19.6 ^b | 79.7 → 77.2 | 13.5 → 13.4 | 24.1 → 24.0 | 109 |

Table 3. continued

| adsorbate | oxide surface | adsorption site | T_p/K | $\beta/(K/s)$ | $\log(\nu/s^{-1})$ | $-\Delta H_{ad}^0/(kJ/mol)$ | $S_{ad}^0(T_p)/R$ | $S_{gas}^0(T_p)/R$ | citation |
|-------------------------|------------------------|---------------------------------------|------------|---------------|--------------------|-----------------------------|-------------------|--------------------|----------|
| SO ₂ methane | ZnO(0001) | metal | 177 → 158 | 2 | 13.6 | 48.3 → 43.0 | 15.3 → 14.9 | 23.5 → 23.1 | 109 |
| | CeO ₂ (111) | metal | 135 → 125 | 1.3 | 14.4 → 14.3 | 39.0 → 35.9 | 12.5 → 12.3 | 22.6 → 22.3 | 110 |
| | MgO(100) | oxygen | 380 | 3 | 15.4 | 118 | 18.0 | 30.5 | 111 |
| | PdO(101) | | 47 | 0.6 | 13.1 | 12.3 | 8.20 | 15.0 | 50 |
| | ethane | MgO(100) | 143 → 140 | 1 | 14.7 | 42.6 → 40.1 | 9.15 → 8.95 | 19.4 → 19.2 | 112 |
| | PdO(101) | unsaturated | 75 | 0.6 | 14.9 | 22.5 | 9.76 | 20.9 | 50 |
| | propane | PdO(101) | 182 → 165 | 1 | 14.7 | 54.6 → 49.2 | 13.8 → 13.6 | 24.5 → 24.1 | 112 |
| | MgO(100) | 100 | 1 | 14.4 | 28.8 | 12.2 | 22.1 | 112 | |
| | PdO(101) | saturated | 93 | 0.6 | 15.6 | 29.4 | 11.9 | 24.9 | 50 |
| | isobutane | MgO(100) | 205 → 184 | 1 | 15.1 | 63.1 → 56.3 | 16.4 → 16.1 | 28.1 → 27.6 | 113 |
| | n-butane | PdO(101) | 151 → 135 | 1 | 14.9 | 45.6 → 40.5 | 15.5 → 15.2 | 26.9 → 26.4 | 113 |
| n-hexane | MgO(100) | metal | 111 | 0.6 | 15.7 ± 1.6 | 35.4 ± 3.9 | 15.8 | 27.8 | 45 |
| | PdO(101) | metal | 222 → 218 | 1 | 15.9 | 71.6 → 70.2 | 20.6 → 20.5 | 34.2 → 34.0 | 114 |
| | isobutane | MgO(100) | 175 | 1 | 15.6 | 55.1 | 19.1 | 32.0 | 114 |
| | n-octane | MgO(100) | 160 → 152 | 1 | 15.5 → 15.4 | 50.0 → 47.2 | 18.5 → 18.2 | 31.1 → 30.7 | 114 |
| | n-decane | MgO(100) | 137 | 1 | 15.3 | 42.1 | 17.5 | 29.7 | 114 |
| | cyclohexane | ZnO(0001) | 190 → 165 | 1.3 | 15.7 → 15.5 | 60.0 → 51.3 | 19.6 → 18.7 | 32.7 → 31.4 | 110 |
| | ethylene | ZnO(0001) | 140 → 130 | 1.6 | 13.4 | 37.7 → 34.9 | 20.7 → 20.0 | 28.6 → 27.9 | 115 |
| | isobutene | MgO(100) | 144 | 0.6 | 16.0 | 47.0 | 47.0 | 36.4 | 50 |
| | propene | Al ₂ O ₃ (111) | 175 | 0.6 | 17.9 | 63.6 | 61.5 | 46.1 | 50 |
| | isobutene | MgO(100) | 204 | 0.6 | 19.1 | 77.9 | 34.9 | 56.3 | 50 |
| methanol | cyclohexane | ZnO(0001) | 210 | 5 | 15.6 | 63.6 | 19.4 | 32.4 | 116 |
| | ethylene | Cr ₂ O ₃ (0001) | 220 → 210 | 4 | 14.8 | 64.2 → 61.1 | 14.2 → 14.1 | 25.0 → 24.8 | 117 |
| | isobutene | RuO ₂ (110) | 120 → 130 | 4 | 14.5 | 33.6 → 36.6 | 12.5 → 12.7 | 22.5 → 22.8 | 117 |
| | propene | TiO ₂ (110) | 320 | 3 | 15.1 | 96.7 | 15.5 | 26.8 | 118 |
| | isobutene | TiO ₂ (110) | 120 to 250 | 3 | 14.5 to 14.9 | 33.9 to 74.2 | 12.5 to 14.6 | 25.5 to 22.5 | 118 |
| | benzene | MgO(100) | 180 | 5 | 15.2 | 53.3 | 16.9 | 28.8 | 119 |
| | isobutene | TiO ₂ (110) | 210 → 190 | 2 | 15.6 → 15.5 | 65.5 → 58.7 | 19.3 → 18.7 | 32.3 → 31.5 | 120 |
| | benzene | parallel to surface | 175 | 5 | 15.1 | 51.3 | 16.6 | 28.5 | 63 |
| | isobutene | tilted | 148 | 5 | 15.0 | 42.8 | 16.0 | 27.6 | 63 |
| | benzene | Al ₂ O ₃ (111) | 163 | 5 | 15.0 | 47.5 | 16.3 | 28.1 | 63 |
| ethanol | isobutene | tilted | 156 | 5 | 15.0 | 45.3 | 16.2 | 27.9 | 63 |
| | methanol | ZnO(0001) | 250 | 5 | 15.4 | 75.6 | 18.3 | 31.0 | 121 |
| | isobutene | ZnO(10̄10) | 260 → 235 | 5 | 15.5 → 15.4 | 78.9 → 70.6 | 18.5 → 18.0 | 31.1 → 30.4 | 122 |
| | methanol | MgO(100) | 296 → 275 | 3 | 15.3 | 90.5 → 83.7 | 16.9 → 16.6 | 28.8 → 28.4 | 64 |
| | isobutene | oxygen | 240 | 3 | 15.2 | 72.3 | 16.2 | 27.8 | 64 |
| | methanol | TiO ₂ (101) | 295 → 260 | 1 | 15.3 → 15.2 | 92.8 → 81.1 | 16.9 → 16.4 | 28.8 → 28.1 | 98 |
| | isobutene | oxygen | 170 | 1 | 14.9 | 51.5 | 15.1 | 26.2 | 98 |
| | methanol | TiO ₂ (110) | 370 → 323 | 1.5 | 15.5 → 15.4 | 117 → 101 | 17.8 → 17.3 | 30.2 → 29.3 | 123 |
| | isobutene | metal | 313 → 295 | 2 | 15.4 | 97.1 → 91.1 | 17.0 → 16.8 | 29.1 → 28.8 | 124 |
| | methanol | oxygen | 183 | 1.5 | 15.0 | 55.1 | 15.3 | 26.5 | 123 |
| 1-propanol | isobutene | 165 | 2 | 14.9 | 49.0 | 15.0 | 26.1 | 124 | |
| | methanol | ZnO(1010) | 440 | 1.5 | 15.7 | 141 | 18.7 | 31.3 | 125 |
| | isobutene | Al ₂ O ₃ (0001) | 325 → 217 | 5 | 15.4 → 15.1 | 98.7 → 64.0 | 17.3 → 15.8 | 29.4 → 27.3 | 126 |
| | methanol | TiO ₂ (110) | 395 → 337 | 1.5 | 16.3 → 16.1 | 131 → 110 | 22.3 → 21.2 | 36.6 → 35.0 | 123 |
| | isobutene | metal | 310 | 4.5 | 16.0 | 97.5 | 20.7 | 34.2 | 127 |
| | methanol | oxygen | 188 | 1.5 | 15.5 | 58.4 | 18.3 | 30.8 | 123 |
| | isobutene | 225 → 185 | 4.5 | 15.6 → 15.5 | 68.8 → 55.7 | 19.0 → 18.2 | 31.9 → 30.7 | 127 | |
| | methanol | TiO ₂ (110) | 413 → 352 | 1.5 | 17.1 → 16.8 | 143 → 120 | 26.9 → 25.3 | 43.1 → 40.9 | 123 |
| | isobutene | oxygen | 204 | 1.5 | 16.0 | 65.6 | 21.5 | 35.4 | 123 |
| | methanol | TiO ₂ (110) | 400 → 340 | 1.5 | 16.9 → 16.6 | 137 → 114 | 25.5 → 23.9 | 41.2 → 38.9 | 123 |
| isopropanol | isobutene | 213 | 1.5 | 15.8 | 67.8 | 20.6 | 34.0 | 123 | |
| | methanol | TiO ₂ (110) | 438 → 366 | 1.5 | 17.9 → 17.5 | 159 → 130 | 31.8 → 29.5 | 50.2 → 46.8 | 123 |
| 1-butanol | isobutene | 206 | 1.5 | 16.5 | 68.1 | 24.3 | 39.4 | 123 | |
| | methanol | TiO ₂ (110) | 425 → 347 | 1.5 | 17.8 → 17.3 | 154 → 122 | 31.3 → 28.7 | 49.4 → 45.7 | 123 |
| 2-butanol | isobutene | 213 | 1.5 | 16.5 | 70.3 | 24.2 | 39.2 | 123 | |
| | methanol | TiO ₂ (110) | 430 → 351 | 1.5 | 17.4 → 16.9 | 152 → 120 | 28.8 → 26.1 | 45.8 → 42.0 | 123 |
| t-butanol | isobutene | 225 | 1.5 | 16.0 | 72.6 | 21.9 | 35.9 | 123 | |
| | methanol | CeO ₂ (111) | 300 | 2 | 16.1 | 97.2 | 21.5 | 35.6 | 128 |

Table 3. continued

| adsorbate | oxide surface | adsorption site | T_p/K | $\beta/(K/s)$ | $\log(\nu/s^{-1})$ | $-\Delta H_{ad}^0/(kJ/mol)$ | $S_{ad}^0(T_p)/R$ | $S_{gas}^0(T_p)/R$ | citation |
|-------------|------------------------|-----------------|-----------|---------------|--------------------|-----------------------------|-------------------|--------------------|----------|
| formic acid | TiO ₂ (110) | metal | 210 | 2 | 15.7 | 65.9 | 19.5 | 32.7 | 128 |
| | | oxygen | 375 | 2 | 16.5 | 125 | 23.2 | 38.0 | 129 |
| | | metal | 320 → 285 | 2 | 16.2 → 16.1 | 104 → 91.9 | 22.0 → 21.2 | 36.2 → 35.1 | 129 |
| NiO(111) | ZnO(0001̄) | | 375 | 5 | 15.6 | 116 | 18.6 | 31.4 | 130 |
| | | | 167 | 5 | 15.0 | 48.7 | 15.8 | 27.3 | 131 |

^aPrefactor and enthalpy values in bold were determined in the original paper by careful analysis of the TPD data, so the resulting adsorbate's entropy at T_p determined from this prefactor using eq 11 is also in bold. The remaining prefactor, enthalpy, and entropy values not in bold were estimated using eqs 16, 6, and 11, respectively. The entries in bold under "adsorption site" are as reported in the original paper. Those not in bold are based on our tentative assignments as justified in the text. When a range of T_p and enthalpy values are given, the arrow indicates that this is the direction of increasing coverage. ^bPrefactors at defects were calculated using the value from eq 16 multiplied by 10⁵ (see text).

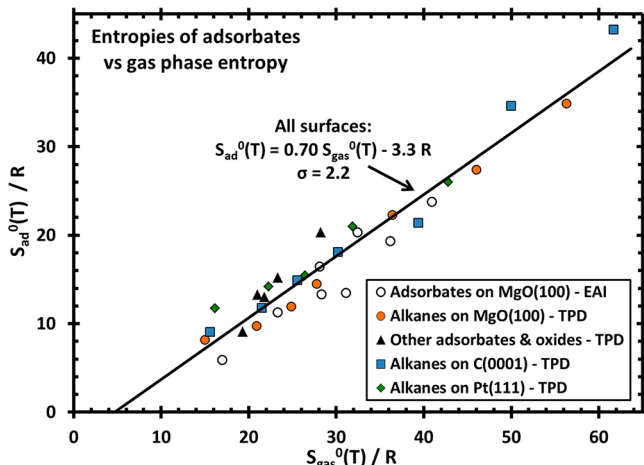


Figure 5. Plot of the standard entropies of adsorbates (S_{ad}^0) on several surfaces plotted versus the standard entropy of the gas-phase species at the same temperature. Data for MgO(100) and other oxides are from Tables 1–3. Entropies for linear alkanes on Pt(111) and graphite(0001) were calculated using eq 11 with experimental prefactors and peak temperatures reported in ref 67. The best-fit line is also shown. Adapted with permission from ref 11. Copyright 2012 American Chemical Society.

decrease with coverage from $-47 \text{ J}/(\text{mol K})$ (after defects are populated) to $-172 \text{ J}/(\text{mol K})$.⁵³ A large decrease in ΔS_{ad}^0 is predicted for an ideal 2D lattice gas model where adsorbate–adsorbate interactions are negligible, due to the large decrease in configurational entropy of the adsorbate as the fractional occupation of sites (θ) increases:⁷³

$$S_{\text{config}} = R \ln[(1 - \theta)/\theta] \quad (14)$$

The accompanying decrease in the heat of adsorption with coverage, from 71 to 25 kJ/mol here,⁵³ indicates that there are repulsive lateral interactions between adsorbed ammonia molecules. However, at low coverage where the average adsorbate–adsorbate separation is large, these can be neglected and the adlayer still should have very large configurational entropy. The point for NH₃ was omitted from Figure 5 because it drops from 5R above the line to 10R below the line (i.e., ~ 0) with increasing coverage. No variation with coverage was reported for the other adsorbates studied by EAI, attributed to the fact that they had attractive interactions and thus condensed into islands. Thus, Figure 5 and eq 13 are only valid for cases with such attractive interactions. A huge decrease in S_{ad} with coverage is probably characteristic of adsorbates with strong repulsive interactions.

There is no significant configurational entropy for the adsorbates that gave rise to the linear relationships of Figures 4 and 5 and eqs 12 and 13. Those were for high coverages and mainly for cases where there are attractive adsorbate–adsorbate interactions, so they cluster into 2D islands. The usual statistical mechanics model adapted for that case is the 2D crystal lattice model, and not the 2D ideal lattice gas model, which is only appropriate when there are negligible or weakly repulsive adsorbate–adsorbate interactions. There is no configurational entropy in a 2D crystal lattice, only vibrational entropy (including frustrated rotational and translational entropy). It is surprising that $\sim 2/3$ of the entropy associated with motion in the gas phase remains after adsorption, suggesting that these 2D islands may be liquid-like at these temperatures where desorption is fast enough for TPD and EAI measurements. Rotations and translations parallel to the surface somehow remain unhindered in such adsorbate islands. The data points in Figure 5 are also reasonably fit by the trend predicted for 3D liquids based on Trouton's rule,¹¹ which again illustrates how large these adsorbate entropies are.

Table 2 summarizes TPD measurements of the activation energies (E_d) and pre-exponential factors (ν) for desorption determined on MgO(100) for molecules that remain intact upon adsorption and desorption. We first list the peak temperatures for desorption (T_p) and heating rates (β). We also list the values reported for E_d and ν when the analysis method used to determine these was rigorous, and the enthalpy of adsorption determined from E_d using eq 3. We do not include here reported values for E_d and ν in those cases where the value for ν was simply assumed. Instead, we list here what we believe to be a more reliable estimate for ν (determined on the basis of the entropy correlation of Figure 5 and eq 13 and transition state theory, as described next), and its corresponding value for E_d (determined from T_p , ν , and β , using simple first-order Redhead analysis, eq 6).

3.2. Predicting Desorption Prefactors Using this Adsorption Entropy Correlation

Combining eq 7 with the approximation for S_{ad}^0 given by Figure 5 and eq 13 (i.e., $S_{ad}^0 = 0.70 S_{gas}^0 - 3.3R$), we get that the standard entropy of activation, $\Delta S_{TS,des}^0$, is:

$$\begin{aligned} \Delta S_{TS,des}^0 &= S_{TS,des}^0 - S_{ad}^0 \\ &= (S_{gas}^0 - S_{gas,1D-trans}^0) - (0.70 S_{gas}^0(T) - 3.3R) \\ &= 0.30 S_{gas}^0 + 3.3R - S_{gas,1D-trans}^0 \end{aligned} \quad (15)$$

where $S_{\text{gas},1D\text{-trans}}^0$ can be calculated from eq 8. Simply plugging this value for $\Delta S_{\text{TS,des}}^0$ into eq 9 gives the prefactor ν :

$$\begin{aligned} \nu &= k_B T / h \exp(\Delta S_{\text{TS,des}}^0 / R) \\ &= k_B T / h \exp[(0.30S_{\text{gas}}^0 + 3.3R - S_{\text{gas},1D\text{-trans}}^0) / R] \\ &= (k_B T / h) \exp\{0.30S_{\text{gas}}^0 / R + 3.3 \\ &\quad - 9.31 \ln[(m/m_{\text{Ar}})(T/298 \text{ K})]\} \end{aligned} \quad (16)$$

Figure 6 shows a plot of the predictions of this equation plotted versus experimentally measured desorption prefactors for all

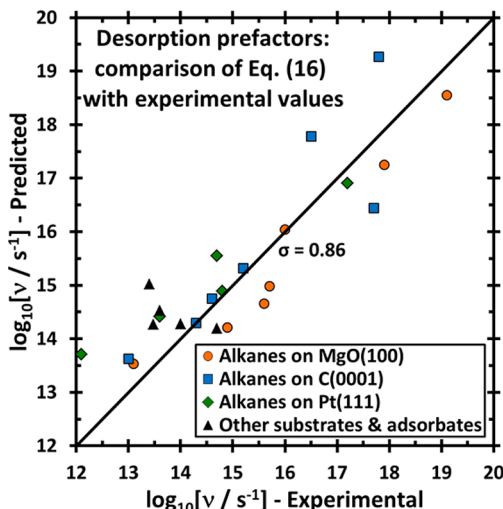


Figure 6. Prefactors for the desorption of molecularly adsorbed species as predicted from the gas-phase entropies using eq 16 (which was derived from the linear relationship in Figure 5 using transition state theory) plotted versus the experimentally measured prefactors. Data are mostly for molecules on oxide single crystals from Table 3, but also shown are data for *n*-alkanes on graphite(0001) and Pt(111), from ref 67. The line shows the expectation based on eq 16. Reprinted with permission from ref 11. Copyright 2012 American Chemical Society.

molecules on single-crystal oxides listed in Table 3, plus our own values for alkanes on Pt(111) and graphite(0001).⁶⁷ The predictions agree very well with these experimental prefactors with a standard deviation in $\log(\nu/\text{s}^{-1})$ of only 0.86, confirming the validity of eq 16 for estimating prefactors. Several discussions of the values for desorption prefactors have been published, but none of these have presented any relationships with prediction integrity anywhere near as good as eq 16.^{74–80}

For the other molecules/surfaces listed in Tables 2 and 3 where the desorption prefactor was not measured by fitting TPD data, we used eq 16 to estimate ν , and then used this ν in eq 6 to estimate E_d , and from that the heat of adsorption. These are the values listed in Tables 2 and 3 for those systems (except for the species at defect sites). Using twice the standard deviation on $\log(\nu/\text{s}^{-1})$ of 0.86 in Figure 6 gives a factor of 50 maximum error in ν at the 95% confidence limits, corresponding to a maximum error in the heat of adsorption of $4.0RT_p$ or 8 kJ/mol when $T_p = 250$ K.

Note that eq 16 is for the majority sites on single-crystal surfaces, and therefore appropriate for species on terraces only. We do not think it is appropriate for the entries in these tables that are assigned to defect sites. These are most frequently at step edges, and we have shown previously that metal adatoms

have a desorption prefactor that is 10^5 -fold larger at step edges than at terraces on Mo(100), due to the loss of all translational motion except in the one direction along the step edge.⁷⁹ For this reason, the prefactors in Table 3 for all species at defect sites have been taken as the predicted value from eq 16 but increased by this same factor of 10^5 . We do not know the accuracy of these prefactors for defect sites.

3.3. Trends in Adsorption Enthalpies on MgO(100)

Table 1 shows that, within a given class of adsorbates (like noble gases or alkanes), the heat of adsorption onto MgO(100) measured by EAI increases with the mass of the adsorbate. This is attributed to the increase in polarizability with the mass of the atoms and the number of atoms in the molecules. As an example, Figure 7 shows that the adsorption enthalpies for noble gases increase almost linearly with atomic number.

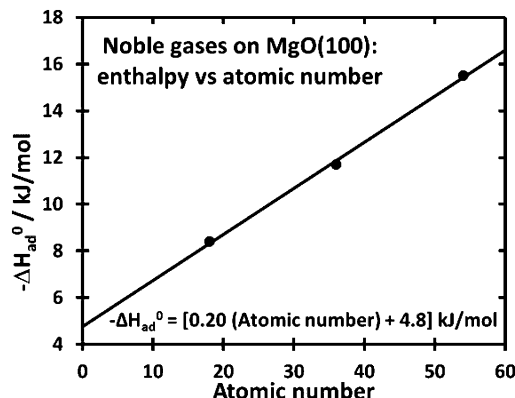


Figure 7. Heats of adsorption for noble gases on MgO(100) determined by EAI versus atomic number. Data from ref 42, and also listed in Table 1.

Table 1 also shows that molecules containing accessible lone pairs of electrons (water, ammonia, methanol, ethyne) have higher heats of adsorption as compared to the other molecules, which we attribute to a strong attraction associated with the donation of this lone pair into the unoccupied orbitals of the Mg^{2+} ion. The coverage dependence of ΔH_{ad}^0 in the first ML was determined by EAI only for the cases of NH_3 and H_2O . Surprisingly, it changes in the opposite direction, increasing from ~ 50 to 85 kJ/mol with coverage for H_2O , but decreasing from 71 to 25 kJ/mol for NH_3 . We attribute this to the fact that the only lone pair in each NH_3 binds to a Mg^{2+} ion, so that the only $\text{NH}_3\text{--NH}_3$ interactions will be their dipole–dipole repulsion (see below), whereas for H_2O , one lone pair of the O can bind to Mg^{2+} , while the other lone pair binds to a H atom in a neighboring H_2O molecule, to form an attractive hydrogen bond.

These $\text{NH}_3\text{--NH}_3$ repulsive lateral interactions have also been observed in desorption kinetics.⁸¹ The most stable binding configuration has the NH_3 axis perpendicular to the surface with the N lone pair donating to the Mg^{2+} ion.^{81,82} Such oriented dipoles always give rise to repulsive adsorbate–adsorbate interactions. Part of the decrease in heat of adsorption is probably also associated with the reported change to a less stable adsorbate structure at higher coverage, wherein one H atom of NH_3 makes a hydrogen bond to an O^{2-} ion of the MgO.⁸² Surprisingly, the heat of adsorption of NH_3 on MgO(100) smoke ($71\text{--}25$ kJ/mol) is much higher than that

reported from calorimetric measurements on normal powdered MgO with heterogeneous surfaces (14–6 kJ/mol⁸³).

Combining the adsorption energy values from Tables 1 and 2 allows us to make a number of conclusions about how adsorption enthalpies on MgO(100) depend on the adsorbate. Figure 8 shows that the adsorption enthalpies for alkanes at 1/2

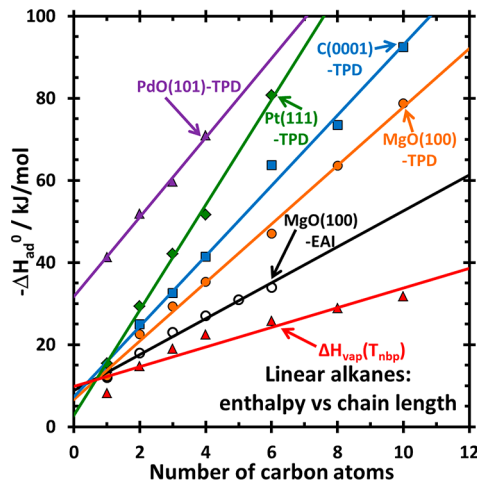


Figure 8. Heats of adsorption determined by TPD for linear alkanes on MgO(100), graphite(0001), and Pt(111), all at 1/2 ML coverage plotted versus alkane chain length, from ref 67. Also plotted are adsorption enthalpies for alkanes on PdO(101) from TPD (Table 3) and on MgO(100) smoke determined by EAI at full, saturated ML coverage (Table 1). For comparison, the bulk vaporization enthalpies of pure liquid alkanes at their normal boiling point are also shown, from ref 133. The best fit line to the data for PdO(101) has a slope of 9.7 kJ/mol/C atom and a y-intercept of 32 kJ/mol.

ML coverage (by TPD) increases nearly proportional to chain length, with a slope of 7.1 kJ/mol per C atom. We add here results for graphite (0001) and Pt(111) to show that this trend seems to be independent of substrate, with a proportionality constant that increases with the electrical conductivity (and therefore polarizability) of the substrate: MgO < C < Pt. This suggests that the bonding interaction is dominated by induced dipole–induced dipole interactions, which increase proportional to polarizability. It is surprising that the permanent dipole of MgO does not dominate over the induced dipoles in graphite and Pt, suggesting that the bonding mechanism(s) may be somewhat more complex. In any case, the adsorption energy scales nearly proportionally with the number of CH_x groups for these alkanes, with a slight offset indicating that CH₃ and CH₄ have slightly stronger attraction than CH₂ groups.

The adsorption energies for alkanes on MgO(100) smoke determined by EAI at full, saturated ML coverage are also shown in Figure 8. At short chain length, these agree with the TPD results at 1/2 ML, but as chain length increases, these full ML energies drop further below the 1/2 ML results. We attribute this to repulsive interactions, which only come into play at the highest coverage and are not present at 1/2 ML total coverage, despite the fact that this condition probably corresponds to islands held together by attractive interactions at high local coverages (but not as high as at the true saturation coverage before second ML growth probed by EAI measurements). The other oxides in Figure 8 will be discussed below.

4. INTACT MOLECULAR ADSORPTION ON OXIDE SINGLE-CRYSTAL SURFACES: ADSORPTION ENTHALPIES FROM TPD STUDIES OF DESORPTION ENERGIES

Table 3 summarizes TPD measurements of the activation energies (E_a) and pre-exponential factors (ν) for desorption determined on single-crystal oxide surfaces for molecules that remain intact upon adsorption and desorption. The format is the same as Table 2, listing first T_p and β , followed by reported values for E_a , ν , and ΔH_{ad}^0 when the analysis method used to determine ν was rigorous fitting to TPD data. For all other cases, the values for E_a , ν , and ΔH_{ad}^0 listed here were those determined using the value for ν estimated using eq 16, based on the entropy correlation of Figure 5 and transition state theory. The table is organized by the molecules, and under each molecule the oxides are listed according to the position of the cation in the periodic table, moving from its top left to its bottom right. As noted below, the heats of adsorption for some molecules correlate with the position of the oxide's cation in the period table, with the maximum heats being observed near the center of the transition metals where the d orbitals are approximately half filled.

While the nature and structure of the oxide surface sites for many of the adsorbate/substrate systems listed in Tables 1–3 have been characterized in depth using experimental measurements (spectroscopy, diffraction, etc.) and/or ab initio modeling methods, we do not describe those results in any detail here, because there are many other reviews within this same special issue of *Chemical Reviews* that discuss those types of studies in great depth.

4.1. CO

The heats of adsorption of CO on the oxides in Table 3 seem to maximize for the oxides of metals near the middle of the transition metals in the periodic table (e.g., Fe and Ru), which probably have the maximum number of valence d electrons available for bonding to CO. Transition metals further to the left may have used up all their d electrons in bonding to lattice O, and transition metals further to the right have fewer d electrons anyway and are well-known for their lack of reactivity. The weakest bonds to CO in this table are for MgO(100), which has no valence d electrons for bonding.

4.2. Alkanes

Adsorption enthalpies of alkanes on MgO(100) were discussed in detail above. As shown in Figure 8, the heats of adsorption of linear alkanes are ~30 kJ/mol higher on the PdO(101) surface than on MgO(100). Indeed, this Pd oxide surface binds alkanes even more strongly than the Pd metal itself, a very unusual and unexpected result, and it even dissociates alkanes during TPD. The reasons for this have been discussed in light of DFT calculations.^{112,132} Note that for the larger alkanes on PdO(101), dissociation competes with desorption, but much less so when using the perdeuterated alkane, yet the TPD peak temperature hardly shifts upon perdeuteration (Jason Weaver, private communication). Therefore, Redhead analysis of the TPD data for PdO(101) to get heats of adsorption should not be changed by more than 5% due to this competition. Both the Zn- and the O-polar faces of ZnO(0001) bind alkanes with the same number of carbon atoms slightly more strongly than MgO(100) (Table 3).

4.3. Water

Molecularly adsorbed water generally shows two TPD peaks from oxides, one near 300 K due to binding through its O atom to metal cation sites (with perhaps H-bonding to O anions) and one near 200 K due to water bound to oxygen anion sites. We will refer to these states below as corresponding to metal and oxygen sites, respectively. In general, the metal sites are populated first, and saturate at one water per metal site. As shown in Table 3, the heat of adsorption at the metal sites generally falls in the range 70–100 kJ/mol. This is considerably stronger than water binds to late transition metal surfaces (e.g., 51 kJ/mol for Pt(111)³⁵). The heats of adsorption for the O sites are in the range 50–60 kJ/mol, similar to that for water on Pt(111) and only slightly larger than the sublimation enthalpy of bulk water (47 kJ/mol¹³³). Note that in the cases indicated in Table 3, we used the TPD peak temperatures to assign the site of that water binding based on the general trend outlined above, indicating there if this differs from the assignment in the original paper (but not if there was no such assignment).

In some cases, the TPD peak due to molecularly adsorbed water on metal sites does not appear, due to the fact that these species dissociate to make an OH at the metal site and an H bound to the neighboring O site, or two different types of surface hydroxyls. We will discuss the water TPD peaks due to the recombinative desorption of these adsorbed dissociation products (OH+H) below when we discuss TPD studies of associative desorption energetics. There, we will also discuss the same species when produced instead at surface defects. In many cases, this TPD peak is at much higher temperature than the ~300 K characteristic of molecularly adsorbed water at metal sites, but in some cases, the peak is near or just above 300 K. In those cases, it has generally been difficult to determine what fraction of the desorption intensity is due to molecularly adsorbed water and what fraction is associative desorption, and the assignments to one or the other in some cases are debatable. Indeed, it seems that there may be an equilibrium between molecularly adsorbed water (dominant) and dissociated water (minority species) in this state, which complicates assignments. For these species, we analyzed this peak to get the heats of adsorption listed in Table 3 as if it were purely molecularly adsorbed.

4.4. Alcohols

Molecularly adsorbed methanol on oxides, like water, generally shows two TPD peaks at high coverage, one near 300 K generally attributed to methanol binding to metal cation sites through its own O atom (with perhaps H-bonding to the oxygen atoms of another methanol or to O anions) and one nearer to 200 K attributed to methanol bound to oxygen anion sites. Although these site assignments are not yet definitive, we will refer to these states below as corresponding to metal and oxygen sites, respectively. In general, the metal sites are populated first, and saturate at one methanol per metal site. As shown in Table 3, the heats of adsorption at the metal sites generally fall in the range 80–100 kJ/mol. This is considerably stronger than methanol bonds to late transition metal surfaces (e.g., 57 kJ/mol for Pt(111)¹³⁴). The heat of adsorption at the O sites is in the range 49–72 kJ/mol, similar to that for methanol on Pt(111) and only slightly larger than the sublimation enthalpy of methanol (45 kJ/mol¹³³). Note that in the cases indicated in Table 3, we used the TPD peak temperature to assign the site of that methanol binding, based on the general trend outlined above.

It has generally been difficult to determine whether the TPD peak at ~300 K from oxides surfaces is due to molecularly adsorbed methanol or associative desorption or some combination of both, and the assignment to one or the other is often based on limited evidence. Where available, direct STM images show mainly a single bump for this species on the terrace metal sites,^{135–137} implying that molecular adsorption is more favorable there. This is also the case for larger alcohols.^{138–141} As with water above, it seems that there may be an equilibrium between molecularly adsorbed methanol (dominant) and dissociated water (minority species) in this peak, with the two states quite similar in energy for many oxides (see, for example, the combined experimental and DFT study on TiO₂(110)¹³⁷), which complicates TPD peak assignments. For these species, we analyze this peak to get the heats of adsorption listed in Table 3 as if it were purely molecularly adsorbed, because this seems to be the dominant structure. Further evidence to support this is presented below, where we show that when analyzed in this way the heats of adsorption of linear alcohols on TiO₂(110) increase with the number of C atoms with the same average slope (7 kJ/mol per C) as that for alkanes on MgO(100).

For some oxide surfaces, a TPD peak near 300 K for molecularly adsorbed methanol on metal sites does not appear, due to the fact that methanol on metal sites instead dissociates to make methoxy at the metal site and an H bound to the neighboring O site. In these cases, a methanol TPD peak appears at considerably higher temperature and has been attributed to the recombinative desorption of these adsorbed dissociation products (OCH₃+H). We will discuss these cases below when we discuss TPD studies of associative desorption energetics, where we also discuss associative desorption of these same species when they are instead produced at defect sites on oxide surfaces.

Ethanol at high coverage has a TPD peak near 340 K, slightly above that for methanol. Again, it now seems that this state is mainly due to molecularly adsorbed ethanol on metal sites, which are probably in equilibrium with some dissociated ethanol (ethoxy plus H).^{138,139} We initially assigned this TPD peak on TiO₂(110) to dissociated ethanol, based on the fact that it was also seen at the same temperature when ethoxy was added to the surface by a different route (the dissociation of adsorbed tetraethoxy silane), albeit in the presence of surface or subsurface H.¹⁴² However, because ethanol was the observed gas-phase product, it could have resulted mainly from the desorption of molecularly adsorbed ethanol, produced at lower temperature by the association of surface ethoxy plus H. We now think that this was the case, based on STM showing that ethanol on terrace Ti sites is mainly molecularly adsorbed.^{138,139}

Figure 9 shows a plot of the heat of adsorption of linear alcohols up to butanol on the Ti and O sites of rutile TiO₂(110) versus the number of carbon atoms. (Again, the assignments to metal and O sites are still tentative.) As with the *n*-alkanes on MgO(100) (Figure 8), there is a linear increase with the number of C atoms, with a slope of 4.6 and 9.4 kJ/mol per C atom for O and Ti sites, respectively. The slope versus carbon number, averaged over both O and Ti sites (7.0 kJ/mol per C atom), is the same as that for the *n*-alkanes on MgO(100) at 1/2 ML (7.1 kJ/mol per C atom), and both are more than twice the slopes of the heats of vaporization of both bulk alkanes and bulk alcohols (~3 kJ/mol per C atom). The larger slopes here imply that the van der Waals interactions of

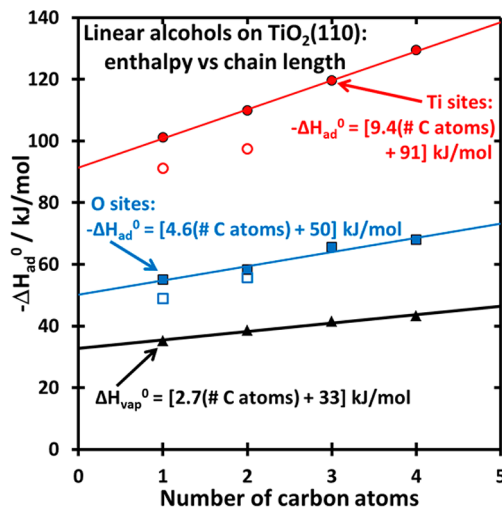


Figure 9. Heats of adsorption for linear alcohols on rutile $\text{TiO}_2(110)$ near saturation coverage (determined by TPD, see Table 3) plotted versus the number of carbon atoms in the alcohol molecule. Data for both the Ti sites and the O sites are shown, from ref 123. Data from other sources are included as hollow points. For comparison, the bulk vaporization enthalpies of the pure liquid alcohols are also shown, from ref 133.

the CH_x groups are stronger with both TiO_2 and MgO than with other alkane chains. The large, constant slope in Figure 9 can only be understood if these alcohols are lying flat along the surface, which would allow near optimal van der Waals interaction with the oxide for every CH_x group. This strongly supports the interpretation that these TPD peaks are due to simple desorption of molecularly adsorbed alcohols, rather than associative desorption of its fragments, which would instead have an activation barrier associated with H addition to the O

atom of the alkoxy and thus should be much less dependent on chain length. The y-intercept here (50 and 91 kJ/mol for O and Ti sites, respectively) is much larger than that for alkanes (7 kJ/mol). This is clearly due to the strong interaction of both the O and the metal sites with the $-\text{OH}$ group, and possibly hydrogen bonds between neighboring $-\text{OH}$ groups that are not present for the alkanes. The intercept is larger for the Ti sites due to the stronger interaction of $-\text{OH}$ with the metal sites than the O sites.

4.5. Comparison to Adsorption Calorimetry on Powdered Oxides

Cardona-Martinez and Dumesic⁸³ have reviewed calorimetry measurements of adsorption energies of a variety of molecules on powdered oxide samples, which had much more heterogeneous surface structures than the samples discussed above. These included studies of molecular adsorption on powdered oxides of Mg, Al, Si, Zn, Fe, and Ti. As might be expected, for a given metal oxide and molecule, those heats on powdered samples generally covered a much broader range than the heats reported above for single-crystalline oxide surfaces, which we attribute to the heterogeneity of sites on those powdered samples. Because of this complexity, we found it too challenging to identify other trends that we should mention here in comparison to the more well-defined single-crystal oxide surfaces, which are the focus of this Review. However, because powdered samples are used in most industrial applications of oxides as catalysts or sorbents, understanding their heterogeneous site distributions is also highly important. Also, for specific adsorbate/oxide combinations, we have found it very helpful for interpreting results on single-crystal samples to use information from published data on powdered samples, and vice versa. For example, our early study of water on $\text{TiO}_2(110)$ relied heavily on insights from TPD and FTIR data from powdered samples.¹⁴³ However, that

Table 4. Adsorption Enthalpies for Dissociatively Adsorbed Molecules on Oxide Surfaces, Based on TPD Analysis of Peaks for Their Associative Desorption^a

| dissociatively adsorbed molecule | oxide surface | adsorption site | T_p/K | $\beta/(\text{K}/\text{s})$ | $\log(\nu/\text{s}^{-1})$ | $-\Delta H_{ad}^0/(\text{kJ/mol})$ | citation |
|----------------------------------|---|---------------------------------|----------------|-----------------------------|---------------------------|------------------------------------|----------|
| O_2 | $\text{PdO}(101)$ | defects | 760 | 1 | 17 | 269 | 87 |
| H_2O | $\text{CeO}_2(001)$ | defects that expose metal sites | 275 | 2 | 17 | 93.5 | 96 |
| | $\text{TiO}_2(110)$ | defects | 507 | 1.5 | 17 | 176 | 123 |
| | $\text{TiO}_2(100)$ | metal | 340 → 320 | 1.8 | 17 | 116 → 109 | 99 |
| H_2O | $\alpha\text{-Cr}_2\text{O}_3(001)$ | metal | 355 | 2 | 17 | 121 | 100 |
| | $\alpha\text{-Cr}_2\text{O}_3(001)$ 2% strained | metal | 345 | 2 | 17 | 118 | 100 |
| | $\text{Fe}_3\text{O}_4(111)$ | metal | 282 → 268 | 5 | 17 | 93.8 → 89.0 | 101 |
| | $\text{Fe}_3\text{O}_4(001)$ | defects | 520 | 2 | 17 | 179 | 102 |
| | $\text{Fe}_3\text{O}_4(001)$ | metal | 325 → 260 | 2 | 17 | 111 → 88.2 | 102 |
| | $\alpha\text{-Fe}_2\text{O}_3(012)$ (1 × 1) | metal | 350 | 2 | 17 | 118 | 144 |
| | $\alpha\text{-Fe}_2\text{O}_3(012)$ (2 × 1) | metal | 380 → 405 | 2 | 17 | 130 → 139 | 144 |
| | $\text{PdO}(101)$ | defects | 354 | 1 | 17 | 123 | 104 |
| | $\text{Cu}_2\text{O}(100)$ | metal | 465 | 2 | 17 | 160 | 105 |
| | $\text{ZnO}(000\bar{1})$ | defects that expose metal sites | 315 | 7.5 | 17 | 104 | 106 |
| | $\text{ZnO}(10\bar{1}0)$ | metal | 450 | 1 | 17 | 157 | 108 |
| | $\alpha\text{-Al}_2\text{O}_3(0001)$ | metal | 395 | 1 | 17 | 138 | 145 |
| MeOH | $\text{TiO}_2(101)$ | defects | 410 | 1 | 17 | 143 | 98 |
| | $\text{TiO}_2(110)$ | defects | 480 | 2 | 17 | 165 | 124 |
| | $\text{ZnO}(10\bar{1}0)$ | ordered bilayer | 370 | 1.5 | 17 | 127 | 125 |

^aPrefactor and enthalpy values in bold were determined in the original paper by careful analysis of the TPD data. The remaining prefactors not in bold were assumed to be 10^{17} s^{-1} as justified in the text, and the corresponding enthalpies were estimated using eqs 6 and 3. For all of these species, the sticking probabilities are large enough to analyze TPD assuming negligible activation energy for dissociative adsorption.

type of integration of data requires a level of detailed analysis of the literature for specific systems that is beyond the scope of this Review.

5. REVERSIBLE DISSOCIATIVE ADSORPTION ON OXIDES: ADSORPTION ENTHALPIES BY TPD

As noted above, when adsorption is dissociative but the two adsorbed products have attractive interactions and thus prefer to occupy neighboring sites, or if they are immobile and simply remain at neighboring sites, their associative desorption kinetics can be treated as a pseudo-first-order process. Therefore, one can use eqs 4–6 to get E_d and, with eq 3, the enthalpy of adsorption. This is only valid when the adsorption \rightleftharpoons desorption process is reversible and the activation energy for adsorption is negligible (i.e., when the sticking probability is near unity). In Table 4, we have analyzed some cases in this way, mainly for cases where the two adsorbed fragments are expected to have attractive interactions (i.e., $-\text{OH}$ and $-\text{H}$ in the case of dissociatively adsorbed water and $-\text{OCH}_3$ and $-\text{H}$ in the case of dissociatively adsorbed methanol). On the basis of the gas exposures reported for all of these species (less than ~ 30 L), the initial sticking probabilities were estimated to be large enough (>0.05), given the surface temperature during exposure, that the activation energies for adsorption were negligible (and certainly below 7 kJ/mol).

In most cases, calculating the adsorption enthalpy for these dissociatively adsorbed species requires the use of an assumed prefactor for recombinative desorption. For this, we assumed a value of 10^{17} s^{-1} , based on the value we think is the most reliable prefactor actually determined experimentally for the associative desorption of similar species on single-crystal oxides, as reported for water on $\alpha\text{-Fe}_2\text{O}_3(012)$ (1 \times 1).¹⁴⁴ This prefactor is higher than that for desorption of molecularly adsorbed water. This is expected within transition state theory, because the adsorbed fragments ($-\text{OH}$ and $-\text{H}$ in the case of dissociatively adsorbed water) are expected to have a tighter binding to the surface, wherein free motions like rotations of the undissociated molecule have been converted into vibrational motion of the fragments with respect to the surface. Because vibrations contribute less to the partition function, this gives a lower partition function to the initial state for the reaction and thus a higher prefactor.

The number of systems in Table 4 are too few, and the assignments to associative desorption even for these are not so certain, so we do not see any trends in these data worth discussing, except to mention that the heat of adsorption for the dissociated molecule is larger than that for the molecularly adsorbed species on the same surface, especially for defect sites.

The energetics of the dissociative adsorption of H_2 on ZnO were measured by Griffin and Yates.¹⁴⁶ Although these results were obtained on ZnO powders, the three states observed were so beautifully characterized by infrared spectroscopy that one can hope to relate them to more recent observations on ZnO single-crystal surfaces. They observed three dissociatively adsorbed states for H_2 with distinct peaks in the TPD spectra for associative recombination. State I_a , which has a $\text{Zn}-\text{H}$ stretching frequency, $\nu(\text{Zn}-\text{H})$, of 1710 cm^{-1} , $\nu(\text{O}-\text{H})$ of 3455 cm^{-1} , and $T_p = 170 \text{ K}$, has a heat of adsorption of 31 kJ/mol and an activation energy for adsorption of 21 kJ/mol. States I_b and I_c both have $\nu(\text{Zn}-\text{H}) = 1710 \text{ cm}^{-1}$ and $\nu(\text{O}-\text{H})$ of 3498 cm^{-1} , but I_b has $T_p = 232 \text{ K}$ with a heat of adsorption of 52 kJ/mol and an activation energy for adsorption of 17 kJ/mol, and I_c has $T_p = 300 \text{ K}$ with a heat of adsorption of 57 kJ/mol.

mol and an activation energy for adsorption of 33 kJ/mol. The latter frequencies are not greatly different from the values of 1613 and 3670 cm^{-1} observed after dosing atomic H gas to the most stable face of ZnO , the (10̄10) surface, which also starts to desorb as H_2 at a similar temperature of 250 K upon heating in UHV.¹⁴⁷ In contrast, dosing H gas to the $\text{ZnO}(0001)\text{-Zn}$ surface leads to much higher temperature peaks in the removal rate of adsorbed H upon heating in UHV, at 383 and 536 K.^{148,149}

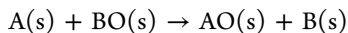
6. METAL ATOM ADSORPTION ON OXIDE SURFACES AND METAL/OXIDE INTERFACIAL ADHESION

Metal/oxide interfaces play key roles in many technologically important applications, including metal/oxide contacts in microelectronics and photovoltaic devices, metal/oxide seals in device and medical implant construction, coatings for corrosion passivation, and novel structural materials based on metal/ceramic composites. One would therefore like to understand the atomic-level structure of metal/oxide interfaces, the electronic character of the metal atoms at these interfaces, their interfacial chemical bond strengths to the oxide, and the thermodynamic stability of these interfaces. These must control their technologically relevant functional properties such as the efficiency of photovoltaic devices, the speed and size of microelectronics, the corrosion resistance of passivation layers, the peel strength of metal/oxide contacts, and the hardness of composite materials. Oxide surfaces that are decorated with submonolayer amounts of metals as either adsorbed cations or small metal nanoparticles are also extremely important in energy and environmental technologies as catalysts, electrocatalysts, photocatalysts, and gas sensors. Again, one would like to know the atomic-level structure of the surface, the electronic character of the metal atoms at these oxide surfaces, and their chemical bond strengths to the oxide, because these properties should correlate with the catalytic activity and selectivity of oxide-supported metal nanoparticles or cations, their resistance to sintering, and the sensitivity and lifetime of sensors. Our understanding of these key scientific questions about metals on oxide surfaces has improved considerably over the past two decades.^{39,150–171}

Here, we review progress that has been made in understanding the adsorption energy of isolated metal atoms to oxide surfaces and how that adsorption energy of metal atoms depends on coverage due to metal–metal bonding as metal particles grow for mid to late transition metals, or alternatively due to metal–metal repulsions for alkali metals. First, we start with a discussion of how chemical bonding enthalpies can be used to predict which chemical structure forms when a metal is deposited onto an oxide surface, and the observed relationships between interfacial chemical bonding strength as measured by metal atom adsorption energies and the adhesion energies at the thick metal film/oxide interface.

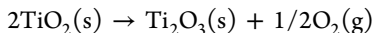
6.1. Predicting When the Adsorbing Metal Will Reduce the Underlying Oxide

It is easy to predict what bulk phase(s) should form at equilibrium (i.e., in the absence of any kinetic constraints) when a large amount of metal is dosed onto an oxide, because this simply depends on the relative thermodynamic stabilities of the various bulk oxides and intermetallic compounds that might form.¹⁵⁴ If metal A is deposited onto oxide BO, then A should reduce the surface of BO to metallic B and itself become oxidized to AO if the reaction



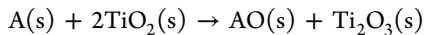
is thermodynamically downhill (i.e., if it has a negative standard free energy change). (Here, s will refer to solids, and g to gas.) Neglecting differences in formation entropies of the oxides, this occurs when the standard heat of formation, ΔH_f^0 , of the bulk oxide of A is more negative than that of the bulk oxide of B. It is reasonable to neglect entropy differences, because the entropies of formation of metal oxides (per mole of oxygen) are nearly independent of the metal.¹⁷² To take more complex stoichiometries like A_3O_4 into account, one should make this comparison using heats of formation per mole of oxygen, using the most negative value among all oxides of A (i.e., the value for the most stable oxide of A). Many of these heats of formation have been tabulated.¹³³ The late transition metals have the least stable oxides (least negative ΔH_f^0), and therefore the lowest affinity for oxygen. The affinity of transition metals for oxygen generally decreases from left to right across the periodic table.

If the substrate oxide can be easily reduced to a lower oxide, as in the case of TiO_2 :



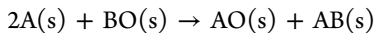
$$(\Delta H^0 = \Delta H_{f,Ti_2O_3}^0 - 2\Delta H_{f,TiO_2}^0 = 368 \text{ kJ/mol at } 298 \text{ K})$$

then one must also consider the possibility for reactions like:



This type of reaction should occur when ΔH_f^0 of the oxide of A is more negative than $-\Delta H_{\text{reaction}}^0$ for the reduction of the substrate to its lower oxide, when compared per mole of oxygen. Evidence for this is seen for several metals on rutile TiO_2 , for example.^{173–178}

If the two metals form stable intermetallic compounds, then one must also consider whether reactions like:



are thermodynamically downhill. This often occurs when depositing metals with very stable oxides onto alumina,^{179,180} or when depositing Al onto oxides,¹⁸¹ because metal aluminides tend to be very stable. Finally, one must consider any mixed oxides that are known to form. For example, $NiAl_2O_4(s)$ is known to form at the Ni/ Al_2O_3 interface, but only when the deposition is done in the presence of oxygen gas.¹⁸⁰ Heats of formation of many single metal oxides are conveniently tabulated.¹³³ Those of mixed oxides and intermetallic compounds are harder to find (see, for example, ref 182).

Experimental measurements of thick metal films on oxides at room temperature often fail to give these thermodynamically expected bulk phases, due to kinetic limitations (e.g., slow diffusion). However, the first monolayer usually shows evidence for the onset of the thermodynamically expected bulk reaction, and thin interfacial layers of the thermodynamically expected phases can often still be seen at thicker layers.^{154,173,177,179,180} This agreement implies that the energetics of metal adsorption in such cases where the adsorbing metal steals oxygen from the substrate oxide are similar to the bulk $\Delta H_{\text{reaction}}^0$ discussed for the above types of reactions.

Because this quantitative explanation of the observed reactivity trends is based on bulk heats of formation, and because heats of formation for both the metal and the oxide can depend on particle size (see below), finite size effects may be important. Thus, these predictions based on bulk thermodynamics will not always apply.

Note that for late transition metals on semiconducting oxides like $TiO_2(110)$ and $ZnO(0001)-O$, bulk thermodynamics predict neutral metal adsorption, and that is observed. However, even in these cases, it is common for the first few percent of a monolayer to donate electron density into the oxide and induce downward band bending on the order of a few tenths of an electronvolt.¹⁵⁴

6.2. Metal/Oxide Adhesion Energies and Wetting of Oxide Surfaces by Metal Films

Whether or not wetting occurs when metal is evaporated onto an oxide can be predicted on the basis of a comparison of the metal/oxide interfacial free energy, $\gamma_{m/\text{ox}}$, with the difference between the surface free energy of the clean oxide in vacuum, $\gamma_{v/\text{ox}}$, and that of the clean metal, $\gamma_{v/m}$.¹⁵⁴ If the metal wets the oxide, then $\gamma_{m/\text{ox}}$ equals $\gamma_{v/\text{ox}} - \gamma_{v/m}$ at equilibrium. In this case, a continuous metal film is formed whose thickness is simply related to the volume of metal deposited. If

$$\gamma_{m/\text{ox}} > \gamma_{v/\text{ox}} - \gamma_{v/m} \quad (17)$$

then the metal does not wet the oxide/vacuum interface.^{183,184} In this case, the metal should make thicker, three-dimensional (3D) particles and leave regions of clean oxide surface between particles.

The interfacial free energy, $\gamma_{m/\text{ox}}$, reflects the strength of metal–oxide bonding. All real interfacial energies γ are positive, and strong bonding between the phases at the metal/oxide interface would lead to small positive values of $\gamma_{m/\text{ox}}$. Because the surface free energy of metals is usually larger than or comparable to that of oxides,¹⁸⁵ eq 17 means that the metal/oxide interfacial free energy must be very small, or there must be very, very strong bonding at the metal/oxide interface, for wetting to occur.

The adhesion energy or the work of adhesion, E_{adh} , is the work needed to separate the metal/oxide interface in vacuum. It is given by:^{183,184,186}

$$E_{\text{adh}} = \gamma_{v/m} + \gamma_{v/\text{ox}} - \gamma_{m/\text{ox}} \quad (18)$$

Therefore, another way of specifying the thermodynamic criterion for wetting is simply that if wetting occurs at equilibrium:

$$E_{\text{adh}} = 2\gamma_{v/m} \quad (19)$$

If $E_{\text{adh}} < 2\gamma_{v/m}$, then wetting does not occur, and 3D metal particles are instead expected to form on the oxide surface.

Adhesion energies have been measured using the contact angle method for liquid metals on alumina, silica, MgO , and ZrO_2 , often under controlled inert gas or H_2 atmospheres (although not under conditions of proven surface cleanliness), and have been tabulated¹⁸⁵. A contact angle of less than 100° was never reproducibly observed for mid to late transition metals on any of these oxides.^{185–192} The values of E_{adh} were usually only 20–70% of $\gamma_{v/m}$ for these metals, and thus a factor of at least 3 too low for wetting. Contact angles have also been measured for liquid metals on more reducible oxides (ZnO , chromia, etc.),^{192,193} and even here the late transition metals usually have a contact angle near or above 90° . Assuming that the solid metal has an interfacial energy on the oxide similar to that of the liquid metal, and realizing that $\gamma_{v/m}$ is even larger for the solid than for the liquid metal (typically by $\sim 18\%$ ¹⁹⁴), this indicates that these metals as solids also should not wet such oxides. Indeed, the mid to late transition metals as solids do not wet such oxides, in the thermodynamic sense, under clean

UHV conditions, but instead form 3D solid particles on these surfaces.¹⁵⁴ Adsorbed gases also influence the wetting thermodynamics: the adsorption of gases like CO that can bind much more strongly to metals than to these oxides can add a large enthalpic driving force for wetting.¹⁵⁴

6.3. Relating Metal Atom Adsorption Energies with Metal/Oxide Adhesion Energies and Sublimation Energies of the Bulk Metal

Metal atom adsorption enthalpies have been connected to adhesion energies by a thermodynamic cycle.¹⁵⁴ That cycle proved that the integral heat of adsorption per mole, $q_{\text{ad,int}}$, at some multilayer coverage where the differential heat of adsorption has just reached the bulk heat of sublimation of the metal per mole, ΔH_{sub} , is given by:

$$q_{\text{ad,int}} = \Delta H_{\text{sub}} - (2\gamma_{v/m} - E_{\text{adh}})/(n/A) \quad (20)$$

where n/A is the coverage in moles of metal atoms per unit area. We used here the convention adopted above that both $q_{\text{ad,int}}$ and ΔH_{sub} are positive, and neglected entropy. For metals that do not wet, $q_{\text{ad,int}} < \Delta H_{\text{sub}}$. Roughness factors must be incorporated into the above derivation to account for any surface roughness of the multilayer metal film, which is done by simply replacing $2\gamma_{v/m}$ with $(1 + f_r)\gamma_{v/m}$, where f_r is the roughness factor.¹⁵⁴ This can even be applied to cases where the metal film is not continuous but instead is in the form of large particles, as shown below.

If we imagine the hypothetical case where the metal had grown in a layer-by-layer fashion, and assume that the adsorption energy of a metal onto an oxide is equal to its sublimation energy in all layers beyond the first monolayer, the (hypothetical) integral heat of adsorption in the first monolayer is given from the above equation as:

$$q_{\text{ad,int,ML}} = \Delta H_{\text{sub}} - (2\gamma_{v/m} - E_{\text{adh}})/(n_1/A) \quad (21)$$

where n_1/A is the coverage for one ML. Combining this with the result that E_{adh} is usually 20–100% of $\gamma_{v/m}$ for late transition metals on alumina, silica, and zirconia,¹⁵⁴ we have shown that:¹⁵⁴

$$q_{\text{ad,int,ML}} = \Delta H_{\text{sub}} - (1.4 \pm 0.4) \cdot \gamma_{v/m} / (n_1/A) \quad (22)$$

Overbury et al.¹⁸⁵ have shown from experimental data for many solid metals that:

$$\gamma_{v/m} = (0.16 \pm 0.02) \cdot (n_1/A) \Delta H_{\text{sub}} \quad (23)$$

Substituting this into eq 22 gives a simple way to estimate heats of adsorption for late transition metals on those oxides:¹⁵⁴

$$q_{\text{ad,int,ML}} = (0.77 \pm 0.09) \Delta H_{\text{sub}} \quad (24)$$

This estimate is based upon surface free energies and adhesion energies measured without the aid of tests that prove surface cleanliness. Experimental measurements of the heats of adsorption for late transition metals on MgO(100), CeO₂(111), Fe₃O₄(111), alumina, and silica (summarized below) are at least qualitatively consistent with this prediction that $q_{\text{ad,int,ML}}$ is some fraction of ΔH_{sub} , but we cannot yet verify that this fraction is generally in the range 0.77 ± 0.09 . Using that E_{adh} is usually 20–100% of $\gamma_{v/m}$ for such systems, together with eq 23, we showed that:¹⁵⁴

$$E_{\text{adh}} = (0.10 \pm 0.07) \cdot (n_1/A) \Delta H_{\text{sub}} \quad (25)$$

This gives a very imprecise way of estimating the range of adhesion energies for such systems.

6.4. SCAC Studies of Metal Adsorption Enthalpies on Single-Crystal Oxide Surfaces

Our group has calorimetrically measured the heats of adsorption of a variety of different metal atoms onto a number of different single-crystal oxide surfaces, including MgO(100), CeO₂(111), and Fe₃O₄(111).^{28,39,195–207} Example heats of adsorption versus coverage data are shown in Figure 10,

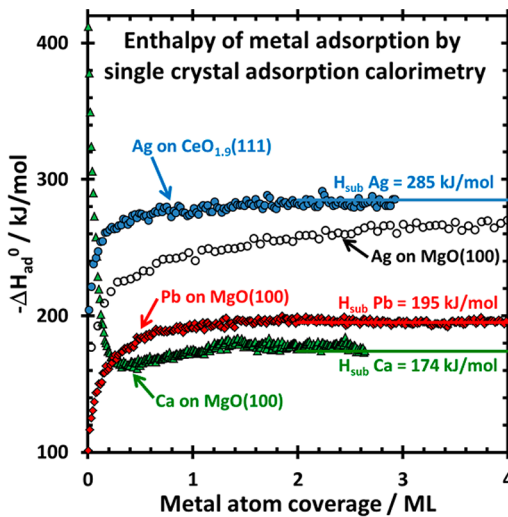


Figure 10. Example heats of adsorption versus coverage data for metals on single-crystal oxides as measured by SCAC at 300 K. Data are shown for Pb, Ag, and Ca on MgO(100) as well as Ag on CeO₂(111) (with 5% oxygen vacancies in XPS probe depth). Data from refs 198,200,202,206 where these original papers show data to higher coverages. One monolayer here is defined as the number of oxygen ions per unit area in the topmost atomic plane ($1.12 \times 10^{15} \text{ cm}^{-2}$ for MgO(100) and $7.9 \times 10^{14} \text{ cm}^{-2}$ for CeO₂(111)). Solid horizontal lines mark the bulk heats of sublimation from the literature.

expressed here as the standard enthalpies of adsorption, ΔH_{ad}^0 , at the stated temperature (where standard simply implies one bar gas pressure). These calorimetric measurements have allowed us for the first time to directly assess the energetic stability of metal atoms on a well-defined oxide surfaces and that of metal atoms within metal nanoparticles supported on these oxide surfaces. Here, we review those studies, showing how the heat of metal atom adsorption, its coverage dependence, and the metal adhesion energy are determined by the position of the metal in the periodic table, the nature of the oxide material, and the presence of hydroxyls, steps, and oxygen vacancies on the oxide surface. Finally, we show how the stability of oxide-supported metal clusters depends on cluster size and the nature of the oxide surface.

6.4.1. Adsorption Enthalpies of Different Metal Atoms on Defective MgO(100). Our studies of metal adsorption enthalpies on MgO(100) used ordered, 4 nm-thick MgO(100) thin films grown epitaxially on Mo(100).^{28,195,197–204} These MgO(100) surfaces contain ~5% defect sites, mainly step and kink sites.^{204,208} Example measurements are shown in Figure 10. Heats of adsorption for Ca, Li, Cu, Ag, and Pb measured at 300 K are summarized in Table 5, where they also are compared to DFT calculations for terrace, step, and kink sites when available.

Table 5. Comparison of the Initial Heats of Adsorption (ΔH_{ad}^0) Measured Calorimetrically for Selected Metals on MgO(100) at 300 K with Values for the Adsorption Energy of Isolated Metal Atoms on the Most Stable Sites Where They Can Adsorb on Terraces, Steps, and Kinks Calculated with DFT Slab Models at 0 K^a

| System | $-\Delta H_{ads}^0$ (kJ/mol) | S_0 (experimental) | ΔH_{sub} (bulk) | - DFT Adsorption Energy (kJ/mol) | | |
|---------------|---------------------------------|-------------------------|----------------------------|--|------------------------|------------------------|
| | | | | Terrace | Step | Kink |
| Ca / MgO(100) | 410 ²⁰² | 1.00 ²⁰² | 178 | 82 ^{202,209} | 205 ^{202,209} | 376 ^{202,209} |
| Li / MgO(100) | 260 ²⁰³ | 0.97 ²⁰³ | 159 | 78 ^{203,204} 58, 85 ²¹⁰ | 161 ^{203,204} | 343 ^{203,204} |
| Cu / MgO(100) | 240 ¹⁹⁷ | 1.00 ¹⁹⁷ | 337 | 60 ²¹¹ , 90 ²¹² , 91 ²¹³ | 144 ²¹³ | 228 ²¹³ |
| Ag / MgO(100) | 176 ¹⁹⁸ | 0.94 ¹⁹⁸ | 285 | 52 ²¹⁴ , 38 ²¹¹ 47 ²¹⁵ | - | - |
| Pb / MgO(100) | 103 ²⁰⁰ | 0.70 ²⁰⁰ | 195 | - | - | - |

^aIncluded are also the measured initial sticking probability (S_0) and the heat of sublimation of the bulk metal (ΔH_{sub} , from ref 133). Light gray spheres represent oxygen atoms, black magnesium, and light blue adsorbed metal atoms. Reprinted with permission from ref 39. Copyright 2009 Elsevier.

The calorimetry results in Table 5 are probably best understood for the cases of Ca and Li on MgO(100), because these calorimetry studies also included complementary DFT calculations and kinetic simulations by our collaborators (Graeme Henkelman and Lijun Xu).^{202,204,209,216} The calorimetry and film morphology measurements for the slightly defective MgO(100) surface and this surface after intentionally adding increasing numbers of defect sites (mainly steps, with some kinks) were well fitted by a kinetic model that included the following heats of adsorption: defect sites (mainly steps) = 420 kJ/mol for Ca and 400 kJ/mol for Li, and terrace sites at the edges of 2D clusters = 174 kJ/mol for Ca and 159 kJ/mol for Li. According to DFT, the binding energies at steps and kinks are 205 and 376 kJ/mol for Ca and 161 and 343 kJ/mol for Li, respectively. It thus appears that DFT must be underestimating the strength of Ca– and Li–MgO binding at steps by ~50%. According to DFT, the binding energies at the edge of 2D islands on terraces are 100 and 116 kJ/mol for Ca and Li, respectively, which is again too low, now by 30–40%.

According to DFT,^{204,209,216} small 2D clusters of Li atoms nucleated at step edges are more stable than Ca atom clusters, which tend to dissociate at room temperature. That is, for the case of Li, when a third metal adatom diffuses to a terrace site nearest to two neighboring metal adatoms both bound on a step edge, it makes a stable trimer, whereas for the case of Ca it would continue migrating until it found a third defect site or a 3D Ca particle. The kinetic simulations mentioned above included this effect, and proved that it can explain the observed tendency for Li to maintain 2D growth to higher coverages than Ca.²⁰⁴

These DFT calculations showed charge transfer from adsorbed Ca and Li monomers to the MgO(100) terrace of -0.24 e and -0.35 e, respectively, and much more at steps.^{209,216} In agreement, the work function was observed to decrease between 0 and 0.5 ML by 1.1 and 1.8 eV for Ca and Li, respectively.^{202,203} It is surprising that despite their large charges and the expected charge–charge and dipole–dipole repulsions, both Ca and Li adatoms show attractive interactions and 2D clustering on MgO(100) in both experiments and DFT.^{202–204,209,216}

The heats of formation of CaO (-152 kJ/mol O) and Li₂O (-141 kcal/mol O) are very similar to that for MgO (-144 kJ/mol), such that some transfer of oxygen from the lattice to the admetal might be expected on the basis of thermodynamics. This was not observed, but the low temperature (300 K) may have prevented overcoming an activation barrier.

In contrast to the case of Ca and Li on the left side of the periodic table, the metals Cu, Ag, and Pb from the right side of the periodic table do not bind very strongly to the steps and kinks on MgO(100). One can conclude this easily by looking at their heat of adsorption versus coverage curves (Figure 10), which start low and increase toward the heat of sublimation with coverage,^{28,195,197–201} exactly the opposite as seen for Ca and Li.^{202,203} This very weak bonding of late transition metals to step sites on MgO(100) is supported by DFT calculations, which found that a palladium atom has an adsorption energy of only ~ 185 kJ/mol at steps, which is only about one-half of its heat of sublimation of 377 kJ/mol but is still ~ 47 kJ/mol stronger than adsorption at terrace sites.²¹⁷ The same trend is seen in the DFT results in Table 5 for Cu at steps and kinks on MgO(100) by Henkelman (private communication).

Metals from the right side of the periodic table (Cu, Ag, and Pb) show correlations between their measured heats of adsorption on MgO(100) and their bulk heats of sublimation, sticking probabilities, and film growth morphologies.¹⁹⁵ These metals were all found to grow as 3D clusters on MgO(100). Late transition metals are typically observed to nucleate at step edges when microscopy data are available.^{151,153,154,161,162,218} At the lowest coverage studied ($\sim 2\%$ of a monolayer), these metals are probably adsorbed at step and/or kink sites, possibly in tiny, two-dimensional (2D) clusters. The measured initial heats of adsorption in Table 5 thus include not only the bond energies of these metal atoms to the step edges on the MgO(100) surface, but possibly some contribution from metal–metal bonding. As seen in Table 5, the initial heats of adsorption for these three metals increase with their bulk sublimation enthalpies, and their initial sticking probabilities at 300 K increase with their initial heats of adsorption.¹⁹⁵ The resulting saturation number densities of metal particles also were found to increase with the magnitude of their initial heats of adsorption.¹⁹⁵ (The number of clusters per unit area grows

initially with coverage, but quickly reaches a saturation value at very low coverage.^{154,219–221}) This supports a transient mobile precursor model for adsorption,¹⁹⁵ which is consistent with DFT-calculated energetics for adatoms at terrace sites (see Table 5) and with estimated diffusion barriers. It is also consistent with classical mechanistic/kinetic models developed by Venables to explain electron microscopy observations of cluster nucleation and growth for such systems.^{219–222}

The effect of surface hydroxyl groups on the adsorption energies of Cu and Pb on MgO(100) was also investigated.²⁰¹ It was found that surface hydroxyls increase the initial heat of adsorption for both metals (by ~10 and 20 kJ/mol, respectively). The saturation number density of metal nanoparticles also increased, consistent with the trends and nucleation/growth model mentioned above.

As noted previously, the adhesion energy between a multilayer metal film and the underlying oxide surface can also be determined from the integral heat of metal adsorption on the oxide.^{25,26,154} This was done for several systems.^{28,197–200} On MgO(100), the reported adhesion energies are: Pb = $77 \pm 20 \mu\text{J}/\text{cm}^2$, Ag = $30 \pm 30 \mu\text{J}/\text{cm}^2$, and Cu = $\sim 192 \pm 50 \mu\text{J}/\text{cm}^2$. Thus, the adhesion energy does not clearly increase with the initial heat of adsorption and the bulk sublimation enthalpy (see Table 5), as one might expect. That the value for Pb is higher than Ag may be related to the fact that Pb–O bonding is much stronger than Ag–O bonding, as evidenced by the much larger heat of formation (per mole metal) for the most stable bulk oxide of Pb than for that of Ag.¹³³ These adhesion energies have been discussed together with adhesion energy data from contact angle measurements for Pd on MgO(100),¹⁹⁵ where it was found that these adhesion energies correlate with the sum of the magnitudes of the metal's bulk sublimation enthalpy plus the heat of formation of the bulk oxide of the metal per mole of metal atoms. This suggests that local chemical bonds, both metal–oxygen and covalent metal–Mg, dominate the interfacial bonding. Similarly, STM observations of whether metals grow as flat 2D films or as 3D particles when deposited onto TiO₂(110) were shown to correlate with a combination of the metal's bulk sublimation enthalpy and the heat of formation of the bulk oxide of the metal per mole of metal atoms.²²³

For metals that grow as 3D particles, heat of adsorption versus coverage data of the type shown in Figure 10 can be replotted as heat of adsorption versus average particle size, if the mapping between coverage and average particle size can be determined. We did this first for the case of Pb on MgO(100),¹⁹⁶ as shown in Figure 11. Careful measurements of Pb and MgO peak intensities versus coverage in Auger electron spectroscopy (AES) were well fitted by a quantitative intensity model (with accurate, *in situ* measurements of relative sensitivities and mean-free paths) assuming that the Pb grows as three-dimensional (3D) Pb particles with a fixed number density (N) of 8×10^{11} particles/cm², independent of Pb coverage.²⁰⁰ As noted above and shown in many experiments and by Venables' kinetic models,^{219–221} it is common for such systems that as metal is first deposited the number of nuclei at first increases, but after only a few percent of a monolayer the number density of clusters reaches a saturation value, N_{sat} and stays constant thereafter (until the particles start growing so large that they touch neighboring particles, after which N decreases). Thus, the assumption of a constant number density for the coverage range applied is justified. It was further assumed that the particles have the shape of a hemispherical

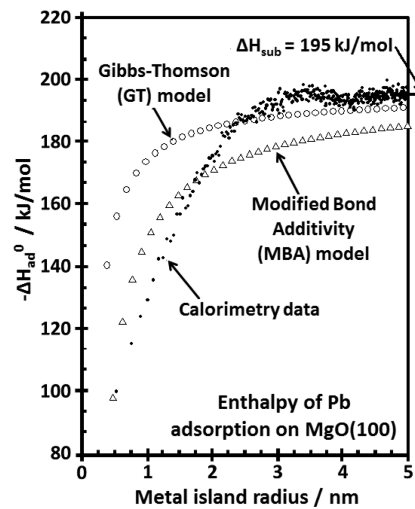


Figure 11. Heat of adsorption of Pb onto Pb nanoparticles on MgO(100) versus average Pb particle radius. Also shown is the Gibbs–Thomson (GT) model of eq 26, which assumes that the surface energy is the bulk value, independent of particle size. This is seen to fit the experimental data very poorly at small radii. In contrast, the modified bond additivity (MBA) model, which is also shown (see details in text), is a much better estimate for the experimental data. Adapted with permission from ref 196. Copyright 2002 American Association for the Advancement of Science.

cap. The data are not sensitive to the exact shape of the 3D particles, and are equally well fitted by any shape with an aspect ratio (thickness ÷ length parallel to the oxide surface) of $\sim 1:3$. Dividing the Pb coverage (atoms/cm²) by N_{sat} (particles/cm²) gives the average number of Pb atoms per particle at any given Pb coverage, which can be combined with the bulk density of Pb (atoms/cm³) to give the average particle volume (V) at each coverage. This hemispherical volume then gives the average Pb particle's effective diameter at that coverage: $d = (6V/\pi)^{1/3}$.

We were thus able to plot the heat of adsorption versus Pb coverage data from Figure 10 instead as heat versus Pb particle radius,¹⁹⁶ as shown in Figure 11. As can be seen, the heat of adsorption decreases dramatically with particle effective radius below 3 nm (diameters below 6 nm). This is due to the fact that when a Pb atom adsorbs to a very small Pb cluster, it makes fewer Pb–Pb bonds than it does to a very large Pb particle, where it makes six Pb–Pb bonds, on average. For example, when a fourth Pb atom adds to a Pb trimer, it makes only three Pb–Pb bonds. Also, the bonds of Pb atoms to the underlying MgO are weaker than Pb–Pb bonds.

A widely used approach for estimating the dependence of particle energy on size has been to use the Gibbs–Thompson (GT) relation, which states that the chemical potential (partial molar free energy) of a metal atom in a particle of radius R , $\mu(R)$, differs from that in the bulk, $\mu(\infty)$, by:

$$\mu(R) - \mu(\infty) = 2\gamma\Omega/R \quad (26)$$

where γ is the surface free energy of the metal and Ω is the volume per atom in the bulk solid.²²⁴ Neglecting entropy differences, this gives that:

$$\Delta H_{\text{ad}}(R) + \Delta H_{\text{sub}} = \mu(R) - \mu(\infty) = 2\gamma\Omega/R \quad (27)$$

remembering that we define ΔH_{ad} as a negative number in this Review. As seen in Figure 11, this GT model severely overestimates the stability of Pb in small Pb particles, by ~60 kJ/mol at 1 nm radius. This is because the surface energy

increases substantially as the radius decreases below ~ 3 nm, because the average coordination number of the surface atoms decreases. This is the same reason more open or stepped crystal facets of metals (i.e., where the metal atoms have lower coordination numbers) have higher surface energies.^{225,226}

The simple, modified pairwise bond-additivity (MBA) model shown in Figure 11 reproduces the dramatic dependence of adsorption enthalpy on cluster size surprisingly well. In this MBA model, described in detail elsewhere,^{196,227} the energies of discrete, compact clusters were calculated assuming that all metal–metal bond energies equal their bulk value (32.5 kJ/mol for Pb, which is 1/6 of the sublimation energy of the bulk solid¹³³). Very stable cluster shapes were chosen by adding successive hexagonal close-packed layers. The effective radius, R , of each such cluster was calculated from its volume (V) assuming hemispherical shape using the equation $V = (\text{number of atoms per cluster}) \cdot \Omega = 2\pi R^3/3$. The energies for other cluster sizes were assumed to vary linearly with radius between these compact clusters, thus modifying true bond-additivity. There are two compensating errors in this MBA model. First, metal–metal bond energies actually increase as the coordination number of the metal atoms involved decreases.^{228,229} Second, MBA interpolates linearly between points calculated only for the most compact clusters, whereas atoms in most small clusters are actually less stable due to their lower average coordination number. Because these errors roughly compensate, there is reasonable agreement with the data.

We also used molecule beam/surface scattering of a beam of Pb atoms from an MgO(100) surface (prepared in the same way as prepared for the SCAC measurements above) to mass-spectrometrically determine the surface residence times of Pb adatoms on this surface at 300 K. We measured the average lifetimes of the Pb adatoms, which transiently adsorbed but did not permanently stick on the MgO(100) surface at 300 K (while the other 70% stick permanently to Pb clusters on the MgO), and extracted from these the heats of adsorption of these transiently adsorbed Pb adatoms, resulting in heats of 69–78 and 92–101 kJ/mol for the two weakest adsorption sites.⁷⁹ These may be attributed to monomers (or clusters smaller than the critical nucleus size) at terrace and step sites, respectively. (“Critical nucleus size” here is defined, based on its use in kinetic models for nucleation and growth of metal clusters during metal vapor deposition onto oxide surfaces,^{154,219} as the size wherein the metal atoms have the highest chemical potential. Smaller clusters spontaneously decompose, but large clusters are thermodynamically stable and continue to grow.) The initial heat of adsorption measured calorimetrically at 300 K (103 kJ/mol, Table 5) is slightly larger than the heat of adsorption at steps, consistent with cluster formation on the surface during the first gas pulse during calorimetry. This initial calorimetric heat of adsorption was almost identical at 190 and 300 K.^{28,200} Given the strong increase in heat with cluster size noted above, this implies that the same average cluster size was formed in the first pulse of metal gas at 190 and 300 K, even though the saturation number density of clusters was much larger at 190 K than at 300 K and took more pulses to reach.²⁸ Using the saturation number density of clusters measured at higher coverage and 300 K (8.1×10^{11} clusters/cm²) and the average coverage during the first pulse (1.2×10^{13} atoms/cm²)²⁰⁰ gives that these clusters contain 15 Pb atoms on average during the first pulse’s heat measurement.²⁰⁰ For Ag on MgO(100), this number is 12 atoms at 300 K.¹⁹⁸

Oxide-supported metal nanoparticles are among some of the most important heterogeneous catalysts in use today. These metal particles supported on oxides often sinter or ripen with time during standard industrial operation, starting from a collection of many small, highly dispersed particles and eventually converting to their thermodynamically preferred state: fewer, larger particles.^{154,224,230–245} Thus, understanding the kinetics of sintering is quite important. Before the results of Figure 11 were published, the use of the GT relation was implicit in all atomistic models for catalyst sintering^{239–241} starting with the pioneering models of Wynblatt and Gjostein.^{224,230} We have shown that when incorporated into kinetic models for catalyst particle sintering, the MBA model helps provide a much more accurate kinetic model for sintering, with physically more reasonable parameters, and it helps explain previous anomalies in sintering kinetics.^{196,227} It also helps explain the size-focusing observed in colloidal nanoparticle growth from liquid solutions.²⁴⁶

6.4.2. Silver Atom Adsorption Enthalpies on Different Oxide Surfaces.

To assess how different oxides affect the stability of nanoparticles of the same metal, SCAC was used to measure the adsorption enthalpies of Ag atoms onto several different oxides: the MgO(100) surface, two slightly reduced CeO₂(111) surfaces, and the Fe₃O₄(111) surface. The Ag film morphology was measured versus Ag coverage at 300 K by measuring the AES and He⁺ ISS peak intensities for the Ag and for the oxide elements (O and/or the oxidized metal) versus Ag coverage. For all of these oxide surfaces, these AES and ISS data were well fitted by assuming the Ag particles have the shape of hemispherical caps, with a fixed number density that is independent of Ag coverage after the first 2% of a ML,^{198,205} where the fits were shown to give saturation Ag particle densities (N) of 2.5×10^{12} , 4×10^{12} , and 4×10^{12} particles/cm² for MgO(100), CeO₂(111), and Fe₃O₄(111), respectively. This value of N was the same for CeO₂(111) independent of whether the surface had a reduced stoichiometry of CeO_{1.9}(111) or CeO_{1.8}(111) within the probe depth of XPS. For the less reduced CeO_{1.9}(111) surface, most of the oxygen vacancies are thought to reside at the step edges.²⁰⁵ (Calculations by DFT generally indicate that oxygen vacancies are much more stable at step edges than on terraces of oxide surfaces.) Dividing the Ag coverage (atoms/cm²) by N (particles/cm²) gives the average number of Ag atoms per particle at any given Ag coverage, which is converted to the average Ag particle diameter at that coverage just as described above for Pb on MgO(100).

Figure 12 shows the measured heat of adsorption of Ag gas atoms on these four oxide surfaces plotted versus the average Ag particle diameter to which it adds, using the above approach to convert from Ag coverage to Ag particle diameter. As can be seen, the heat of adsorption increases rapidly with Ag particle size (coverage) on all these oxides, but reaches a saturation value for large silver particles, which is indistinguishable from the bulk heat of Ag sublimation (285 kJ/mol,¹³³ shown by the horizontal line).

Figure 12 shows that there are large differences between the different surfaces in the stability of metal atoms adding to particles of the same size. Most notably, Ag atoms bind much more strongly to sub-4 nm Ag particles on the Fe₃O₄(111) and reduced CeO₂(111) surfaces than to the same size particles on MgO(100). When a pulse of metal atoms adds to the particles, some add on the tops and sides of the particles but some add to the perimeters, where they bind to the oxide as well. The

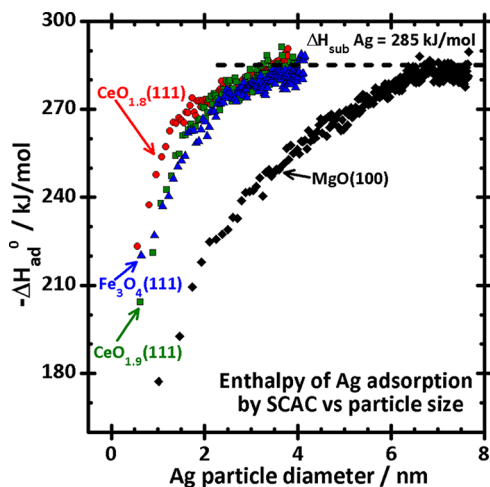


Figure 12. The heat of Ag atom adsorption during experiments where Ag is vapor deposited onto oxide surfaces under conditions (300 K) where the Ag atom transiently adsorbs on clean parts of the oxide surface but quickly diffuses across the surface and adds to growing Ag particle on the surface. Plotted here is the measured heat of Ag atom adsorption versus the Ag particle diameter to which it adds (i.e., the average Ag particle size at the Ag coverage corresponding to that heat value). Data are shown for four different surfaces: $\text{Fe}_3\text{O}_4(111)$ thin film and two $\text{CeO}_2(111)$ thin films with different extents of surface reduction ($x = \sim 0.1$ and 0.2 in CeO_{2-x}), all grown on Pt(111) to 4 or 5 nm thickness, and a 4 nm thick $\text{MgO}(100)$ film grown on Mo(100). The data for $\text{Fe}_3\text{O}_4(111)$ are from ref 207, and those for $\text{CeO}_2(111)$ and $\text{MgO}(100)$ are from ref 205. Adapted with permission from ref 207. Copyright 2011 Royal Society of Chemistry.

difference in average adsorption energy may come from this nearest-neighbor bonding difference, with perhaps a lesser contribution from next-nearest-neighbor sites. Also, the growing Ag lattice may adopt its lattice parameter to that of the oxide surface, and vice versa, thus providing sites for the next Ag atom where the Ag–Ag bond energies are different due to lattice strain effects. For example, a slightly stretched oxide lattice might provide thermodynamically more stable sites for Ag adsorption. This type effect cannot continue forever, because lattice strain builds up as the Ag island gets larger.

In all four oxide surfaces, the metal particles are probably nucleated mainly at step edges,^{151,153,154,161,162,205,218,247} but the particles are big enough in the 1.5–4 nm range that most of the metal atoms at the metal/oxide interface are not directly bonding to oxide step atoms, but instead bind to terrace atoms. This can be seen, for example, in the STM image of Ag particles grown on this same type of $\text{CeO}_2(111)$ film (here only 2.6 nm thick) by Luches et al.²⁴⁷ (Figure 13). Thus, these heat data indicate that the bonding of Ag particles to the oxide is stronger also at the terrace sites of $\text{Fe}_3\text{O}_4(111)$ and reduced $\text{CeO}_2(111)$ than $\text{MgO}(100)$.

The data in Figure 12 are all for oxide thin films that are 4 nm thick, grown on a metal single-crystal support. For $\text{CeO}_2(111)$, we also measured heats of Ag adsorption using oxide films that were only 1, 2, and 3 nm thick (all grown on Pt(111)). While the 2, 3, and 4 nm films all gave the same results as shown here, the 1 nm thick oxide gave considerably higher heats of adsorption for the same particle size, by 20–50 kJ/mol for Ag particles below 1.5 nm diameter.²⁰⁵ This indicates that 1 nm oxide films are not thick enough to represent the bulk, whereas 2 nm and above are. In this case, the Ag feels additional attraction to the surface when the CeO_2

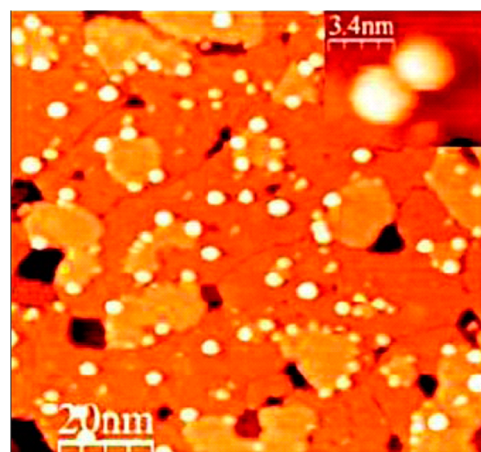


Figure 13. An STM image of Ag nanoparticles grown on the same type of $\text{CeO}_2(111)$ film on Pt(111) as in Figure 12 (here only 2.6 nm thick). Reprinted with permission from ref 247. Copyright 2012 American Chemical Society.

film is only 1 nm thick, probably due to long-range electronic interactions with the underlying Pt(111) substrate. Other related effects have been observed experimentally and theoretically in this ≤ 1 nm thickness range, with the extent of charging of the adsorbed metal even being affected by oxide thickness.^{165,203,214,248}

Another way to view the data in Figure 12 is to plot the enthalpy of a metal atom after it adds to a particle relative to its enthalpy in bulk Ag (or the partial molar enthalpy) versus particle size, as shown in Figure 14. In this figure, we express

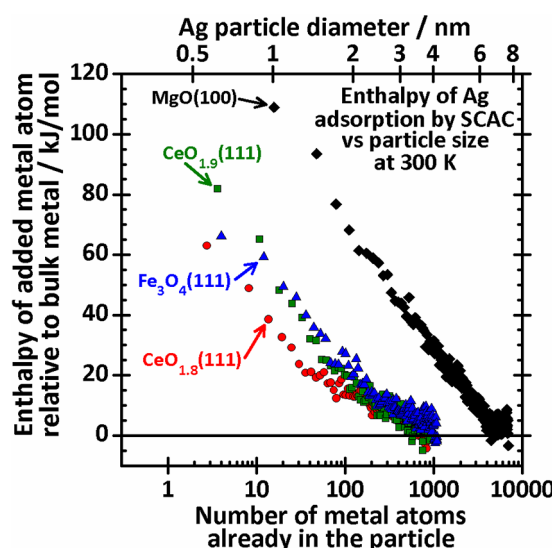


Figure 14. Partial molar enthalpy of Ag atoms in Ag nanoparticles (i.e., the enthalpy of the last Ag atom to be added to the particle (relative to bulk solid Ag)) versus the average Ag particle size for Ag adsorption on different oxide surfaces. These enthalpies were taken from the data in Figure 12.

particle size as the number of metal atoms per particle, and also as effective diameter along the top axis. The increase in stability with particle size in all of these curves is dominated by the effect of particle size on the number of metal–metal bonds per atom, as it was in Figure 11. The Pb data for $\text{MgO}(100)$ from Figure 11 fall almost on top of the Ag/ $\text{MgO}(100)$ data (as

shown in ref 205, where they are presented in the same plot). These MgO(100) data are distinctly different from the Ag data for the CeO_{2-x}(111) and Fe₃O₄(111) surfaces. As seen, Ag atoms are 30–70 kJ/mol more stable in Ag nanoparticles for any given size smaller than ~1000 atoms when those particles are attached to CeO_{2-x}(111) and Fe₃O₄(111) surfaces than when attached to MgO(100) surfaces. This difference gets smaller for larger particles, and essentially disappears by ~5000 atoms/particle, where the energy of the added metal atom reaches the stability of the bulk solid even on MgO(100).

The curves in Figure 14 directly reflect the thermodynamic driving force for nanoparticle sintering. If a metal atom is on a relatively small particle within a collection of particles on an oxide, it is less stable and prefers to migrate to a larger particle where it is more stable (i.e., move down and to the right on each of these curves until it reaches the minimum, or zero). Such migration of individual monomers from smaller to larger particles (typically by diffusion across the surface of the oxide) is referred to as Ostwald ripening and is the same effect that gives rise to raindrops in clouds, where water monomers migrate through the gas. Similarly, it is downhill in enthalpy for two small particles to diffuse together and form one larger particle. This mechanism for sintering is called particle diffusion/coalescence. Both mechanisms have been observed experimentally (see refs 224,227,230,231 and references therein).

The enthalpic driving force for sintering shown in Figure 14 drops below 10 kJ/mol already for ~400-atom (3 nm) particles on the CeO_{2-x}(111) and Fe₃O₄(111) surfaces, but similar energies are not reached until ~3000-atom (6 nm) particles on MgO(100). Clearly, sintering will stop at much smaller particles on CeO₂ and Fe₃O₄(111) surfaces! Because Au nanoparticles are very active for several catalytic reactions when 3 nm in diameter but almost completely inactive above 6 nm,^{249–254} this range of particular sizes is critical. Our derivation of kinetic rate equations for sintering by both mechanisms showed that this enthalpy in Figure 14 is exponentially reflected in the sintering rate, as a negative contribution to the apparent activation energy.^{196,227,246} Thus, the sintering rates for small particles should be much slower on CeO₂ and Fe₃O₄(111) surfaces than on MgO(100). This is consistent with observations that ceria offers a more sinter-resistant support for late transition metals than other oxides.^{255,256}

In Figure 14, we also see that small Ag nanoparticles (<1.5 nm or 30 atoms) on CeO_{2-x}(111) are ~15 kJ/mol more stable on the more reduced CeO_{1.8}(111) surface than on CeO_{1.9}(111). This increase in stability with vacancy concentration is consistent with DFT calculations that Ag adatoms bind >100 kJ/mol more strongly to vacancy sites on CeO_{2-x}(111) than to stoichiometric sites.²⁵⁷

We have integrated the measured heat versus coverage curves (up to the coverage where the heat reaches the bulk sublimation energy), for each of these oxide surfaces, and extracted from that integral the adhesion energies for Ag nanoparticles to these oxide surfaces using eq 20 and the roughness factor of hemispherical caps (=2). This is exactly the same procedure as outlined in ref 198, which gave an adhesion energy of 0.3 J/m² for Ag on MgO(100). In all cases, we assumed a hemispherical shape for the Ag nanoparticles. The results are summarized in Table 6.

These results show that the adhesion energies of Ag nanoparticles to CeO₂(111) and Fe₃O₄(111) are much larger than for the same particles to MgO(100), and that this

Table 6. Calorimetrically Measured Adhesion Energies of Ag Nanoparticles to MgO(100), Two Reduced CeO_{2-x}(111) Surfaces and Fe₃O₄(111), and the Initial Heats of Ag Adsorption ($\Delta H_{\text{ad,init}}^0$) for the First Pulse (~0.03 monolayer) of Ag Gas at 300 K^a

| substrate surface | Ag adhesion energy/(J/m ²) | Ag coverage/atoms/cm ² | Ag particle size/nm | $-\Delta H_{\text{ad,init}}^0$ / (kJ/mol) |
|--------------------------------------|--|-----------------------------------|---------------------|---|
| MgO(100) | 0.3 ± 0.3 ¹⁹⁸ | 9.6 × 10 ¹⁵ | 6.6 | 176 |
| CeO _{1.9} (111) | 2.3 ± 0.3 | 2.8 × 10 ¹⁵ | 3.6 | 200 |
| CeO _{1.8} (111) | 2.5 ± 0.3 | 2.8 × 10 ¹⁵ | 3.6 | 220 |
| Fe ₃ O ₄ (111) | 2.5 ± 0.3 | 2.8 × 10 ¹⁵ | 3.6 | 220 |
| Ag(solid) | 2.44 ¹⁹⁸ | ∞ ^b | ∞ ^b | 285 ^c |

^aAlso listed are the Ag particle size and Ag coverage used to get the adhesion energy. The adhesion energy for Ag on Ag (i.e., twice the surface energy of bulk solid Ag) is given for comparison. ^bBulk Ag(solid), so the high coverage/large particle limit. ^cHeat of sublimation of bulk Ag(solid).

adhesion energy increases with the extent of reduction of the CeO₂. These adhesion energies correlate with the initial adsorption energy of the first Ag gas pulse (Table 6). Both values reflect the strength of Ag–oxide bonding.

The adhesion energies of Ag nanoparticles to these CeO_{2-x}(111) and Fe₃O₄(111) surfaces (~2.3–2.5 J/m²) approach and even exceed the adhesion energy of Ag to itself (2.44 J/m²).¹⁹⁸ For an adhesion energy equal to or larger than the Ag/Ag adhesion energy, one would generally not expect the Ag to cluster into 3D islands, but instead to wet the surface. However, these Ag particles bind locally to some part of the oxide surface where there is greater defect (step, kink, or vacancy) concentration than elsewhere, and thus the local adhesion energy is likely less on the stoichiometric oxide terraces. Furthermore, the lattice mismatch between Ag(111) and the underlying oxide will cause the Ag lattice to expand or contract to match the underlying oxide lattice, and also cause the oxide lattice under the Ag island to contract or expand to gain interfacial bonding stability. This strain in the oxide under a Ag island will also force the oxide lattice immediately adjacent to the island to strain in the opposite direction, thus weakening further Ag atom bonding to the island as the island size grows (and also causing particle–particle repulsions).²⁰⁵

The strain arising from such lattice mismatch has been directly observed by electron microscopy for Pd particles on MgO(100), where measurements of the 3D particle shape showed that the adhesion energy increases with decreasing Pd particle size from 0.91 J/m² for 10–15 nm particles to >1.64 J/m² below 5 nm.²⁵⁸ Such tiny Pd particles were seen to increase their lattice parameter to match that of the MgO, whereas regularly spaced Pd dislocations appeared at the interface for particles larger than 10 nm. STM measurements of the 3D particle shape for Cu particles on the ZnO(0001)–Zn surface gave an adhesion energy of 3.4 J/m².²⁵⁹

The types of calorimetric results summarized above may eventually reveal correlations between the strength of metal–oxide bonding and the structural, electronic, chemisorption, and catalytic properties of oxide-supported metal nanoparticles, their dispersion, and their resistance to long-term sintering. This would substantially improve our fundamental understanding of structure/function relationships in heterogeneous catalysis.

Table 7. Adsorption Enthalpies for Metal Atoms Adsorbed on Oxide Surfaces, Listing the Parameters in Equation 28 Used To Fit the Coverage Dependence^a

| adsorbate | oxide surface | T _p /K | log(ν/s ⁻¹) | -ΔH _{ad,init} /kJ/mol | ΔH _{sub} /kJ/mol | θ _C /ML | γ _{v/m} /J/m ² | E _{adh} /J/m ² | θ _{contact} /deg | citation |
|-----------|--|-------------------|-------------------------|--------------------------------|---------------------------|--------------------|------------------------------------|------------------------------------|---------------------------|----------|
| Pd | disordered SiO ₂ /Mo(110) | 1140 → 1290 | 14.5 | 304 | 373 | 1.2 | 2.00 | 2.8 | 66 | 260 |
| Cu | α-Al ₂ O ₃ (0001) or γ-Al ₂ O ₃ (111)/Mo(110) | 980 → 1130 | 14.4 → 14.5 | 279 | 337 | 1.2 | 1.76 | 2.6 | 62 | 261 |
| | disordered SiO ₂ /Mo(110) | 980 → 1140 | 14.4 → 14.5 | 271 | | 1.3 | | 2.3 | 71 | 262 |
| Ag | α-Al ₂ O ₃ (0001) or γ-Al ₂ O ₃ (111)/Re(0001) | 740 → 900 | 14.3 → 14.4 | 221 | 285 | 0.89 | 1.22 | 1.6 | 71 | 263,264 |
| Au | TiO ₂ (001)/Mo(100) | 1080 → 1180 | 14.4 → 14.5 | 318 | 377 | 2.3 | 1.54 | 1.8 | 79 | 265 |
| | disordered SiO ₂ /Mo(110) | 1070 → 1250 | 14.4 → 14.5 | 314 | | 1.3 | | 2.0 | 73 | 266 |

^aDesorption energies at each initial coverage were determined by Redhead analysis of the TPD data in the citations listed, using T_p and the prefactor estimated using eq 16 (also listed for the range of T_p values analyzed). Also listed are the bulk metal's sublimation enthalpy and surface energy from the literature, and the metal/oxide adhesion energy and contact angle determined from these using eqs 30–32.

6.5. TPD Studies of Metal Atom Adsorption Enthalpies on Oxides

The probability that a metal gas atom striking an oxide surfaces becomes at least transiently adsorbed has always been observed to be >0.1 at 300 K or colder for the papers reviewed here and in section 6.4 on SCAC studies of metal adsorption energies on ordered oxide surfaces. Therefore, it is safe to assume that the activation energy for adsorption is <10 kJ/mol. As described above, the activation energy for desorption determined from TPD studies can be used to estimate the heat of adsorption when the activation energy for adsorption is small by simply adding 1/2RT_p. Adsorption enthalpies determined from TPD measurements of submonolayer coverages of metals adsorbed on oxides are summarized in Table 7.

6.5.1. TPD Studies of the Adsorption of Late Transition Metals and Noble Metals.

Figure 15 shows

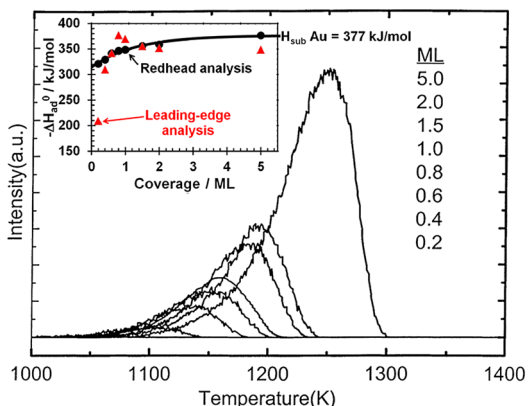


Figure 15. TPD spectra from different Au coverages adsorbed on a 2.5 nm thick SiO₂ film on Mo(110). Reprinted with permission from ref 266. Copyright 2001 Elsevier. The inset shows the heat of adsorption as a function of initial Au coverage determined from the peak temperatures as described in the text, and, for comparison, as determined by the original authors by fitting the leading edge of each TPD spectrum to the Arrhenius law. We present several reasons in the text why such an analysis leads to very large errors at low coverage.

TPD spectra as a function of coverage for Au particles on a 5 nm thick SiO₂ thin film on Mo(110).²⁶⁶ As shown in this typical example, the TPD peak temperatures increase strongly with coverage for submonolayer coverages of late transition metals on such oxides. This has been attributed to the influence of metal particle size on the adsorption energy, associated with the decrease in the number of metal–metal bonds that form as

the metal particles become smaller,^{266–268} which is consistent with our SCAC results above. The inset shows heat of adsorption calculated from the desorption energies determined from these TPD spectra by leading-edge analysis, as reported in the original paper.²⁶⁶ Next, we show why desorption energies determined in this way are highly inaccurate for low coverages of late transition metals, which grow as 3D particles, and explain the alternate method we have adopted for estimating desorption energies for such cases to get the values listed in Table 7. Heats of adsorption determined with this preferred method are also shown in the inset of Figure 15.

While leading-edge analysis and so-called complete analysis of TPD spectra are usually excellent methods for extracting accurate desorption energies, we feel that it has serious problems when applied to systems like late transition metals on oxides, where the adsorbates cluster into 3D particles and the adsorption energy varies so strongly with particle size, as we have shown above. This is because of a breakdown of the basic assumption used in applying eq 4 above to extract E_d. Equation 4 assumes that the surface species are always in equilibrium so that the desorption rate is a single-valued function of coverage and temperature: $r(\theta, T)$. This is far from true here, because sintering is fast for tiny particles, but the sintering rate decreases so dramatically with particle size (see section 6.4.2). As shown above, the same total coverage of large metal particles (>6 nm in diameter) will have a much larger E_d (larger heat of adsorption) than particles with size ~1 nm. The large particles will also have a much smaller total surface area. The net effect is a desorption rate that is many orders of magnitude slower at the same temperature for an oxide surface with large metal particles than for one with small particles, when both samples have the same total coverage. We are convinced that this is the reason that Arrhenius plots of constant-coverage cuts from TPD spectra for Ag on alumina²⁶³ do not show straight lines, but instead the slope decreases dramatically with temperature. This is because the average particle size gets larger with temperature during a TPD experiment, due both to the selective removal of smaller particles because of their faster desorption rates and to sintering driven by the increasing temperature. For the same reason, leading-edge analysis will give an Arrhenius plot that has a slope that is biased toward smaller magnitude (resulting in lower E_d than reality) because the fastest desorption rates are for the smallest particles in the distribution of initial particle sizes present, but these particles disappear almost immediately, and further desorption is biased toward slower and slower rates.

For these reasons, we propose that a simple first-order Redhead analysis using the desorption peak temperature for each coverage with a prefactor estimated as suggested above is a much better method for estimating desorption energies from TPD for such systems. To support this, Figure 16 compares

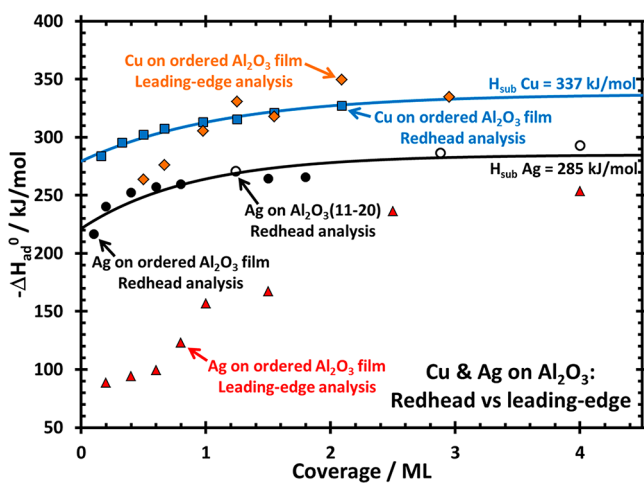


Figure 16. Comparison of heats of adsorption for Cu (upper curves) and Ag (lower curves) on alumina determined from TPD data by simple first-order Redhead analysis assuming a prefactor for desorption based on eq 16 using the entropy correlation of eq 13, which gives a prefactor of $\sim 10^{15} \text{ s}^{-1}$. Also shown for comparison are the results by leading-edge analysis as reported by the original authors. The Cu data are for an ordered Al_2O_3 film grown on Mo(110) whose hexagonal LEED pattern was attributed to either $\alpha\text{-Al}_2\text{O}_3(0001)$ or $\gamma\text{-Al}_2\text{O}_3(111)$.²⁶⁷ The Ag data are from a bulk sapphire $\alpha\text{-Al}_2\text{O}_3(11\bar{2}0)$ surface and a thin Al_2O_3 film grown on Re(0001) (also to either $\alpha\text{-Al}_2\text{O}_3(0001)$ or $\gamma\text{-Al}_2\text{O}_3(111)$), from refs 263 and 264, respectively. The lowest-coverage heat of adsorption for Ag by the leading-edge analysis gave a prefactor of only $\sim 10^5 \text{ s}^{-1}$, which is clearly many orders of magnitude too low. The text argues that the results from our Redhead analysis are much more accurate. Also shown are best fits of eq 28 to these data analyzed by this preferred method.

heats of adsorption versus coverage for Cu and Ag on single-crystalline Al_2O_3 surfaces determined from TPD data reported by Goodman's group^{264,267} and by Van Campen et al.²⁶³ using this preferred method (i.e., using the first-order Redhead equation with a prefactor of $\sim 10^{15} \text{ s}^{-1}$ from eq 16) with those determined from the same data by the original authors using leading-edge analysis. (We also added $1/2RT$ to the desorption energies originally reported to convert to heats of adsorption.) At low coverages, the values reported in the original papers fall far below the values from our preferred Redhead analysis. At the lowest coverages here, this leading-edge analysis gives a prefactor of only $\sim 10^5 \text{ s}^{-1}$ for Ag, which is many orders of magnitude too low according to transition state theory estimates with any reasonable assumptions. Leading-edge analysis of the low-coverage Cu data gave a prefactor of only $\sim 10^{10} \text{ s}^{-1}$, also lower than expected.

Table 7 summarizes the analyses we performed in this way for late transition metals on oxides. The prefactor was estimated in each case using eq 16 based on the entropy correlation we summarized in section 3.2.

As shown in Figure 16, for both Cu and Ag on these ordered Al_2O_3 surfaces, the heat of adsorption increases by 60–70 kJ/mol with coverage, eventually leveling off at the heat of

sublimation. As shown, these heats of adsorption are all well fitted by an equation of the form:

$$q_{\text{ad}}(\theta) = q_{\text{ad},0} + (\Delta H_{\text{sub}} - q_{\text{ad},0})(1 - e^{-\theta/\theta_C}) \quad (28)$$

where $q_{\text{ad},0}$ is the heat of adsorption in the limit of zero coverage, θ is the initial coverage for each TPD spectrum used in this Redhead analysis, and θ_C is a constant proportional to how quickly the heat increases with coverage between $q_{\text{ad},0}$ and ΔH_{sub} . The value for ΔH_{sub} was not treated as a fitting parameter but instead taken from the literature.¹³³ The data in Figure 15 were also well fitted by this equation.

Similar analyses to those in Figure 16 were performed on many previously published TPD spectra for late transition metals on oxides. The results are summarized in Table 7. We list there the parameters $q_{\text{ad},0}$, ΔH_{sub} , and θ_C , which characterize the heat versus coverage curves thus obtained and fitted to eq 28. That these data were all well fitted by eq 28 proves that this Redhead analysis and the choice of prefactors using eq 16 gives accurate values of $q_{\text{ad}}(\theta)$. Otherwise, the data points would not so nicely approach ΔH_{sub} asymptotically at high coverage in each case.

If eq 28 is integrated versus coverage to high coverage, and is combined with eq 20 (assuming the metal makes a flat film), it can be rearranged to give the adhesion energy in terms of these parameters:

$$E_{\text{adh}} = 2\gamma_{v/m} - (\Delta H_{\text{sub}} - q_{\text{ad},0})(n/A)\theta_C \quad (29)$$

Correcting for surface roughness gives:

$$E_{\text{adh}} = (1 + f_r)\gamma_{v/m} - (\Delta H_{\text{sub}} - q_{\text{ad},0})(n/A)\theta_C \quad (30)$$

where f_r is the roughness factor of the metal film. If the metal film consists of spherical caps each with a contact angle to the oxide surface of θ_{contact} , it is a simple geometric derivation to prove that:

$$f_r = 2 \cdot [1 - \cos(\theta_{\text{contact}})] / [\sin^2(\theta_{\text{contact}})] \quad (31)$$

The adhesion energy is also related to the contact angle by the equation of Young and Dupre:¹⁵⁴

$$E_{\text{adh}} = \gamma_{v/m}[1 + \cos(\theta_{\text{contact}})] \quad (32)$$

After substituting eq 31 into eq 30 to remove f_r , eqs 30 and 32 provide two equations in two unknowns, E_{adh} and θ_{contact} . For systems where the parameters for eq 28 have already been measured, such as for the systems in Table 7, these can be solved to provide E_{adh} and θ_{contact} . Note that the initial coverages in the TPD curves that most strongly influence the values of $q_{\text{ad},0}$ and θ_C are low enough that the surface is only partly covered by individual particles during desorption, whereas the overall analysis of eq 30 involves integration of eq 28 to much higher coverages. This is valid because $q_{\text{ad}}(\theta)$ already closely approaches ΔH_{sub} at the higher coverages where the particles merge into a continuous film and the surface roughness factor from eq 31 is no longer reasonable.

The metal/oxide adhesion energies and contact angles estimated in this way for the systems in Table 7 are also listed there. The surface free energies for the metals were taken from refs 197, 198, 226, and n/A was taken as the packing density of the (111) face of the metal. In Table 7, we have listed θ_C using the definition of one monolayer (ML) as given in the original TPD paper cited, which was defined as one adatom per surface atom of the underlying metal substrate (i.e., under the oxide

thin film). (The definition was not always clearly stated, but it is the way that the group generally defined ML in these types of studies.) To use θ_C in eq 29, it must first be converted from those units to the fraction n/A .

6.5.2. TPD Studies of the Adsorption of Alkali Metals.

Because alkali metals have repulsive lateral interactions as adatoms on oxides (see below), the problem with analyzing TPD data to extract desorption energies mentioned above for late transition metals is not a problem here.

The TPD spectra of Cs from $\text{TiO}_2(110)$ is shown in Figure 17 as a function of coverage.²⁶⁹ The sharp peak at ~ 300 K in

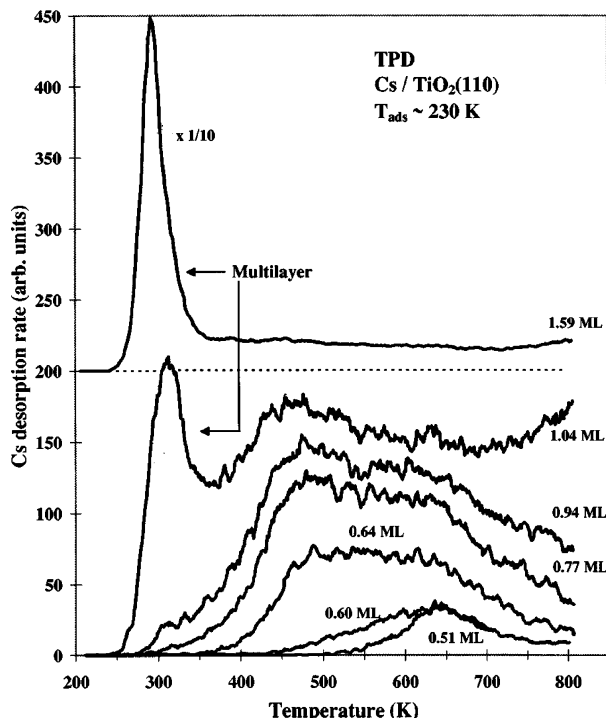


Figure 17. TPD curves for Cs desorption from $\text{TiO}_2(110)$ after adsorption at ~ 230 K to increasing initial coverages of Cs. The completion of a monolayer is easily identified by the appearance of the sharp multilayer peak at ~ 300 K. Coverages below 0.4 ML are so strongly bound that they do not desorb by the highest TPD temperature. The heating rate was ~ 5 K/s. Reprinted with permission from ref 269. Copyright 1997 American Physical Society.

the highest coverage spectrum in the lower panel and ~ 285 K in the upper panel is due to multilayer Cs. Using eq 16 to estimate a desorption prefactor for this 285 K multilayer peak gives a prefactor of 10^{14} s^{-1} . Analyzing this peak temperature with the first-order Redhead equation gives a heat of adsorption of 78 kJ/mol for this multilayer, in nearly perfect agreement with the standard enthalpy of sublimation of bulk Cs(solid) of 78.2 kJ/mol.¹³³ Starting from the lowest coverage shown, there is a continuous population of desorption intensity to increasingly lower temperature with Cs coverage. Coverages below 0.4 ML do not start to desorb until above the highest temperature studied (800 K). This reflects a nearly continuous decrease in heat of adsorption with coverage from above 200 kJ/mol down to the sublimation enthalpy of bulk Cs, 78 kJ/mol. A very similar large, smooth decrease in adsorption energy with coverage is also typically observed for alkali metals on metal surfaces, where it is attributed to increasing dipole-dipole repulsions as these positively charged adsorbates pack

more closely together.²⁷⁰ These repulsions lead to mutual depolarization of the alkali adsorption complexes with increasing coverage within the first monolayer on metals.²⁷⁰ This also occurs for alkali metals on oxide surfaces, as judged by the decrease in local dipole moment with coverage.¹⁵⁴ Work function measurements for Cs on $\text{TiO}_2(110)$ indicate that the adsorbate–substrate complex has a local dipole moment of ~ 6 D at 0.1 ML coverage, but that the dipole moment decreases at higher coverage.²⁶⁹

Adsorbed Cs on alumina also shows TPD spectra similar to Figure 17 in that Cs desorption extends in a broad peak from 1100 to 300 K, reflecting a continuous decrease in the Cs adsorption energy from 263 to 75 kJ/mol with increasing Cs coverage.²⁷¹ Photoemission also showed that this Cs is cationic at low coverages. Similarly for K on $\text{TiO}_2(110)$,²⁷² TPD spectra showed evidence for strongly repulsive K–K interactions in the first layer, with a peak extending from ~ 780 to 380 K. Note that the time scale of the experiment is important for the Cs and K on TiO_2 systems, where reduction of the oxide by the metal is thermodynamically allowed but only marginally, so that it does occur but only after long waiting times.¹⁵⁴

TPD for both K and Cs on $\text{NiO}(100)$,^{273–275} where thermodynamics strongly favor reduction, showed results consistent with strong reduction of the NiO by the alkali metal.¹⁵⁴

7. CONCLUDING REMARKS

The amount of quantitative experimental data on the enthalpies and entropies of adsorption on single-crystalline oxide surfaces is still rather limited. However, this compilation of data reveals a number of important trends. The standard entropies of adsorbed molecules (S_{ad}^0) on single-crystal oxide surfaces are found to linearly track the entropy of the gas-phase molecule at the same temperature (T), such that $S_{ad}^0(T) = 0.70S_{gas}^0(T) - 3.3R$. This provides a powerful tool for predicting prefactors in rate constants for reactions involving adsorbed molecules on oxides. This has been applied here to improve the accuracy of desorption energies extracted from TPD data, and hence adsorption enthalpy measurements by TPD. Heats of molecular adsorption track molecule size, with linear relationships and similar slopes found for both *n*-alkanes and linear alcohols versus the number of carbon atoms in the chain. The heats of adsorption of noble gases vary linearly with atomic number. The heats of adsorption of late transition metals on $\text{MgO}(100)$ are less than, but increase with, the bulk metal's sublimation energy. The heat of adsorption of the same late transition metal atom can vary widely between different oxides. Alkali and alkaline earth metals bind more strongly to oxides, dramatically so at defects. The late transition metals cluster into 3D nanoparticles on oxides of the type used for catalyst supports. The heat of adsorption of the metal atoms to these nanoparticles varies strongly with particle size below 6 nm diameter, and this size dependence varies strongly with the nature of the oxide. Temperature programmed desorption can be used to estimate adsorption and adhesion energies for later transition metals on oxides, but the method for data analysis must be changed from that previously used in the literature, because leading-edge analysis fails dramatically for these systems. There are almost no reliable heats of adsorption for dissociatively adsorbed molecules on single-crystalline oxide surfaces, so data of that type are badly needed. While this Review summarizes many conclusions that could not have been realized without the tremendous work of a large, talented and

dedicated scientific community over the past few decades, it also highlights the need to expand upon our basic knowledge set when it comes to the properties of oxide supports and the thermodynamics of their interactions with adsorbed species. Hopefully, this is just the beginning of many advances that will be made in the near future in understanding these systems, which we feel will ultimately play a vital role in helping advance many technologies.

AUTHOR INFORMATION

Corresponding Author

*E-mail: campbell@chem.washington.edu.

Notes

The authors declare no competing financial interest.

Biographies



Charles T. Campbell is a Professor and the B. Seymour Rabinovitch Endowed Chair in Chemistry, and an Adjunct Professor of both Chemical Engineering and Physics, at the University of Washington. He is the author of over 270 publications on surface chemistry, catalysis, and biosensing. He was Editor-in-Chief of the journal *Surface Science* for 11 years. He is an elected Fellow of both the American Chemical Society (ACS) and the American Association for the Advancement of Science. He received the Arthur W. Adamson Award of the ACS and the ACS Award for Colloid or Surface Chemistry, the Gerhard Ertl Lecture Award, the Ipatieff Lectureship at Northwestern University, and an Alexander von Humboldt Research Award. He served as Chair, Chair-Elect, Vice-Chair, and Treasurer of the Colloid and Surface Chemistry Division of the ACS. He was the founding Co-Director and Director of the University of Washington's Center for NanoTechnology, and helped develop the USA's first Ph.D. program in Nanotechnology there. He received his B.S. in Chemical Engineering (1975) and his Ph.D. in Physical Chemistry (1979, under J. M. White) from the University of Texas at Austin, and then did research in Germany under Gerhard Ertl (2007 Nobel Prize Winner) through 1980.



Jason R. V. Sellers was born in Fredericksburg, VA, but spent his formative years near the coast in Virginia Beach. He finished his B.S. degree in chemistry from Old Dominion University in Norfolk, VA, in 2007 while concurrently working as a research assistant at Morphix Technologies, where he helped develop and test new hazardous chemical detection methods. He is currently a graduate student working toward his Ph.D. degree at the University of Washington under the direction of Professor Charles T. Campbell. His research involves the development of new techniques for calorimetric measurements of the heats of adsorption of metal atoms and the adhesion energies of metal films on single-crystalline oxide surfaces under ultrahigh vacuum conditions where the evolving surface structure can be characterized with surface analysis and diffraction techniques.

ACKNOWLEDGMENTS

We acknowledge support for this work by the National Science Foundation under CHE-1010287, and the Department of Energy Office of Basic Energy Sciences, Chemical Sciences Division, grant no. DE-FG02-96ER14630. We thank Drs. Jens Norskov and Joachim Sauer for discussions that inspired this review. C.T.C. thanks Drs. Josef Michl and John T. Yates, Jr., for inspiring this special issue.

REFERENCES

- (1) Hammer, B.; Norskov, J. K. *Surf. Sci.* **1995**, 343, 211.
- (2) Hammer, B.; Hansen, L. B.; Norskov, J. K. *Phys. Rev. B* **1999**, 59, 7413.
- (3) Norskov, J. K.; Bligaard, T.; Logadottir, A.; Bahn, S.; Hansen, L. B.; Bollinger, M.; Bengaard, H.; Hammer, B.; Sljivancanin, Z.; Mavrikakis, M.; Xu, Y.; Dahl, S.; Jacobsen, C. J. H. *J. Catal.* **2002**, 209, 275.
- (4) Greeley, J.; Mavrikakis, M. *Nat. Mater.* **2004**, 3, 810.
- (5) Norskov, J. K.; Bligaard, T.; Rossmeisl, J.; Christensen, C. H. *Nat. Chem.* **2009**, 1, 37.
- (6) Norskov, J. K.; Abild-Pedersen, F.; Studt, F.; Bligaard, T. *Proc. Natl. Acad. Sci. U.S.A.* **2011**, 108, 937.
- (7) Mavrikakis, M. *Nat. Mater.* **2006**, 5, 847.
- (8) Di Valentin, C.; Pacchioni, G.; Selloni, A. *Phys. Rev. Lett.* **2006**, 97, 166803.
- (9) Ganduglia-Pirovano, M. V.; Hofmann, A.; Sauer, J. *Surf. Sci. Rep.* **2007**, 62, 219.
- (10) Hu, Z. P.; Metiu, H. *J. Phys. Chem. C* **2011**, 115, 5841.
- (11) Campbell, C. T.; Sellers, J. R. V. *J. Am. Chem. Soc.* **2012**, 134, 18109.
- (12) Brennan, D.; Hayward, D. O.; Trapnell, B. M. W. *Proc. R. Soc. London* **1960**, A256, 81.
- (13) Cerny, S. *Surf. Sci. Rep.* **1996**, 26, 3.
- (14) Wedler, G. *Discuss. Faraday Soc.* **1966**, 41, 108.
- (15) Kyser, D. A.; Masel, R. I. *Rev. Sci. Instrum.* **1987**, 58, 2141.

- (16) Borroni-Bird, C. E.; Al-Sarraf, N.; Andersson, S.; King, D. A. *Chem. Phys. Lett.* **1991**, *183*, 516.
- (17) Borroni-Bird, C. E.; King, D. A. *Rev. Sci. Instrum.* **1991**, *62*, 2177.
- (18) Al-Sarraf, N.; Stuckless, J. T.; King, D. A. *Nature* **1992**, *360*, 243.
- (19) Al-Sarraf, N.; Stuckless, J. T.; Wartnaby, C. E.; King, D. A. *Surf. Sci.* **1993**, *283*, 427.
- (20) Al-Sarraf, N.; King, D. A. *Surf. Sci.* **1994**, *307*, 1.
- (21) Stuck, A.; Wartnaby, C. E.; Yeo, Y. Y.; King, D. A. *Phys. Rev. Lett.* **1995**, *74*, 578.
- (22) Stuckless, J. T.; Al-Sarraf, N.; Wartnaby, C.; King, D. A. *J. Chem. Phys.* **1993**, *99*, 2202.
- (23) Stuck, A.; Wartnaby, C. E.; Yeo, Y. Y.; Stuckless, J. T.; Al-Sarraf, N.; King, D. A. *Surf. Sci.* **1996**, *349*, 229.
- (24) Dixon-Warren, S. J.; Kovar, M.; Wartnaby, C. E.; King, D. A. *Surf. Sci.* **1994**, *307*, 16.
- (25) Stuckless, J. T.; Starr, D. E.; Bald, D. J.; Campbell, C. T. *J. Chem. Phys.* **1997**, *107*, 5547.
- (26) Stuckless, J. T.; Frei, N. A.; Campbell, C. T. *Rev. Sci. Instrum.* **1998**, *69*, 2427.
- (27) Stuckless, J. T.; Frei, N. A.; Campbell, C. T. *Sens. Actuators, B* **2000**, *62*, 13.
- (28) Starr, D. E.; Campbell, C. T. *J. Phys. Chem. B* **2001**, *105*, 3776.
- (29) Ajo, H. M.; Ihm, H.; Moilanen, D. E.; Campbell, C. T. *Rev. Sci. Instrum.* **2004**, *75*, 4471.
- (30) Diaz, S. F.; Zhu, J. F.; Shamir, N.; Campbell, C. T. *Sens. Actuators, B* **2005**, *107*, 454.
- (31) Lew, W.; Lytken, O.; Farmer, J. A.; Crowe, M. C.; Campbell, C. T. *Rev. Sci. Instrum.* **2010**, *81*, 024102.
- (32) Fischer-Wolfarth, J. H.; Hartmann, J.; Farmer, J. A.; Flores-Camacho, J. M.; Campbell, C. T.; Schauermann, S.; Freund, H. J. *Rev. Sci. Instrum.* **2011**, *82*, 024102.
- (33) Lytken, O.; Lew, W.; Harris, J. J. W.; Vestergaard, E. K.; Gottfried, J. M.; Campbell, C. T. *J. Am. Chem. Soc.* **2008**, *130*, 10247.
- (34) Lew, W.; Crowe, M. C.; Karp, E.; Lytken, O.; Farmer, J. A.; Arnadottir, L.; Schoenbaum, C.; Campbell, C. T. *J. Phys. Chem. C* **2011**, *115*, 11586.
- (35) Lew, W. D.; Crowe, M. C.; Karp, E.; Campbell, C. T. *J. Phys. Chem. C* **2011**, *115*, 9164.
- (36) Brown, W. A.; Kose, R.; King, D. A. *Chem. Rev.* **1998**, *98*, 797.
- (37) Ge, Q. F.; Kose, R.; King, D. A. *Adv. Catal.* **2000**, *45*, 207.
- (38) Lytken, O.; Lew, W.; Campbell, C. T. *Chem. Soc. Rev.* **2008**, *37*, 2172.
- (39) Campbell, C. T.; Lytken, O. *Surf. Sci.* **2009**, *603*, 1365.
- (40) Crowe, M. C.; Campbell, C. T. *Annu. Rev. Anal. Chem.* **2011**, *4*, 41.
- (41) Dash, J. G.; Ecke, R.; Stoltenberg, J.; Vilches, O. E.; Whittemore, O. J. *J. Phys. Chem.* **1978**, *82*, 1450.
- (42) Coulomb, J. P.; Sullivan, T. S.; Vilches, O. E. *Phys. Rev. B* **1984**, *30*, 4753.
- (43) Sullivan, T. S.; Migone, A. D.; Vilches, O. E. *Surf. Sci.* **1985**, *162*, 461.
- (44) Redhead, P. A. *Vacuum* **1962**, *12*, 203.
- (45) Tait, S. L.; Dohnalek, Z.; Campbell, C. T.; Kay, B. D. *J. Chem. Phys.* **2005**, *122*, 164707.
- (46) Comsa, G.; David, R. *Surf. Sci. Rep.* **1985**, *5*, 145.
- (47) Pauls, S.; Campbell, C. T. *Surf. Sci.* **1990**, *226*, 250.
- (48) Miller, J. B.; Siddiqui, H. R.; Gates, S. M.; Russell, J. N.; Yates, J. T., Jr.; Tully, J. C.; Cardillo, M. J. *J. Chem. Phys.* **1987**, *87*, 6725.
- (49) Dohnalek, Z.; Kimmel, G. A.; Joyce, S. A.; Ayotte, P.; Smith, R. S.; Kay, B. D. *J. Phys. Chem. B* **2001**, *105*, 3747.
- (50) Tait, S. L.; Dohnalek, Z.; Campbell, C. T.; Kay, B. D. *J. Chem. Phys.* **2005**, *122*, 164708.
- (51) Rodriguez, J. A.; Campbell, C. T. *J. Phys. Chem.* **1989**, *93*, 826.
- (52) Trabelsi, M.; Coulomb, J. P. *Surf. Sci.* **1992**, *272*, 352.
- (53) Sidoumou, M.; Panella, V.; Suzanne, J. *J. Chem. Phys.* **1994**, *101*, 6338.
- (54) Arnold, T.; Cook, R. E.; Chanaa, S.; Clarke, S. M.; Farinelli, M.; Yaron, P.; Larese, J. Z. *Phys. B* **2006**, *385*, 205.
- (55) Trabelsi, M.; Saidi, S.; Chefí, C.; Picaud, S.; Hoang, P. N. M.; Coulomb, J. P. *Surf. Sci.* **2004**, *550*, 133.
- (56) Trabelsi, M.; Saidi, S.; Chefí, C.; Martin, C.; Lucas, S.; Ferry, D.; Suzanne, J. *Surf. Sci.* **2004**, *566*, 789.
- (57) Sprung, M.; Larese, J. Z. *Phys. Rev. B* **2000**, *61*, 13155.
- (58) Ferry, D.; Glebov, A.; Senz, V.; Suzanne, J.; Toennies, J. P.; Weiss, H. *Surf. Sci.* **1997**, *377*, 634.
- (59) Ferry, D.; Suzanne, J. *Surf. Sci.* **1996**, *345*, L19.
- (60) Stirnimann, M. J.; Huang, C.; Smith, R. S.; Joyce, S. A.; Kay, B. D. *J. Chem. Phys.* **1996**, *105*, 1295.
- (61) Wichtendahl, R.; Rodriguez-Rodrigo, M.; Hartel, U.; Kuhlenbeck, H.; Freund, H. J. *Phys. Status Solidi A* **1999**, *173*, 93.
- (62) Wichtendahl, R.; Rodriguez-Rodrigo, M.; Hartel, U.; Kuhlenbeck, H.; Freund, H. J. *Surf. Sci.* **1999**, *423*, 90.
- (63) Street, S. C.; Guo, Q.; Xu, C.; Goodman, D. W. *J. Phys. Chem.* **1996**, *100*, 17599.
- (64) Gunster, J.; Liu, G.; Stultz, J.; Goodman, D. W. *J. Chem. Phys.* **1999**, *110*, 2558.
- (65) McQuarrie, D. A. *Statistical Mechanics*; University Science Books: Sausalito, 2000.
- (66) Atkins, P. *Physical Chemistry*, 6th ed.; W. H. Freeman: New York, 1998.
- (67) Tait, S. L.; Dohnalek, Z.; Campbell, C. T.; Kay, B. D. *J. Chem. Phys.* **2006**, *125*, 234308.
- (68) Gellman, A. J.; Paserba, K. R. *J. Phys. Chem. B* **2002**, *106*, 13231.
- (69) Paserba, K. R.; Gellman, A. J. *J. Chem. Phys.* **2001**, *115*, 6737.
- (70) Fichthorn, K. A.; Becker, K. E.; Miron, R. A. *Catal. Today* **2007**, *123*, 71.
- (71) Becker, K. E.; Fichthorn, K. A. *J. Chem. Phys.* **2006**, *125*, 184706.
- (72) Becker, K. E.; Mignogna, M. H.; Fichthorn, K. A. *Phys. Rev. Lett.* **2009**, *102*, 046101.
- (73) Hill, T. L. *An Introduction to Statistical Thermodynamics*; Addison-Wesley: Reading, MA, 1960.
- (74) Lombardo, S. J.; Bell, A. T. *Surf. Sci. Rep.* **1991**, *13*, 1.
- (75) Madix, R. J.; Ertl, G.; Christmann, K. *Chem. Phys. Lett.* **1979**, *62*, 38.
- (76) Sellers, H.; Gislason, J. *Surf. Sci.* **1999**, *426*, 147.
- (77) Wise, M. L.; Koehler, B. G.; Gupta, P.; Coon, P. A.; George, S. M. *Surf. Sci.* **1991**, *258*, 166.
- (78) Zhdanov, V. P. *Surf. Sci. Rep.* **1991**, *12*, 183.
- (79) Starr, D. E.; Campbell, C. T. *J. Am. Chem. Soc.* **2008**, *130*, 7321.
- (80) Campbell, C. T.; Sun, Y.-K.; Weinberg, W. H. *Chem. Phys. Lett.* **1991**, *179*, 53.
- (81) Arthur, D. A.; Meixner, D. L.; Boudart, M.; George, S. M. *J. Chem. Phys.* **1991**, *95*, 8521.
- (82) Echterhoff, R.; Knozinger, E. *Surf. Sci.* **1990**, *230*, 237.
- (83) Cardonamartinez, N.; Dumescic, J. A. *Adv. Catal.* **1992**, *38*, 149.
- (84) Dohnalek, Z.; Kim, J.; Bondarchuk, O.; White, J. M.; Kay, B. D. *J. Phys. Chem. B* **2006**, *110*, 6229.
- (85) Henderson, M. A.; Epling, W. S.; Perkins, C. L.; Peden, C. H. F.; Diebold, U. *J. Phys. Chem. B* **1999**, *103*, 5328.
- (86) Dillmann, B.; Rohr, F.; Seiferth, O.; Klivenyi, G.; Bender, M.; Homann, K.; Yakovkin, I. N.; Ehrlich, D.; Baumer, M.; Kuhlenbeck, H.; Freund, H. J. *Faraday Discuss.* **1996**, *105*, 295.
- (87) Hinojosa, J. A.; Kan, H. H.; Weaver, J. F. *J. Phys. Chem. C* **2008**, *112*, 8324.
- (88) Linsebigler, A.; Lu, G. Q.; Yates, J. T., Jr. *J. Chem. Phys.* **1995**, *103*, 9438.
- (89) Pykavy, M.; Staemmler, V.; Seiferth, O.; Freund, H. J. *Surf. Sci.* **2001**, *479*, 11.
- (90) Lemire, C.; Meyer, R.; Henrich, V. E.; Shaikhutdinov, S.; Freund, H. J. *Surf. Sci.* **2004**, *572*, 103.
- (91) Ge, Q. F.; Moller, P. J. *Appl. Surf. Sci.* **1994**, *82–3*, 305.
- (92) Sorescu, D. C.; Rusu, C. N.; Yates, J. T., Jr. *J. Phys. Chem. B* **2000**, *104*, 4408.
- (93) Paulus, U. A.; Wang, Y.; Jacobi, K.; Ertl, G. *Surf. Sci.* **2003**, *547*, 349.

- (94) Matolin, V.; Matolinova, I.; Dvorak, F.; Johanek, V.; Myslivecek, J.; Prince, K. C.; Skala, T.; Stetsovych, O.; Tsud, N.; Vaclavu, M.; Smid, B. *Catal. Today* **2012**, *181*, 124.
- (95) Henderson, M. A.; Perkins, C. L.; Engelhard, M. H.; Thevuthasan, S.; Peden, C. H. F. *Surf. Sci.* **2003**, *S26*, 1.
- (96) Herman, G. S.; Kim, Y. J.; Chambers, S. A.; Peden, C. H. F. *Langmuir* **1999**, *15*, 3993.
- (97) Hugenschmidt, M. B.; Gamble, L.; Campbell, C. T. *Surf. Sci.* **1994**, *302*, 329.
- (98) Herman, G. S.; Dohnalek, Z.; Ruzicka, N.; Diebold, U. *J. Phys. Chem. B* **2003**, *107*, 2788.
- (99) Henderson, M. A. *Surf. Sci.* **1994**, *319*, 315.
- (100) Henderson, M. A.; Chambers, S. A. *Surf. Sci.* **2000**, *449*, 135.
- (101) Joseph, Y.; Kuhrs, C.; Ranke, W.; Ritter, M.; Weiss, W. *Chem. Phys. Lett.* **1999**, *314*, 195.
- (102) Peden, C. H. F.; Herman, G. S.; Ismagilov, I. Z.; Kay, B. D.; Henderson, M. A.; Kim, Y. J.; Chambers, S. A. *Catal. Today* **1999**, *51*, 513.
- (103) Lobo, A.; Conrad, H. *Surf. Sci.* **2003**, *523*, 279.
- (104) Kan, H. H.; Colmyer, R. J.; Astagiri, A.; Weaver, J. F. *J. Phys. Chem. C* **2009**, *113*, 1495.
- (105) Cox, D. F.; Schulz, K. H. *Surf. Sci.* **1991**, *256*, 67.
- (106) Zwicker, G.; Jacobi, K. *Surf. Sci.* **1983**, *131*, 179.
- (107) Zhang, R.; Ludviksson, A.; Campbell, C. T. *Surf. Sci.* **1993**, *289*, 1.
- (108) Wang, Y.; Muhler, M.; Woell, C. *Phys. Chem. Chem. Phys.* **2006**, *8*, 1521.
- (109) Thompson, T. L.; Diwald, O.; Yates, J. T., Jr. *J. Phys. Chem. B* **2003**, *107*, 11700.
- (110) Wang, J.; Hokkanen, B.; Burghaus, U. *Surf. Sci.* **2005**, *577*, 158.
- (111) Mullins, D. R.; McDonald, T. S. *Surf. Sci.* **2008**, *602*, 1280.
- (112) Weaver, J. F.; Hakanoglu, C.; Hawkins, J. M.; Astagiri, A. J. *Chem. Phys.* **2010**, *132*, 024709.
- (113) Weaver, J. F.; Devarajan, S. P.; Hakanoglu, C. *J. Phys. Chem. C* **2009**, *113*, 9773.
- (114) Weaver, J. F.; Hinojosa, J. A., Jr.; Hakanoglu, C.; Antony, A.; Hawkins, J. M.; Astagiri, A. *Catal. Today* **2011**, *160*, 213.
- (115) Wang, J.; Hokkanen, B.; Burghaus, U. *Surf. Sci.* **2006**, *600*, 4855.
- (116) Grant, A. W.; Ngo, L. T.; Stegelman, K.; Campbell, C. T. *J. Phys. Chem. B* **2003**, *107*, 1180.
- (117) Hemmerich, I.; Rohr, F.; Seiferth, O.; Dillmann, B.; Freund, H. J. *Faraday Discuss.* **1997**, *105*, 295.
- (118) Paulus, U. A.; Wang, Y.; Bonzel, H. P.; Jacobi, K.; Ertl, G. *J. Phys. Chem. B* **2005**, *109*, 2139.
- (119) Ajo, H. M.; Bondzie, V. A.; Campbell, C. T. *Catal. Lett.* **2002**, *78*, 359.
- (120) Robbins, M. D.; Henderson, M. A. *J. Catal.* **2006**, *238*, 111.
- (121) Ngo, L. T.; Xu, L. J.; Grant, A. W.; Campbell, C. T. *J. Phys. Chem. B* **2003**, *107*, 1174.
- (122) Poss, D.; Ranke, W.; Jacobi, K. *Surf. Sci.* **1981**, *105*, 77.
- (123) Li, Z.; Smith, R. S.; Kay, B. D.; Dohnalek, Z. *J. Phys. Chem. C* **2011**, *115*, 22534.
- (124) Henderson, M. A.; Otero-Tapia, S.; Castro, M. E. *Faraday Discuss.* **1999**, *114*, 313.
- (125) Kiss, J.; Langenberg, D.; Silber, D.; Traeger, F.; Jin, L.; Qiu, H.; Wang, Y.; Meyer, B.; Woell, C. *J. Phys. Chem. A* **2011**, *115*, 7180.
- (126) Nishimura, S. Y.; Gibbons, R. F.; Tro, N. J. *J. Phys. Chem. B* **1998**, *102*, 6831.
- (127) Gamble, L.; Jung, L. S.; Campbell, C. T. *Surf. Sci.* **1996**, *348*, 1.
- (128) Senanayake, S. D.; Gordon, W. O.; Overbury, S. H.; Mullins, D. R. *J. Phys. Chem. C* **2009**, *113*, 6208.
- (129) Henderson, M. A. *J. Phys. Chem. B* **2004**, *108*, 18932.
- (130) Truong, C. M.; Wu, M. C.; Goodman, D. W. *J. Chem. Phys.* **1992**, *97*, 9447.
- (131) Ludviksson, A.; Zhang, R.; Campbell, C. T.; Griffiths, K. *Surf. Sci.* **1994**, *313*, 64.
- (132) Antony, A.; Hakanoglu, C.; Astagiri, A.; Weaver, J. F. *J. Chem. Phys.* **2012**, *136*, 054702.
- (133) CRC Handbook of Chemistry and Physics (Internet Version), 88th ed.; Lide, D. R., Ed.; CRC Press/Taylor and Francis: Boca Raton, FL, 2008.
- (134) Karp, E. M.; Silbaugh, T. L.; Crowe, M. C.; Campbell, C. T. *J. Am. Chem. Soc.* **2012**, *134*, 20388.
- (135) Zhang, Z. R.; Bondarchuk, O.; White, J. M.; Kay, B. D.; Dohnalek, Z. *J. Am. Chem. Soc.* **2006**, *128*, 4198.
- (136) Zhou, C. Y.; Ren, Z. F.; Tan, S. J.; Ma, Z. B.; Mao, X. C.; Dai, D. X.; Fan, H. J.; Yang, X. M.; LaRue, J.; Cooper, R.; Wodtke, A. M.; Wang, Z.; Li, Z. Y.; Wang, B.; Yang, J. L.; Hou, J. G. *Chem. Sci.* **2010**, *1*, 575.
- (137) Dohnalek, Z.; Lyubinetsky, I.; Rousseau, R. *Prog. Surf. Sci.* **2010**, *85*, 161.
- (138) Hansen, J. O.; Huo, P.; Martinez, U.; Lira, E.; Wei, Y. Y.; Streber, R.; Laegsgaard, E.; Hammer, B.; Wendt, S.; Besenbacher, F. *Phys. Rev. Lett.* **2011**, *107*, 136102.
- (139) Huo, P.; Hansen, J. O.; Martinez, U.; Lira, E.; Streber, R.; Wei, Y. Y.; Laegsgaard, E.; Hammer, B.; Wendt, S.; Besenbacher, F. *J. Phys. Chem. Lett.* **2012**, *3*, 283.
- (140) Bondarchuk, O.; Kim, Y. K.; White, J. M.; Kim, J.; Kay, B. D.; Dohnalek, Z. *J. Phys. Chem. C* **2007**, *111*, 11059.
- (141) Zhang, Z. R.; Bondarchuk, O.; Kay, B. D.; White, J. M.; Dohnalek, Z. *J. Phys. Chem. C* **2007**, *111*, 3021.
- (142) Gamble, L.; Jung, L. S.; Campbell, C. T. *Surf. Sci.* **1996**, *348*, 1.
- (143) Hugenschmidt, M. B.; Gamble, L.; Campbell, C. T. *Surf. Sci.* **1994**, *302*, 329.
- (144) Henderson, M. A.; Joyce, S. A.; Rustad, J. R. *Surf. Sci.* **1998**, *417*, 66.
- (145) Elam, J. W.; Nelson, C. E.; Cameron, M. A.; Tolbert, M. A.; George, S. M. *J. Phys. Chem. B* **1998**, *102*, 7008.
- (146) Griffin, G. L.; Yates, J. T., Jr. *J. Chem. Phys.* **1982**, *77*, 3751.
- (147) Wang, Y.; Meyer, B.; Yin, X.; Kunat, M.; Langenberg, D.; Traeger, F.; Birkner, A.; Woell, C. *Phys. Rev. Lett.* **2005**, *95*, 266104.
- (148) Becker, T.; Hovel, S.; Kunat, M.; Boas, C.; Burghaus, U.; Woell, C. *Surf. Sci.* **2001**, *486*, L502.
- (149) Becker, T.; Hovel, S.; Kunat, M.; Boas, C.; Burghaus, U.; Woell, C. *Surf. Sci.* **2002**, *511*, 463.
- (150) Bäumer, M.; Freund, H.-J. *Prog. Surf. Sci.* **1999**, *61*, 127.
- (151) Freund, H. J.; Baumer, M.; Kuhlenbeck, H. *Adv. Catal.* **2000**, *45*, 333.
- (152) Henry, C. R.; Chapon, C.; Giorgio, S.; Goyhenex, C. In *Chemisorption and Reactivity on Supported Clusters and Thin Films*; Lambert, R. M., Pacchioni, G., Eds.; Kluwer Academic Publishers: Amsterdam, 1997.
- (153) Henry, C. R. *Surf. Sci. Rep.* **1998**, *31*, 231.
- (154) Campbell, C. T. *Surf. Sci. Rep.* **1997**, *227*, 1.
- (155) Gunter, P. L. J.; Niemantsverdriet, J. W. *Catal. Rev.-Sci. Eng.* **1997**, *39*, 77.
- (156) Freund, H.-J. *Angew. Chem., Int. Ed. Engl.* **1997**, *36*, 452.
- (157) Persaud, R.; Madey, T. E. In *The Chemical Physics of Solid Surfaces and Heterogeneous Catalysis*; King, D. A., Woodruff, D. P., Eds.; Elsevier: Amsterdam, 1997; Vol. 8.
- (158) Rainer, D. R.; Goodman, D. W. *J. Mol. Catal. A: Chem.* **1998**, *131*, 259.
- (159) Diebold, U.; Pan, J.-M.; Madey, T. E. *Surf. Sci.* **1995**, *331–333*, 845.
- (160) Libuda, J.; Freund, H. J. *Surf. Sci. Rep.* **2005**, *57*, 157.
- (161) Freund, H. J. *Catal. Today* **2005**, *100*, 3.
- (162) Freund, H. J.; Libuda, J.; Baumer, M.; Risse, T.; Carlsson, A. *Chem. Rec.* **2003**, *3*, 181.
- (163) Henry, C. R. *Prog. Surf. Sci.* **2005**, *80*, 92.
- (164) Nilius, N.; Corper, A.; Bozdech, G.; Ernst, N.; Freund, H. J. *Prog. Surf. Sci.* **2001**, *67*, 99.
- (165) Freund, H. J. *Surf. Sci.* **2007**, *601*, 1438.
- (166) Schoiswohl, J.; Sock, M.; Chen, Q.; Thornton, G.; Kresse, G.; Ramsey, M. G.; Surnev, S.; Netzer, F. P. *Top. Catal.* **2007**, *46*, 137.
- (167) Chen, M. S.; Goodman, D. W. *Acc. Chem. Res.* **2006**, *39*, 739.
- (168) Wallace, W. T.; Min, B. K.; Goodman, D. W. *Top. Catal.* **2005**, *34*, 17.

- (169) McClure, S. M.; Goodman, D. W. *Top. Catal.* **2011**, *54*, 349.
- (170) Nilius, N.; Risse, T.; Schauermann, S.; Shaikhutdinov, S.; Sterrer, M.; Freund, H. J. *Top. Catal.* **2011**, *54*, 4.
- (171) Risse, T.; Shaikhutdinov, S.; Nilius, N.; Sterrer, M.; Freund, H. J. *Acc. Chem. Res.* **2008**, *41*, 949.
- (172) Nakamura, J.; Rodriguez, J. A.; Campbell, C. T. *J. Phys.: Condens. Matter* **1989**, *1*, SB149.
- (173) Pan, J.-M.; Diebold, U.; Zhang, L.; Madey, T. E. *Surf. Sci.* **1993**, *295*, 411.
- (174) Pan, J.-M.; Maschhoff, B. L.; Diebold, U.; Madey, T. E. *Surf. Sci.* **1993**, *291*, 381.
- (175) Pan, J.-M.; Madey, T. E. *J. Vac. Sci. Technol., A* **1993**, *11*, 1667.
- (176) Pan, J.-M.; Madey, T. E. *Catal. Lett.* **1993**, *20*, 269.
- (177) Dake, L. S.; Lad, R. J. *J. Vac. Sci. Technol., A* **1995**, *13*, 122.
- (178) Zhang, Z.; Henrich, V. E. *Surf. Sci.* **1992**, *277*, 263.
- (179) Zhao, X. A.; Kolawa, E.; Nicolet, M. A. *J. Vac. Sci. Technol., A* **1986**, *4*, 3139.
- (180) Ohuchi, F. S.; Kohyama, M. *J. Am. Ceram. Soc.* **1991**, *74*, 1163.
- (181) Imdaduddin, S.; Lad, R. J. *Surf. Sci.* **1993**, *290*, 35.
- (182) Saxena, S. K.; Chatterjee, N.; Fei, Y.; Shen, G. *Thermodynamic Data on Oxides and Silicates*; Springer-Verlag: New York, 1993.
- (183) Adamson, A. W. *Physical Chemistry of Surfaces*, 5th ed.; John Wiley and Sons: New York, 1990.
- (184) Schick, M. *Les Houches, Session XLVIII*, 1988; p 415.
- (185) Overbury, S. H.; Bertrand, P. A.; Somorjai, G. A. *Chem. Rev.* **1975**, *75*, 547.
- (186) Chatain, D.; Coudurier, L.; Eustathopoulos, N. *Rev. Phys. Appl.* **1988**, *23*, 1055.
- (187) Chatain, D.; Rivollet, I.; Eustathopoulos, N. *J. Chim. Phys. Phys.-Chim. Biol.* **1986**, *83*, 561.
- (188) Chatain, D.; Rivollet, I.; Eustathopoulos, N. *J. Chim. Phys. Phys.-Chim. Biol.* **1987**, *84*, 201.
- (189) Sangiorgi, R.; Muolo, M. L.; Chatain, D.; Eustathopoulos, N. *J. Am. Ceram. Soc.* **1988**, *71*, 742.
- (190) Rivollet, I.; Chatain, D.; Eustathopoulos, N. *Acta Metall.* **1987**, *35*, 835.
- (191) Didier, F.; Jupille, J. *Surf. Sci.* **1994**, *314*, 378.
- (192) Stoneham, A. M. *Appl. Surf. Sci.* **1982–83**, *14*, 249.
- (193) Naidich, J. V. *Prog. Surf. Membr. Sci.* **1981**, *14*, 354.
- (194) Tyson, W. R.; Miller, W. A. *Surf. Sci.* **1977**, *62*, 267.
- (195) Campbell, C. T.; Starr, D. E. *J. Am. Chem. Soc.* **2002**, *124*, 9212.
- (196) Campbell, C. T.; Parker, S. C.; Starr, D. E. *Science* **2002**, *298*, 811.
- (197) Ranney, J. T.; Starr, D. E.; Musgrove, J. E.; Bald, D. J.; Campbell, C. T. *Faraday Discuss.* **1999**, *114*, 195.
- (198) Larsen, J. H.; Ranney, J. T.; Starr, D. E.; Musgrove, J. E.; Campbell, C. T. *Phys. Rev. B* **2001**, *63*, 195410.
- (199) Larsen, J. H.; Starr, D. E.; Campbell, C. T. *J. Chem. Thermodyn.* **2001**, *33*, 333.
- (200) Starr, D. E.; Bald, D. J.; Musgrove, J.; Ranney, J.; Campbell, C. T. *J. Chem. Phys.* **2001**, *114*, 3752.
- (201) Starr, D. E.; Diaz, S. F.; Musgrove, J. E.; Ranney, J. T.; Bald, D. J.; Nelen, L.; Ihm, H.; Campbell, C. T. *Surf. Sci.* **2002**, *515*, 13.
- (202) Zhu, J.; Farmer, J. A.; Ruzycki, N.; Xu, L.; Campbell, C. T.; Henkelman, G. *J. Am. Chem. Soc.* **2008**, *130*, 2314.
- (203) Farmer, J. A.; Ruzycki, N.; Zhu, J. F.; Campbell, C. T. *Phys. Rev. B* **2009**, *80*, 035418.
- (204) Farmer, J. A.; Ruzycki, N.; Zhu, J.; Xu, L.; Campbell, C. T.; Henkelman, G. *J. Am. Chem. Soc.* **2009**, *131*, 3098.
- (205) Farmer, J. A.; Campbell, C. T. *Science* **2010**, *329*, 933.
- (206) Farmer, J. A.; Barciuato, J. H.; Campbell, C. T. *J. Phys. Chem. C* **2010**, *114*, 17166.
- (207) Campbell, C. T.; Sharp, J. C.; Yao, Y. X.; Karp, E. M.; Silbaugh, T. L. *Faraday Discuss.* **2011**, *152*, 227.
- (208) Benedetti, S.; Benia, H. M.; Nilius, N.; Valeri, S.; Freund, H. J. *Chem. Phys. Lett.* **2006**, *430*, 330.
- (209) Xu, L.; Henkelman, G. *Phys. Rev. B* **2008**, *77*, 205404.
- (210) Snyder, J. A.; Jaffe, J. E.; Gutowski, M.; Lin, Z. J.; Hess, A. C. J. *Chem. Phys.* **2000**, *112*, 3014.
- (211) Zhukovskii, Y. F.; Kotomin, E. A.; Borstel, G. *Vacuum* **2004**, *74*, 235.
- (212) Musolino, V.; Selloni, A.; Car, R. *Surf. Sci.* **1998**, *402–4*, 413.
- (213) Henkelman, G., private communication.
- (214) Giordano, L.; Baistrocchi, M.; Pacchioni, G. *Phys. Rev. B* **2005**, *72*, 115403.
- (215) Hu, Y. L.; Zhang, W. B.; Deng, Y. H.; Tang, B. Y. *Comput. Mater. Sci.* **2008**, *42*, 43.
- (216) Xu, L. J.; Henkelman, G. *Phys. Rev. B* **2010**, *82*, 115407.
- (217) Giordano, L.; Di Valentin, C.; Goniakowski, J.; Pacchioni, G. *Phys. Rev. Lett.* **2004**, *92*, 096105.
- (218) Henry, C. R.; Chapon, C.; Duriez, C.; Giorgio, S. *Surf. Sci.* **1991**, *253*, 177.
- (219) Venables, J. A. *Surf. Sci.* **1994**, *299/300*, 798.
- (220) Venables, J. A.; Harding, J. H. *J. Cryst. Growth* **2000**, *211*, 27.
- (221) Venables, J. A. *Introduction to Surface and Thin Film Processes*; Cambridge: New York, 2000.
- (222) Venables, J. A. *Philos. Mag.* **1973**, *27*, 697.
- (223) Hu, M.; Noda, S.; Komiyama, H. *Surf. Sci.* **2002**, *S13*, 530.
- (224) Wynblatt, P.; Gjostein, N. A. *Acta Metall.* **1976**, *24*, 1165.
- (225) Galanakis, I.; Papanikolaou, N.; Dederichs, P. H. *Surf. Sci.* **2002**, *511*, 1.
- (226) Liu, C. L.; Cohen, J. M.; Adams, J. B.; Voter, A. F. *Surf. Sci.* **1991**, *253*, 334.
- (227) Parker, S. C.; Campbell, C. T. *Phys. Rev. B* **2007**, *75*, 035430.
- (228) Yang, L. Q.; Depristo, A. E. *J. Catal.* **1994**, *149*, 223.
- (229) Methfessel, M.; Hennig, D.; Scheffler, M. *Appl. Phys.* **1992**, *A55*, 442.
- (230) Wynblatt, P.; Gjostein, N. A. In *Progress in Solid State Chemistry*; McCaldin, J. O., Somorjai, G. A., Eds.; Pergamon Press: Oxford, 1975; Vol. 9.
- (231) Wynblatt, P.; Betta, R. A. D.; Gjostein, N. A. In *The Physical Basis for Heterogeneous Catalysis*; Drauglis, E., Jaffee, R. I., Eds.; Plenum Press: New York, 1975.
- (232) Ahn, T.-H.; Wynblatt, P.; Tien, J. K. *Acta Metall.* **1981**, *29*, 921.
- (233) McVicker, G. B.; Garten, R. L.; Baker, R. T. *J. Catal.* **1978**, *54*, 129.
- (234) Ruckenstein, E.; Dadyburjor, D. B. *Rev. Chem. Eng.* **1983**, *1*, 251.
- (235) Fuentes, G. A.; Gamas, E. D. In *Catalyst Deactivation*; Bartholomew, C. H., Butt, J. B., Eds.; Elsevier Science: Amsterdam, 1991.
- (236) Fuentes, G. A.; Salinas-Rodriguez, E. In *Catalyst Deactivation*; Bartholomew, C. H., Fuentes, G. A., Eds.; Elsevier Science: New York, 1997.
- (237) *Sintering Kinetics of Supported Metals: Perspectives from a Generalized Power Law Approach*; Bartholomew, C. H., Ed.; Elsevier Science B. V.: New York, 1994; Vol. 88.
- (238) Bartholomew, C. H. In *Catalyst Deactivation*; Bartholomew, C. H., Fuentes, G. A., Eds.; Elsevier Science B. V.: New York, 1997.
- (239) Lai, X.; Goodman, D. W. *J. Mol. Catal.* **2000**, *A162*, 33.
- (240) Jak, M. J.; Konstapel, C.; Kreuningen, A. v.; Crost, J.; Verhoeven, J.; Frenken, J. W. *Surf. Sci.* **2001**, *474*, 28.
- (241) Jak, M. J.; Konstapel, C.; Kreuningen, A. v.; Verhoeven, J.; Frenken, J. W. *Surf. Sci.* **2000**, *457*, 259.
- (242) Cosandey, F.; Madey, T. E. *Surf. Rev. Lett.* **2001**, *8*, 73.
- (243) Sault, A. G.; Tikare, V. J. *Catal.* **2002**, *211*, 19.
- (244) Sehested, J. *J. Catal.* **2003**, *217*, 417.
- (245) Imre, A.; Gontier-Moya, E.; Beke, D. L.; Szabo, I. A.; Erdelyi, G. *Surf. Sci.* **1999**, *441*, 133.
- (246) Parker, S. C.; Campbell, C. T. *Top. Catal.* **2007**, *44*, 3.
- (247) Luches, P.; Pagliuca, F.; Valeri, S.; Illas, F.; Preda, G.; Pacchioni, G. *J. Phys. Chem. C* **2012**, *116*, 1122.
- (248) Ricci, D.; Bongiorno, A.; Pacchioni, G.; Landman, U. *Phys. Rev. Lett.* **2006**, *97*, 036106.
- (249) Haruta, M.; Tsubota, S.; Kobayashi, T.; Kageyama, H.; Genet, M. J.; Delmon, B. *J. Catal.* **1993**, *144*, 175.
- (250) Haruta, M. *Catal. Today* **1997**, *36*, 153.

- (251) Haruta, M.; Date, M. *Appl. Catal., A* **2001**, *222*, 427.
(252) Haruta, M. *CATTECH* **2002**, *6*, 102.
(253) Valden, M.; Lai, X.; Goodman, D. W. *Science* **1998**, *281*, 1647.
(254) Valden, M.; Pak, S.; Lai, X.; Goodman, D. W. *Catal. Lett.* **1998**, *56*, 7.
(255) Kalakkad, D.; Datye, A. K.; Robota, H. *Appl. Catal., B* **1992**, *1*, 191.
(256) Schwartz, J. M.; Schmidt, L. D. *J. Catal.* **1992**, *138*, 283.
(257) Wang, J. H.; Liu, M. L.; Lin, M. C. *Solid State Ionics* **2006**, *177*, 939.
(258) Graoui, H.; Giorgio, S.; Henry, C. R. *Philos. Mag. B* **2001**, *81*, 1649.
(259) Koplitz, L. V.; Dulub, O.; Diebold, U. *J. Phys. Chem. B* **2003**, *107*, 10583.
(260) Xu, X.; Szanyi, J.; Xu, Q.; Goodman, D. W. *Catal. Today* **1994**, *21*, 57.
(261) Wu, M. C.; Goodman, D. W. *J. Phys. Chem.* **1994**, *98*, 9874.
(262) Xu, X.; He, J.-W.; Goodman, D. W. *Surf. Sci.* **1993**, *284*, 103.
(263) Campen, D. G. V.; Hrbek, J. *J. Phys. Chem.* **1995**, *99*, 16389.
(264) Luo, K.; Lai, X.; Yi, C. W.; Davis, K. A.; Gath, K. K.; Goodman, D. W. *J. Phys. Chem. B* **2005**, *109*, 4064.
(265) Xu, C.; Oh, W. S.; Liu, G.; Kim, D. Y.; Goodman, D. W. *J. Vac. Sci. Technol., A* **1997**, *15*, 1261.
(266) Luo, K.; Kim, D. Y.; Goodman, D. W. *J. Mol. Catal. A: Chem.* **2001**, *167*, 191.
(267) Wu, M.-C.; Goodman, D. W. *J. Phys. Chem.* **1994**, *98*, 9874.
(268) Goodman, D. W. *Surf. Rev. Lett.* **1995**, *2*, 9.
(269) Grant, A. W.; Campbell, C. T. *Phys. Rev. B* **1997**, *55*, 1844.
(270) Campbell, C. T. *Annu. Rev. Phys. Chem.* **1990**, *41*, 775.
(271) Rodriguez, J. A.; Kuhn, M.; Hrbek, J. *J. Phys. Chem.* **1996**, *100*, 18240.
(272) Lad, R. J.; Dake, L. S. *Mater. Res. Soc. Symp. Proc.* **1992**, *238*, 823.
(273) Kennou, S.; Kamaratos, M.; Papageorgopoulos, C. A. *Vacuum* **1990**, *41*, 22.
(274) Chen, J. G.; Weisel, M. D.; Hardenbergh, J. H.; Hoffmann, F. M.; Moms, C. A.; Hall, R. B. *J. Vac. Sci. Technol., A* **1991**, *9*, 1684.
(275) Kennou, S.; Kamaratos, M.; Papageorgopoulos, C. A. *Surf. Sci.* **1991**, *256*, 312.